

Moosfluh, towards a rock slope failure?

Master Thesis

Author(s):

Galletti, Maud

Publication date:

2018

Permanent link:

<https://doi.org/10.3929/ethz-b-000456801>

Rights / license:

[In Copyright - Non-Commercial Use Permitted](#)

Master Thesis

Department of Earth Sciences, Engineering Geology

Moosfluh, towards a rock slope failure?

Fig. 1: View on the Moosfluh landslide from Driest (Photo taken by Maud Galletti)

Maud Galletti

31st July 2018

Main Supervisor: Andrea Manconi (ETH)

Co-supervisor: Franziska Glüer (ETH)

Matteo Picozzi (Università Federico II, Naples, Italy)

ABSTRACT

Landslides and rockfalls are critical hazards to take into account in mountainous areas and understanding their mechanisms is crucial for mitigation purposes. Due to climate change, permafrost degradation and glacial retreat are becoming more and more relevant to consider in steep terrain. Indeed critically stressed slopes might react to these rapid changes and generate an increasing number of rock failure events. In the Great Aletsch region (Switzerland) glacial retreat has been considerable in the last decade and the adjacent southern slope (Moosfluh) has suffered progressive debuttressing, as well as increased deep-seated gravitational slope deformation (DSGD) and enhanced rock failure phenomena.

In this study, we investigate rockfall events occurring in the lower portions of the Moosfluh DSGD in the 2017 summer season. We used a local network of three low-cost seismometers (raspberry shakes), webcam photos and field data to detect rockfalls and generate an event's catalogue. Rockfall parameters as duration, amplitude, volume, runout, energy, as well as their spatial and temporal distribution, provided insights into the mechanisms driving the slope deformation.

An increase in rockfall activity was detected at the beginning of August, corresponding to 3 days of heavy rainfalls. The weeks later followed a change in the displacement rate of the entire DSGD. We also found that the majority of rockfalls occurred during night, pointing out a potential effect of daily surface temperature changes leading to rock contraction and eventually failure events. The peculiar spatial pattern of rockfall suggested temporally and spatially dependent activity for displacement in different domains of the moving mass. Finally, we calibrated a magnitude frequency relationship, which provides hints for mitigation strategies in Moosfluh as well as in other similar alpine areas.

TABLE OF CONTENTS

Abstract	3
Table of contents	5
List of Figures, tables and Appendix	7
1 Introduction	9
2 Goals	10
2.1 Key Questions	10
3 Background	10
3.1 Study area	11
3.2 Existing Monitoring Network	11
3.3 Geology	12
3.4 Recent movements	14
3.5 Passive seismic monitoring to study rockfalls	16
4 Data	17
4.1 Seismic data	18
4.2 Optical data	20
4.2.1 Webcam images	20
4.2.2 Orthophoto.....	22
4.2.3 High resolution photograph (Geoprævent).....	23
4.2.4 Digital elevation model (DEM)	24
4.2.5 Leica vector.....	24
5 Methodology	25
5.1 Events identification	25
5.2 Events classification	29
5.3 Seismic data	32
5.4 Optical data	33
5.4.1 Webcam.....	34

5.4.2	Selected events for Leica vector and georectification measurements.....	34
5.4.3	Leica vector.....	35
5.4.4	Georectification.....	35
5.4.5	Block volume estimation	37
5.5	Data combination	38
5.5.1	Energy calculation	38
5.5.2	Magnitude frequency plot.....	40
6	Results and interpretation.....	41
6.1	Rockfall Catalogue.....	41
6.2	Rockfall classification	44
6.3	Spatial and temporal distribution	47
6.3.1	Spatial distribution.....	47
6.3.2	Temporal distribution.....	49
6.4	Energy calculation.....	54
6.5	Magnitude frequency plot.....	55
6.6	Uncertainty estimation.....	56
7	Discussion and Conclusion.....	57
8	Acknowledgements.....	58
9	References	59
10	Appendix.....	62

LIST OF FIGURES, TABLES AND APPENDIX

Figure 1: Approximate location of the Moosfluh DSGSD in yellow and the fast moving part in red	11
Figure 2: Total stations and reflector monitoring network in Aletsch	12
Figure 3: Geological map of the Aletsch region including lineations measurements	13
Figure 4: InSAR measurements of the Moosfluh DSGSD displacement	15
Figure 5: Rock slope failure (a) and vertical displacement (b) of the Moosfluh DSGSD	16
Figure 6: Typical rockfall seismic signal in helicorder (up) and seismogram views (down)	17
Figure 7: Driest (A) and Cazulecher (B) total stations and raspberry shake seismometers	18
Figure 8: Raspberry shake 4D seismometer (A) and seismometer installation in the field (B)	19
Figure 9: Seismic data showing the helicorder view in the background and a zoom on a rockfall in helicorder and seismogram views.	19
Figure 10: Webcam in Driest oriented towards the landslide, taking photos every 10 minutes	21
Figure 11: Picture captured by the webcam in Driest. Photo taken the 23.07.2017 at 08h02 UTC	21
Figure 12: Bad conditions on webcam; night(a), bad weather(b), morning light(c), evening light(d)	22
Figure 13: Orthophoto of the Aletsch region	23
Figure 14: High-resolution photograph of the Moosfluh DSGSD	23
Figure 15: Field installation of the Leica vector and measurement explanation	24
Figure 16: Main steps followed during the thesis	25
Figure 17: Rockfall event of the 27.7 at 17h37 at the 3 stations in helicorder and seismogram view	27
Figure 18: Event of the 27.7.2017 at 17h37 on the webcam before, during and after the event	27
Figure 19: Local earthquake of the 24.9.2018 at 23:48 UTC	28
Figure 20: Teleseisms of the 19.9.2018 at 14:39 UTC	29
Figure 21: Spider plot for local earthquake	30
Figure 22: Spider plot for teleseisms	31
Figure 23: Spider plot for rockfalls	31
Figure 24: Calculation of the peak amplitude and event duration from the raw signal	32
Figure 25: Rockfall having lower noise before than after the event	33
Figure 26: GCPs matching between the high-resolution photograph and the DEM	36
Figure 27: map view of the photo georectification	37
Figure 28: Example of block volume measurement from the georectified photo	38
Figure 29: Soil classification for RockyFor3D	39
Figure 30: Correlation between the duration and the energy	40
Figure 31: Summary of the main seismic parameters of the rockfall catalogue as boxplot	43
Figure 32: Time-series of amplitude (only the largest amplitude event of each day is shown)	43
Figure 33: Number of event in each rockfall category	44

Figure 34: Spider plot and corresponding seismic signal for the 7 rockfall categories	46
Figure 35: Main features of the DSGSD fast moving part	48
Figure 36: Source and deposit of the 20 selected events measured by the Leica vector	49
Figure 37: A) Cumulative number of events (blue) and B) surface displacement of reflector 72	50
Figure 38: Daily precipitation data and daily rockfall events between July 1 st and October 31 st 2017	51
Figure 39: 1 week moving average of the temperature in Catzulecher (July 2013 - November 2017)	52
Figure 40: Typical temperature of a September day in Catzulecher	52
Figure 41: Event distribution across one day (time in UTC, local time = UTC + 2)	53
Figure 42: Rockfall modeling with RockyFor3D giving the kinetic energy (kJ)	54
Figure 43: Magnitude frequency plot with the energy estimation and cumulative frequency	55
Table 1: Main parameters of the 20 selected events for measurement with the Leica vector and georectification	34
Table 2: error estimation of the main parameters	56
Appendix 1: Different noises and unknown signals observed between July and October 2017	62
Appendix 2: Rockfall event visible on webcam photo but not on the seismic signal	63
Appendix 3: extract from the event catalogue built from seismic data	63
Appendix 4: Georectification of the Geoprævent photo with PRACTISE	64
Appendix 5: Description of input parameters needed in RockyFor3D	64
Appendix 6: input parameters for rocky for 3D	65
Appendix 7: output files from RockyFor3D	66
Appendix 8: Most important output from RockyFor3D	66
Appendix 9: night noise at the cable car station	67
Appendix 10: source and deposit coordinates of the 20 selected events	67
Appendix 11: Heavy rain in Catzulecher on the 10th of August between 22h30 and 22h45 (up) and a zoom between 22h41 and 22h42 (down).	68

1 INTRODUCTION

Worldwide most glaciers have been retreating during the past decades (VAW/ETHZ & EKK/SCNA, 2015) leading to debulking and stress changes in slopes adjacent to glaciers (Geertsema and Chiarle, 2013). These changes lead to an increase in landslides and rockfalls in critically stressed oversteepened slopes (Cossart et al., 2008, Borgatti et Soldati, 2013). In addition, these failures are likely to turn into rock avalanches, debris flows, or landslide dams, hazards susceptible to damage downhill villages, infrastructures, or injure inhabitants and hikers. This problem will gain more and more importance in the future together with climate change and increasing temperatures leading to more and faster ice melting (IPCC Fifth Assessment Report, 2013).

Landslide masses dominate glaciated landscapes, nevertheless, mechanisms and timing of mass movements are difficult to describe (Agliardi et al., 2009). In recent literature relevant to this topic, open questions include: What is the temporal delay between large slides and glacier melt? Which geological conditions favor slope instability or how is stress varying with time? How long are large slope instabilities active? Is their failure catastrophic or progressive? How is the spatial and temporal occurrence of rockfalls associated to large mass movements? What are the main triggering factors of catastrophic failure?

This project focuses on the analysis of the Moosfluh deep-seated gravitational slope deformation (DSGSD) located on the southeastern flank of the great Aletsch Glacier in Wallis, Switzerland. Being active today, this location provides a unique opportunity to challenge some of the above-listed questions. The Moosfluh landslide has been (and still is) widely investigated. Recent studies focus on its geometry, kinematics and displacement pattern (Kelly et al., 2004, Strozzi et al., 2010, Kos et al., 2016, Grämiger et al., 2017). The 150-200 Mm³ (Manconi et al., 2017) rock mass has been moving of several centimeters per year since the 1980th (Strozzi et al., 2010). In 2005, it underwent exponential acceleration to reach displacement in the order of tens of centimeters per year (Strozzi et al., 2010, Kos et al., 2016). In 2016 a 2 Mm³ (Manconi et al., 2017) superficial part of the slide underwent large acceleration reaching displacements up to one meter per day (Loew and al., 2017). Such a severe evolution induced new tensile cracks leading to an increase in rockfall activity expressed by numerous events every day. Studying the interaction between spatial/temporal rockfall occurrence pattern and surface deformation is critical for a better understanding of the DSGSD kinematic and allows new insights into triggering mechanisms. The surface displacement is already well monitored by a network of reflectors measured by a Robotized Total Station (Loew et al., 2017, Manconi et al., 2018b) but the rockfall events were so far only captured by a webcam located opposite to the active slope. Moreover the webcam allows events identification only during daytime, provided good weather and light conditions. To fill this monitoring gap, seismic sensors appeared to be the most convenient solution. Indeed seismometers can be installed at safe distance from the active parts of the slope, they allow continuous monitoring over long time period and are independent of weather and light conditions. Previous studies (Deparis et al., 2008, Helmstetter and Grambois 2010, Zimmer and Sitar 2015, Dammeier et al., 2016, Manconi et al., 2016, Dietze et al., 2017a) revealed that

recording rockfalls with seismometers is feasible at local and regional scales and that specific parameters of the seismic signal can be linked with rockfall properties such as their energy, velocity, volume, runout distance, duration and location of events (Hibert et al., 2014, Dammeier and al., 2011). With the growth of regional and global seismic networks simultaneously with the development of low-cost sensors, seismic recently drew the attention of many scientists seeing new applications. Here a network of 3 low-cost seismic sensors (Raspberry Shake) was installed around the DSGSD with the aim to build a rockfall catalogue. This study focuses on the period between the 1st of July and the 31st of October 2017, months during which the largest rockfall activity was expected. However, the monitoring network is still actively retrieving continuous seismic data since more than one year.

2 GOALS

The primary goals of this thesis are to learn about rockfalls properties and distribution in space and time, compare seismic monitoring with surface deformation and study the DSGSD kinematic and possible trigger mechanisms in Moosfluh. Secondary goals are to investigate the ability of low-cost seismometers to record, identify and characterize rockfalls in a local seismic network.

2.1 Key Questions

- *What is the Spatial and temporal distribution of the rockfalls in Moosfluh?*

Spatial and temporal distributions are important to characterize a rockfall area, understand the mechanisms and mitigate risk. Continuous monitoring allows new insights in the temporal distribution of rockfalls and the complementary optical methods allow investigation of the spatial distribution.

- *What are the properties (runout distance, volume, energy) of the rockfalls in Moosfluh?*

With seismic data, indirect measurements of the rockfalls are made through the amplitude and duration of the signal. The goal here is to use additional remote sensing methods to correlate seismic data with physical properties of the rockfalls.

- *How do meteo-climatic conditions (Temperature, precipitation) influence rockfalls occurrence?*

The climate is known to influence rockfalls, especially as trigger during extreme events. It is interesting to investigate how temperature and precipitation influences the number of rockfall to identify driving parameters and trigger mechanisms.

- *How does the distribution of rockfalls correlate with surface deformation from other measurement types (e.g., in-situ and/or remote sensing)?*

Estimating uncertainty is important to assess the quality of the data. Moreover having several methods measuring the same phenomena gives validation, strengthen the results and supplement the dataset.

3 BACKGROUND

This section presents the study area, the existing monitoring network, the current knowledge of the Moosfluh DSGSD and passive seismic as a tool to record rockfalls.

3.1 Study area

The study area is located nearby the current (2017) tongue of the great Aletsch glacier in Wallis, Switzerland. The latter is the largest glacier in Europe with a length of 22 kilometers and a maximum thickness of 900 meters. As most glaciers in the Alps, it has been retreating during the past 150 years. Indeed the Aletsch glacier is more than 3 kilometers shorter today and lost a thickness of about 300 meters (VAW/ETHZ & EKK/SCNA, 2015, Pro Natura, 2017). The Moosfluh DSGSD is located southeast of the current glacier tongue in a critically stressed and over-steepened slope. It has a volume of 150-200 Mm³ undergoing an overall displacement of few centimeters per year (Manconi et al., 2017) and comprises a 6 Mm³ (Franziska Glüer) faster moving part. Kos et al., (2016) described toppling as the main mechanism driving the landslide. Figure 1 shows the approximate DSGSD extent in yellow, the faster moving part in red and the seismometers locations in purple.

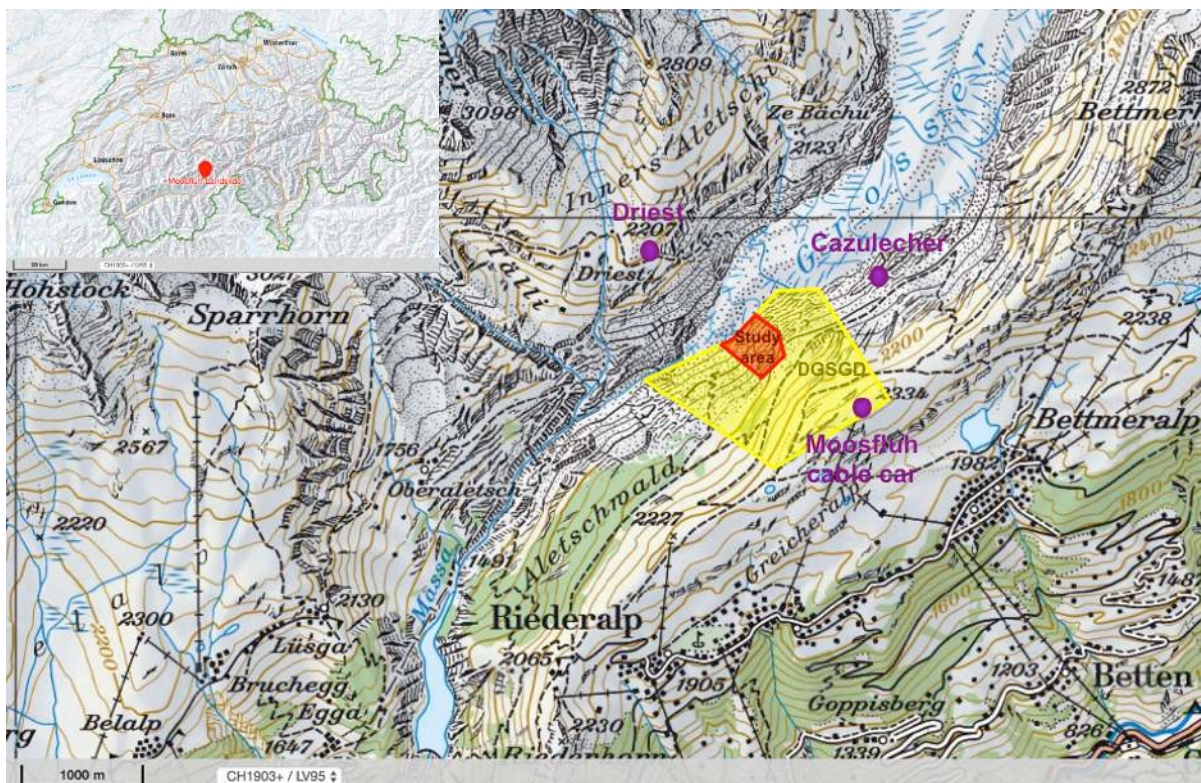


Figure 1: Approximate location of the Moosfluh DSGSD in yellow and the fast moving part in red. In purple are the locations of the three seismic stations (Cazulecher, Driest, and Moosfluh cable car) (Swisstopo, 2017b)

3.2 Existing Monitoring Network

Monitoring is ongoing in Moosfluh since 2013 with an in-place GPS and two total stations in Driest and Cazulecher measuring 85 reflectors as shown in Figure 2 (Manconi et al., 2018b). The reflectors are located in different parts of the slope, inside and outside the DSGSD perimeter. The ones located outside the DSGSD are reference point assumed to be stable, while the others are located inside the DSGSD at different locations capturing differential displacement at the boundaries and between the fast and slower moving parts. Unfortunately, many reflectors failed during rockfall events in the fast moving part and cannot be reinstalled due to safety issues. Therefore, reflector 72 located just above

the fast moving part was used as reference for surface displacement during comparisons. Moreover several reflectors are also located on the other valley flank to capture eventual movements and ensure that the measurements made from Driest total station are related to the Moosfluh DSGSD or to correct them if displacements are measured at Driest total station. Indeed another DSGSD is located around Driest, whose displacement is measured with the reflector network on that slope. Additionally, a webcam is installed in Driest, and since September 2016 takes photos of the landslide every 10 minutes. Finally, 2 weather stations recording temperature and pressure are located in Driest and Catzulecher. Daily Precipitation data are taken from the Bruchji station (MeteoSwiss, 2017) located 6 kilometers southwest of the center of the DSGSD.

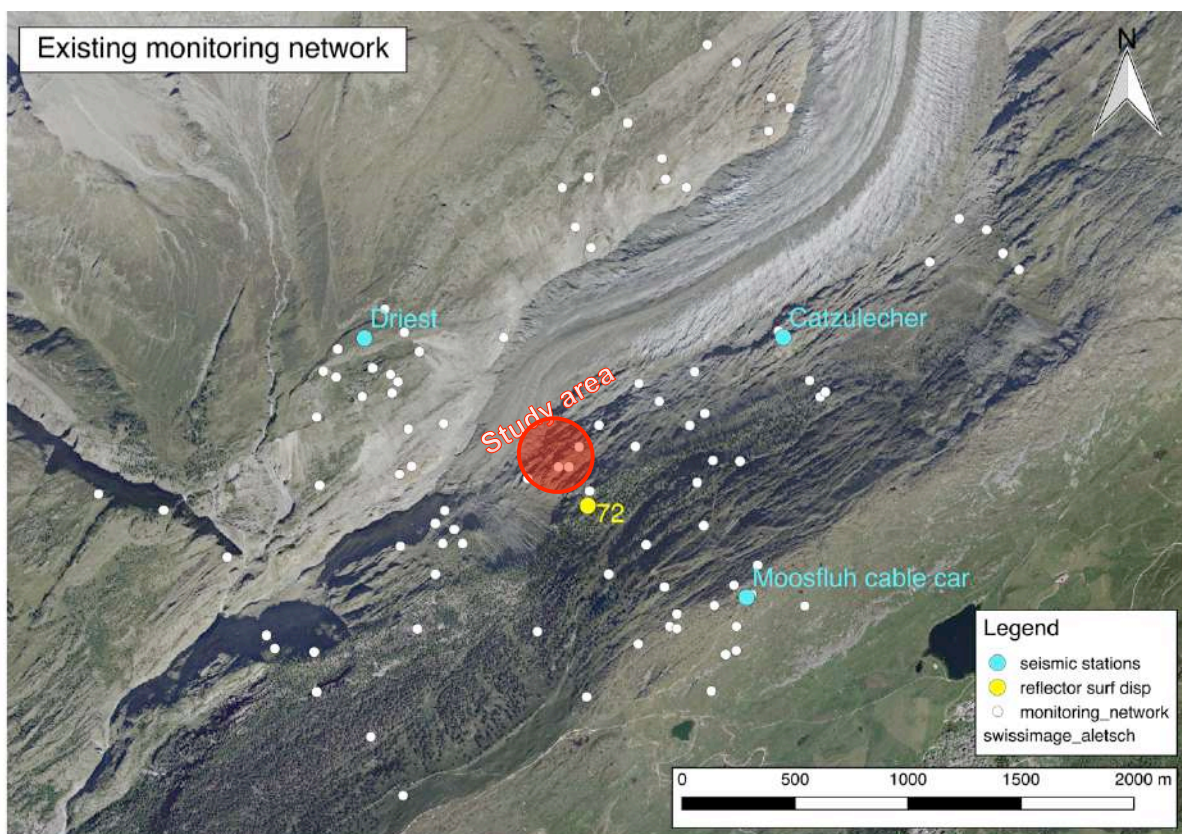


Figure 2: Total stations and reflector monitoring network in Aletsch. 2 total stations are present in Driest and Catzulecher. The reflector 72 was used to compare the surface deformation as the others in the fast moving part failed.

3.3 Geology

The Aletsch region occurs in the Aar massif, a poly-metamorphic gneiss body intruded around 280 million years ago (Permian), which is today part of the crystalline basement of the Alps. During the Alpine orogeny (18-12 million years, Miocene), it has been metamorphosed to the greenschist facies and deformed into a dome shape. Its sedimentary cover has been carried away and eroded until exposition of the gneiss basement in the Bernese and Lepontine Alps. The rocks exposed in Aletsch are leucocratic and granitic gneisses (Figure 3). They are mainly composed of alkali feldspars (albite and microcline) and quartz (Crisinel, 1978). Three lineations are apparent in the region, the most prominent one is the alpine schistosity, which is steeply dipping toward southeast (dip direction 122° /dip angle 76°), the joints are persistent (3-10 meters) and have a spacing in the centimeter range

(Grämiger et al., 2017, Crisinel, 1978). The second one is dipping very steeply toward south-southwest ($198^{\circ}/83^{\circ}$). It is less persistent (1-3 meters) and has a medium spacing (0.5-2 meters). The third one is gently dipping towards Southwest ($240^{\circ}/20^{\circ}$), has a persistence of 3 to 5 meters and a spacing of 1 to 5 meters. A fourth lineation can be described; large-scale fault zones striking parallel to the alpine schistosity (Northeast-Southwest) (Grämiger et al., 2017). The rock mass is described as blocky, with a GSI (geological strength index) between 65 and 80 (Grämiger et al., 2017).

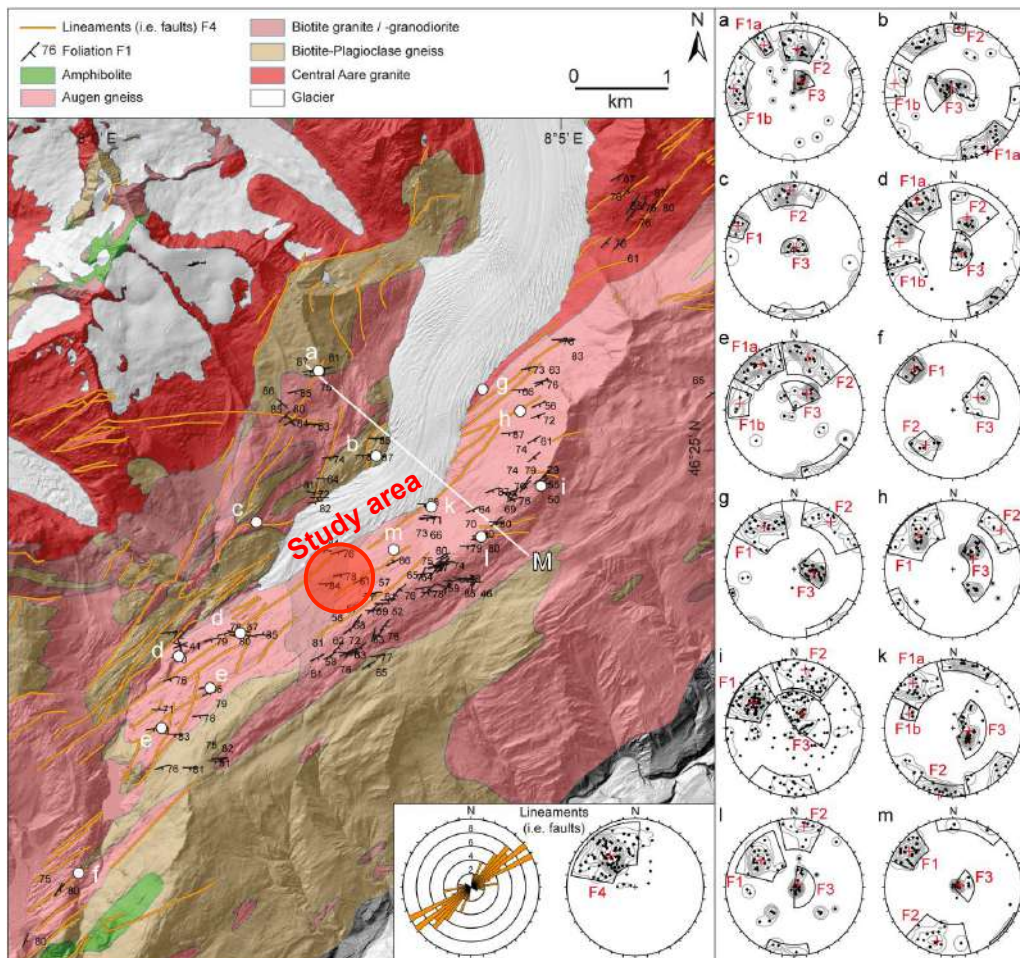


Figure 3: Geological map of the Aletsch region including lineations measurements (Grämiger et al., 2017)

Since the late Pleistocene (100'000-10'000 years ago), the climate has been fluctuating between warmer and cooler periods inducing several glacial advance and retreat cycles (Schindelwig et al., 2011), which can be observed in the field by at least three moraines in Moosfluh (Grämiger et al., 2017). Grämiger et al. (2017) suggest that slopes located under the little ice age moraines have been affected by at least five cycles, while above this limit only the Last glacial maximum (17'000 years ago) reshaped the slopes in Aletsch. About half of Moosfluh DSGSD is located under the little ice age moraine, including the studied fast-moving part.

Grämiger et al. (2017) investigated the mechanisms causing failure in the Aletsch region with numerical simulations. They showed that pure mechanical loading of the slope has only limited influences on creating new damages, while ice fluctuation (fatigue process) and bedrock erosion has significantly larger influences. These actions induce stress amplitude changes, stress redistribution,

fracture propagation and slip leading to degradation of the rock mass strength preparing it for failure during the next ice loss. Furthermore, Kos et al. (2016) have investigated the timing of debuttressing and found that slope response to stress changes was happening within one decade after ice retreat.

Along the Aletsch glacier, Kos et al. (2016) reported at least seven slope deformations on both sides of the valley including at least two active ones. According to Strozzi et al. (2010), Moosfluh landslide was already active before the young Dryas (12'900-11'700 years ago). Nevertheless, no lasting activity took place during the Holocene (10'000 years ago-now), and it is only during the 1990th that the landslide was reactivated. At the slope scale, a kinematic analysis based on joint sets measurements and GIS-based mapping identified toppling as main mechanisms and slope stability was assessed as critical (Kos et al., 2016). In the field, large ridges, grabens, scarps and counterscarps strengthen these results. The slope is mostly outcropping disintegrated bedrock and steep talus slopes with rockfall deposits of various sizes from centimeter to several meters. The mean slope angle from the top of the fast moving part down to the glacier is about 40° (map.geo.admin.ch, 2018).

3.4 Recent movements

The surface deformation of the Moosfluh DSGSD has been studied with synthetic aperture radar interferometry (InSAR). The latter is an active remote sensing technique analyzing the phase difference of 2 or more radar images to generate maps of surface deformation (Bürgmann et al., 2000). Figure 4 presents displacement rate from InSAR data in the superficial part of the Moosfluh DSGSD. Slow linear increase in displacement rate can be observed until 2005 (Strozzi et al., 2010, Kos et al., 2016) followed by an exponential increase until autumn 2016. At that time, the landslide underwent an unexpected large acceleration, moving up to one meter per day in some parts and creating the large head-scarp of the fast moving part. During winter of the same year, the displacement stabilized at a rate of five centimeters per day (Manconi, 2017). In summer 2017 similar but smaller acceleration (up to 30 centimeters per day) took place in the same area (Manconi et al., 2018a). Associated with these large displacements many rockfalls and partial failures occurred in the slope. In addition to those failures, the creation of new scarps, counterscarps, grabens, trenches and tensional openings was observed (Kos et al., 2016). Furthermore, Figure 4 shows that since 2011, failure events are decreasing in number but increasing in volume. This observation raises a critical question concerning the future evolution of the DSGSD; will this trend continue and lead to catastrophic failure or will it change and turn into more progressive failure?

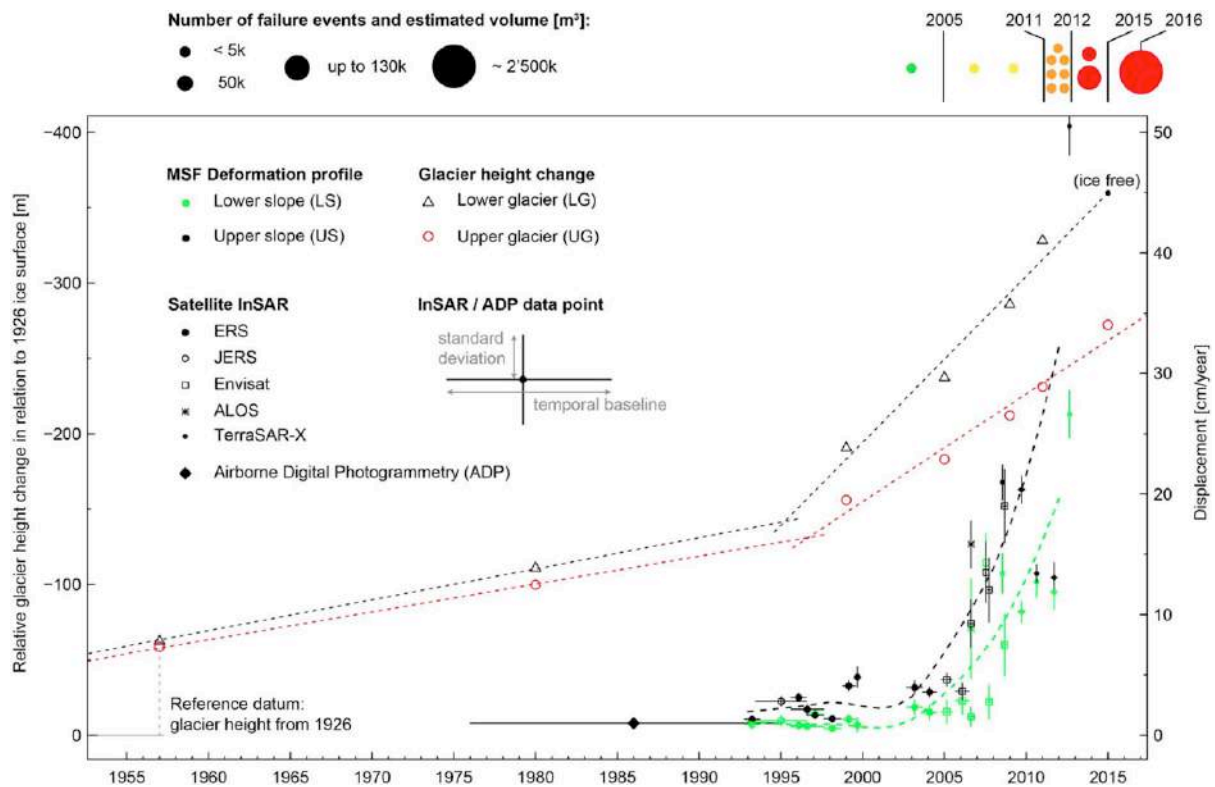


Figure 4: InSAR measurements of the Moosfluh DSGSD displacement (Kos et al., 2016)

Figure 5 shows the evolution of the landslide most active part focusing on the period after 2005. Between 2012 and 2015, many active structures and rock slope failures were observed (Figure 5a). During this period the displacement reached the critical threshold of 25 centimeters per year. Strozzi et al. (2010) discovered that larger displacements developed in the middle of the slide, trend visible in Figure 5b (blue-purple). Differential displacement is observed through the landslide with both subsidence and uplift. Subsidence and volume loss reach 14 meters in the middle and toe of the slide. These changes are linked to flat topography and formation of graben structures. On the contrary, positive surface changes up to 4.5 meters can be observed associated with steep topography and uphill counterscarp, visible in red on Figure 5b (Kos et al., 2016). These structures initiated by debuttressing of the slope toe where ice loss decreased confining pressure and left empty spaces. In summary, debuttressing generates local failures at the toe, which controls toppling and sliding processes higher in the slope causing rock failures (Kos et al., 2016). Finally the DSGSD can be seen as additional predisposing factor, whose motion accelerates the rockfall phenomena in Moosfluh. It helps rock-mass disintegration and acts as the extra disturbance needed to generate failures in this already critically stressed slope. Other factors, such as rainfall and snowmelt are common triggering events and affect Moosfluh as well (Kos et al., 2016).

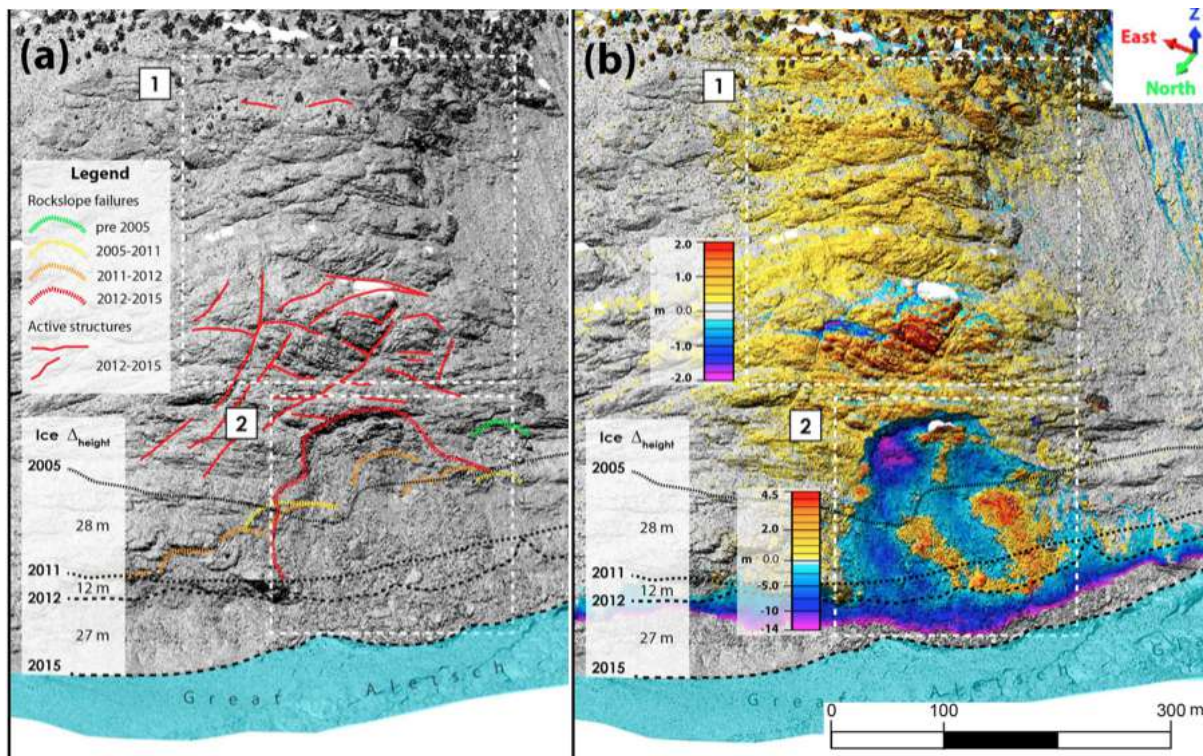


Figure 5: Rock slope failure (a) and vertical displacement (b) of the Moosfluh DSGSD (Kos et al., 2016)

3.5 Passive seismic monitoring to study rockfalls

Many phenomena generate vibrations that are detectable as seismic waves comprising both natural (wind, rain, volcanic eruption, rockfalls) and anthropic phenomena (helicopter, planes, cable car, explosions). All these waves propagate into the ground and are measurable by seismometers kilometers away from their source location. Each phenomenon has unique signal characteristics (frequency range, duration, shape) making the identification, classification, and characterization of individual events possible (Kortström et al., 2015). Many studies focus on identification of these parameters to identify rockfall seismic signals and discriminate it from other phenomena such as earthquake or blasts. The main parameters used for identification and classification of events are the frequency range, the duration and the envelope shape (Deparis et al., 2008, Zimmer and Sitar, 2015 and Hibert et al., 2014). Rockfalls have typical predominant frequencies from 3 to 10 Hz, the duration generally ranges from 5 to 30 seconds and they have triangular envelope shapes (Figure 6).

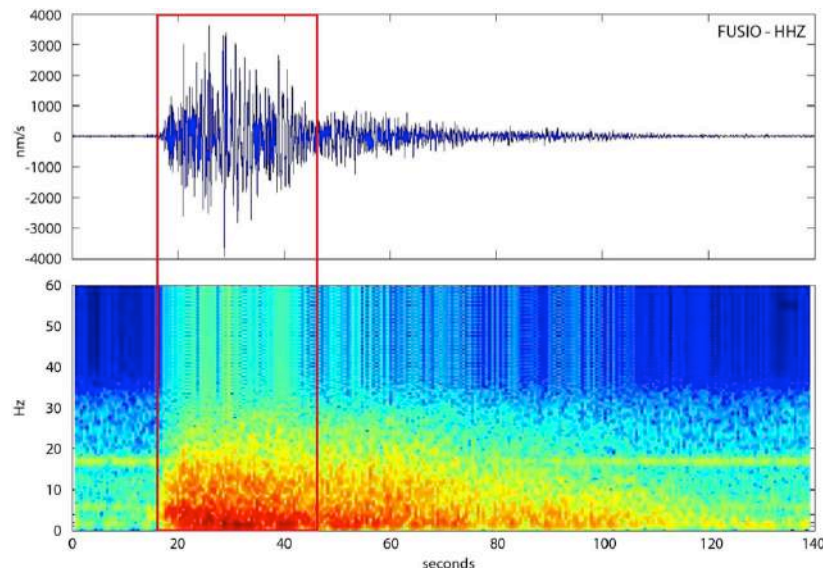


Figure 6: Typical rockfall seismic signal in helicorder (up) and seismogram views (down) (Dammeier et al., 2016)

After identification, the next step is to correlate the seismic parameters to physical characteristics of the rockfalls such as the energy released, the runout distance, the location and the block volumes. Useful seismic parameters for this purpose are the event duration, the peak amplitude, the arrival time, and the envelope area (Dammeier et al., 2011). Comparing arrival times at several stations allows the location of events, while an empirical relationship has been built to estimate rockfall volume from the duration magnitude (Manconi et al., 2016, Hibert et al., 2014). Moreover, Deparis et al., (2008) have detected a correlation between event duration and runout distance allowing estimation of the latest from the seismic signal alone.

Many research studies focus on automatic identification and classification of events. If successful, this approach would allow the detection of critical mass movements using seismic networks and thus to develop early warning and fast response systems based on seismic data (Satriano et al., 2008). Classification methods and criteria already exist to discriminate rockfalls from other events (teleseism, local earthquake, blasts, helicopter, etc.) (Zimmer and Sitar, 2015). Nevertheless, several technical challenges are still under research to produce working algorithms. An example of challenging task is the picking of onset time in gradually increasing signals that are rockfalls. In contrast, earthquakes exhibit sharp changes making the onset time obvious. One approach is the use of STA/LTA ratio (short-term average over long-term average), as triggering criterion (Dietze et al., 2017). Alternative methods such as the use of higher order statistics allow more accurate picking (Hibert et al., 2014). Despite, the method has to be calibrated depending on the seismic sensors used, the local network setting, and the characteristics of the target mass movements.

4 DATA

This section gives a description of the data used in this thesis. Section 4.1 introduces the seismic network, the seismometers properties and the seismic data obtained. Section 4.2 and 4.3 present the webcam images and Swisstopo data used. Finally, section 4.4 describes the field measurements data acquired.

4.1 Seismic data

The seismic network built for this study is composed of 3 raspberry shake seismometers surrounding the Moosfluh active rockfall area (Figure 1). The first one is mounted in Driest (Figure 7A), 1 kilometer northwest of the study area on the opposite valley flank. The second one is fixed in Catzulecher (Figure 7B), 1.5 kilometers northeast of the study area on the same slope 50 meters above the glacier. The third one is installed at the cable car station of Moosfluh, 1 kilometer southeast of the study area, on top of the same slope. Potentially two more existing seismometers could be used to detect the largest rockfalls occurring in Moosfluh. The CH-FIESA seismometer located in Fiescheralp, 6 kilometers northeast of the landslide, and The CH-SBRS seismometer located in Brig hospital, 10 kilometers south-southwest of the landslide. Both are parts of the Swiss seismological service and data are available via the Orfeus website (orfeus-eu.org, 2017).

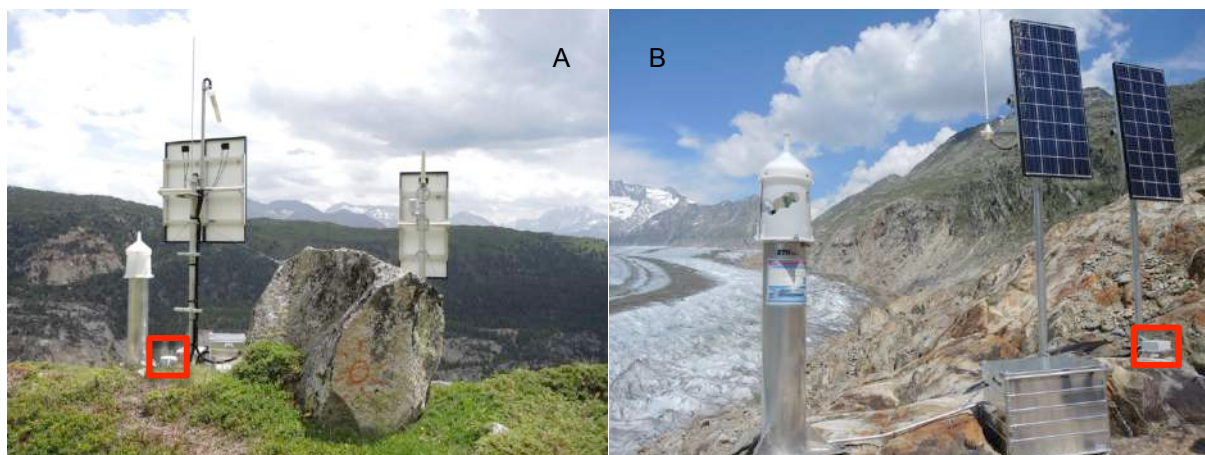


Figure 7: Driest (A) and Catzulecher (B) total stations and raspberry shake seismometers

Raspberry shakes are low-cost seismometers identical to the one presented in Figure 8A. They are composed of a single component 4.5Hz vertical Rachtotech RGI-20DX geophone with electronic extension to lower frequencies ($<1\text{Hz}$) (OSOP, 2017). Raspberry shakes have a sampling rate of 50 samples per second and a flat frequency band ranging from 0.7 to 19 Hz. The raspberry shake seismometers have been installed into a protecting box and screwed directly on the bedrock to ensure stability (Figure 8B). It was not possible to dig them into the ground to avoid some surface noises because of directly outcropping bedrock surrounding the stations and drilling shallow boreholes was too expensive. The raspberry shakes are connected to power with a cable to available power source of the monitoring stations (solar panels in Catzulecher and Driest, the cable car installation at the cable car). They have been installed in June and July 2017 and are all running since the 7th of July (Catzulecher and Driest were already recording in June). Since then continuous seismic data have been acquired with only minor gaps (minutes to hours) in the dataset at single stations. The seismic data is sent in almost real time to a computer at ETH and stored there. The files are saved as miniSEED; they are saved for each station every 24 hours. Moreover, the seismometer at Moosfluh cable car is in open access. The data are consultable and can be downloaded online through the raspberry shake website (<http://www.raspberryshake.org/stationview>).

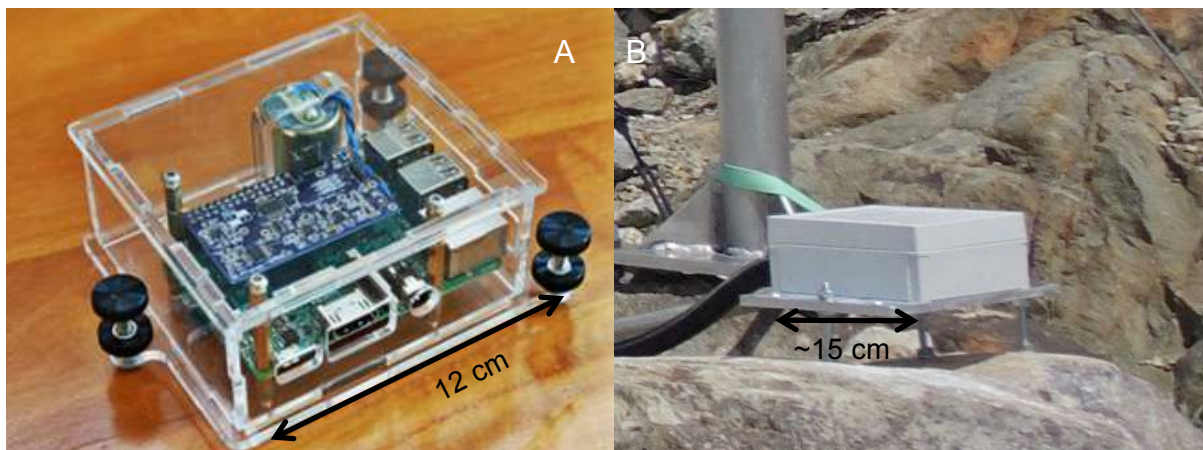


Figure 8: Raspberry shake 4D seismometer (OSOP, 2017) (A) and seismometer installation in the field (B). The grey box serves as protection and is screwed to the bedrock.

Figure 9 shows an example of the data obtained opened in the program SWARM (USGS, 2017b). That program allows a display of the data in helicorder, spectrogram and frequency views. From these data, events can be identified and classified based on typical seismic parameters; the onset time, the duration, the peak amplitude and the mean frequency. These parameters are the base for all following analyses and link to physical properties of the rockfalls.

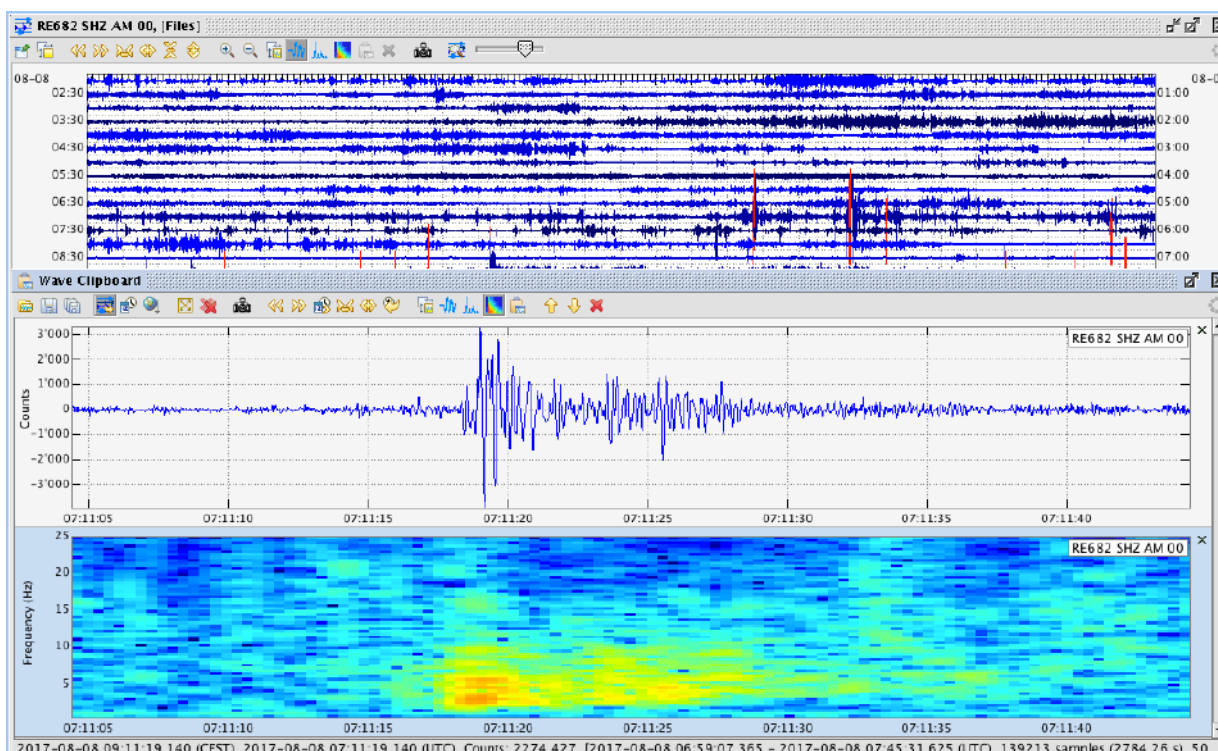


Figure 9: Seismic data showing the helicorder view in the background and a zoom on a rockfall in helicorder and seismogram views.

Many other signals were recorded by the raspberry shakes, which are not of direct interest for us and are classified as noise. Examples of the main ones are shown in Appendix 1. These noises can potentially be superimposed on rockfall signals masking the event or preventing accurate picking of the onset time. Three main noise sources were observed between July and October 2017. The first

one is the noise from Moosfluh cable car during its operating hours from 8h00 to 16h30 (local time). Since one of the seismometer (cable car) is located inside the top station of the cable car, vibrations and acoustic noises from the installation largely affect it. Nevertheless the signal in Driest and Catzulecher is not impacted by that noise. The second one is large-amplitude-single-spike signal ($8.5e-6 < 1.3e-4$ m/s) probably due to temperature changes inducing thermo-mechanical deformation. The third noise source is rainfall on the seismometers protection box. Rain is not observed at the cable car due to the protection brought by the station building. Similarly, the thermo-mechanical spikes are only rarely observed in Moosfluh thanks to the building protection against large temperature changes. Other less frequent but recurrent noises were observed as well, such as helicopter landing and taking off during field operations, which was observed at a single station. Military planes are regularly flying at different altitudes along the Aletsch glacier and when flying at low altitude, their noise can be identified in the seismic data. At the cable car, the building protects the seismometer from this acoustic noise. Other unknown and very rare or unique noise could as well be observed such as very low frequency noise, having very large wavelength and low amplitude ($2.1e-7$ to $4.3e-7$ m/s) observed at the three stations.

4.2 Optical data

Photographs are crucial part of this thesis, since they are used to confirm observation made with the seismic sensors and allow quantitative analyses of block locations, runout and volume. This chapter presents the different optical tools used.

4.2.1 Webcam images

A webcam is installed in Driest capturing the DSGSD every 10 minutes (Figure 10). The DSGSD is situated from 1 (slope bottom) to 2 (cable car station) kilometers away on the other side of the valley. The Mobotix M25 webcam used has a resolution of 5 megapixels, which gives at a distance of 1.2 km (distance to the study area) a pixel size of 60 centimeters. Blocks of about 5 by 5 meters were usually identified when comparing 2 photos taken 10 minutes apart. For larger temporal baselines, the 2 photos had more contrasts mostly due to changing light conditions making it more challenging to rockfall events. Usually only larger blocks (10 by 10 meters) were identified in these cases. Rarely, an event was identified on the webcam photos but was not visible in the seismic signal as the example in Appendix 2 illustrates. Besides, it is possible to see long-term changes in the slope by comparing photos taken about one month apart. The fast moving part of the DSGSD is clearly moving downward as a whole domain. In conclusion, the webcam is an excellent tool to validate observations made with the seismometers and to study the DSGSD kinematic, in particular the spatial component.



Figure 10: Webcam in Driest oriented towards the landslide, taking photos every 10 minutes to capture the rockfalls

Figure 11 is an ideal case of signal validation. Clouds from the rockfall are apparent on the photo and at the same time, a typical rockfall signal was detected on the seismometers. The event occurred the 23.07.2017 at 8h01:45 UTC on the seismometers lasting for about 22 seconds. The same event was then identified in the webcam photo taken the same day at 8h01:58 UTC, which is one of the 2 cases a photo was taken exactly during an event.



Figure 11: Picture captured by the webcam in Driest. Photo taken the 23.07.2017 at 08h02 UTC

Nonetheless, the webcam is often unable to record rockfalls within the 10 minutes temporal baseline due to darkness (Figure 12A), clouds (Figure 12B) or bad light conditions (Figure 12C and D). Even though it is more difficult, it is possible to identify events from photos having larger temporal baseline (several hours to several days). Nevertheless, it is more difficult to specify which rockfall corresponds to which signal when several events happen during the investigated time period. The only available criteria were the amplitude and duration of the seismic signal. It was assumed that the largest amplitude and longest duration were associated to the largest rockfalls and thus the largest block identified on the photos.

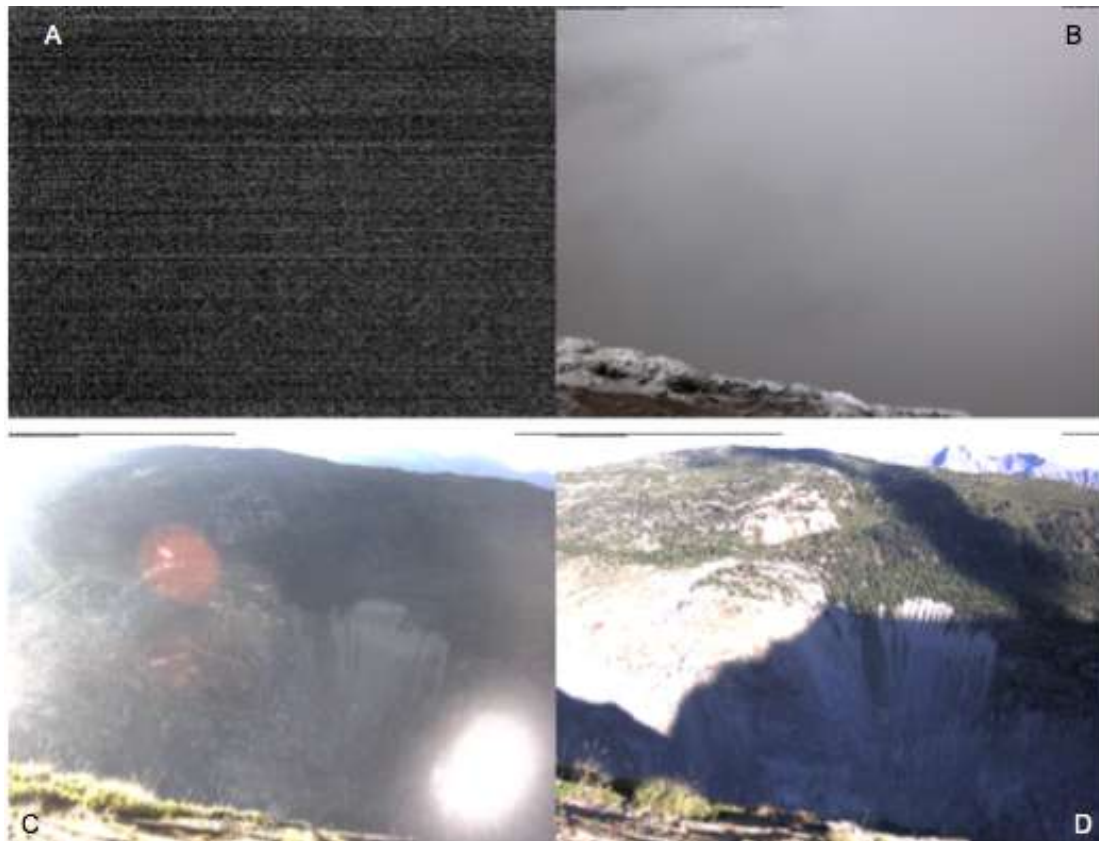


Figure 12: Bad conditions on webcam; night(a), bad weather(b), morning light(c), evening light(d)

4.2.2 Orthophoto

Orthophotos are georectified and orthorectified photographs to have a product free from distortions. The SWISSIMAGE25 databank from Swisstopo assembles orthophoto for the entire country (Switzerland). The final images have resolutions of 0.25 meters and 0.5 meters in mountainous areas (Swisstopo, 2016). The last orthophoto available (Figure 13) is from 2016 and was used as background to control the location of the identified rockfalls from field measurement and to produce ground control points for the georectification. Nevertheless the features are difficult to recognize in the fast moving part of the DSGSD due to local displacements reaching up to 70 meters since the photo was taken (1year).

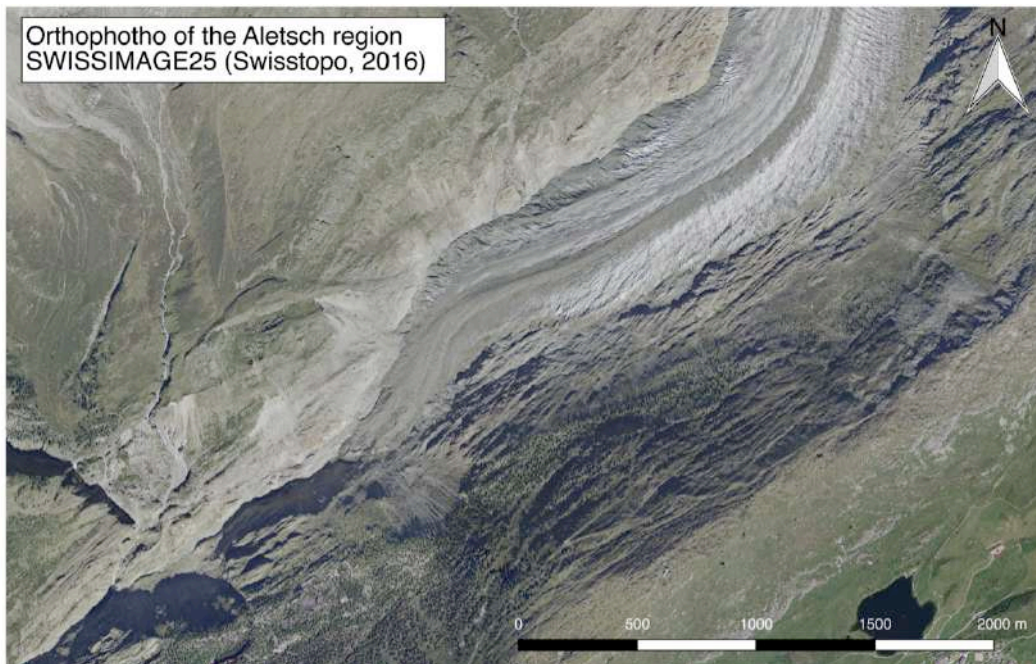


Figure 13: Orthophoto of the Aletsch region (Swisstopo, 2016)

4.2.3 High resolution photograph (Geoprævent)

The image used for georectification is a high-resolution photograph taken by the company Geoprævent (GEOPRÆVENT AG. (2018)). The camera is located 50 meters East-Northeast of the Driest Webcam capturing the entire DSGSD all the way down to the glacier (Figure 14). The camera is a Sony Alpha 7 R II equipped with a CMOS sensor of 42.4 megapixels having a width of 35.9 mm, a height of 24 mm and a focal length of 25 mm.

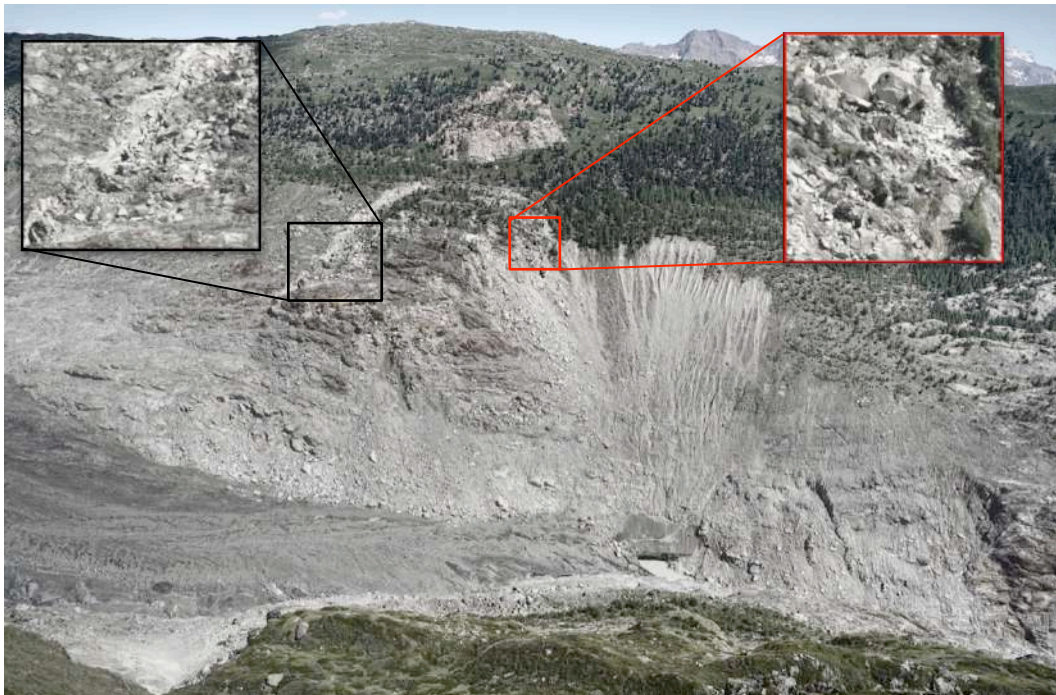


Figure 14: High-resolution photograph of the Moosfluh DSGSD (Geoprævent, 2018)

4.2.4 Digital elevation model (DEM)

The DEM comes from one of the Swisstopo database. It is part of the SwissALTI3D DEM reproducing the ground surface without vegetation and constructions (Swisstopo, 2017a). It covers the entire Switzerland and has a resolution of 2 meters. The data comes from airborne laser scans and high-resolution aerial photographs. It is used in this thesis as GeoTIFF format for QGIS and as ASCII X,Y,Z format for the georectification. The coordinate system is the LV03/CH1903 and has been changed in QGIS to the new Swiss coordinate system LV05/CH1903+ to match other data.

4.2.5 Leica vector

The Leica vector rangefinder is an instrument used to measure the position of target points from a distance (Figure 15). It is very useful when targets are not directly accessible or dangerous, such as blocks in the middle of active unstable slopes. The azimuth, distance, and inclination angle between a reference location and the wanted target are measured with a laser (Figure 15). Knowing the coordinate of the reference point, it is possible to back calculate the exact location of the target. The distance range of the instrument is 25 to 5'500 meters, which is well into the needed range of 1'000 to 2'000 meters from Driest to the blocks. At this distance, the accuracy is around ± 15 meters (Azimuth ± 10 mil, Inclination ± 3 mil, distance ± 5 m) according to the instrument specification (Vectronix, 2004). The measuring location (Driest) was the reference point, whose coordinates have been measured with a DGPS (Figure 15). All data acquired with the Leica vector were saved into the GPS and the final coordinates of the targets were automatically calculated. The goal was to measure the source and deposit of rockfalls recorded with the seismometers and identified with the webcam. For this purpose, 20 rockfall events (block source and deposit) were located on the webcam photos and measured in the field. Two reflectors at known positions were also measured with the Leica vector to assess the accuracy of the instrument and correct the model if necessary.



Figure 15: Field installation of the Leica vector and measurement explanation (Photo taken by Andrea Manconi)

5 METHODOLOGY

This chapter provides information about all steps followed during this project. A schematic view of these steps is presented in Figure 16. The different procedures done are displayed based on the 2 main data types; seismic and optical data. Output parameters obtained after the main tests are as well listed. The first 2 sections (5.1 and 5.2) describe events identification and classification. Then the calculation of all needed parameters is specified in chapter 5.3 and 5.4. Finally, magnitude frequency plots and energy calculation are presented in chapter 5.5.

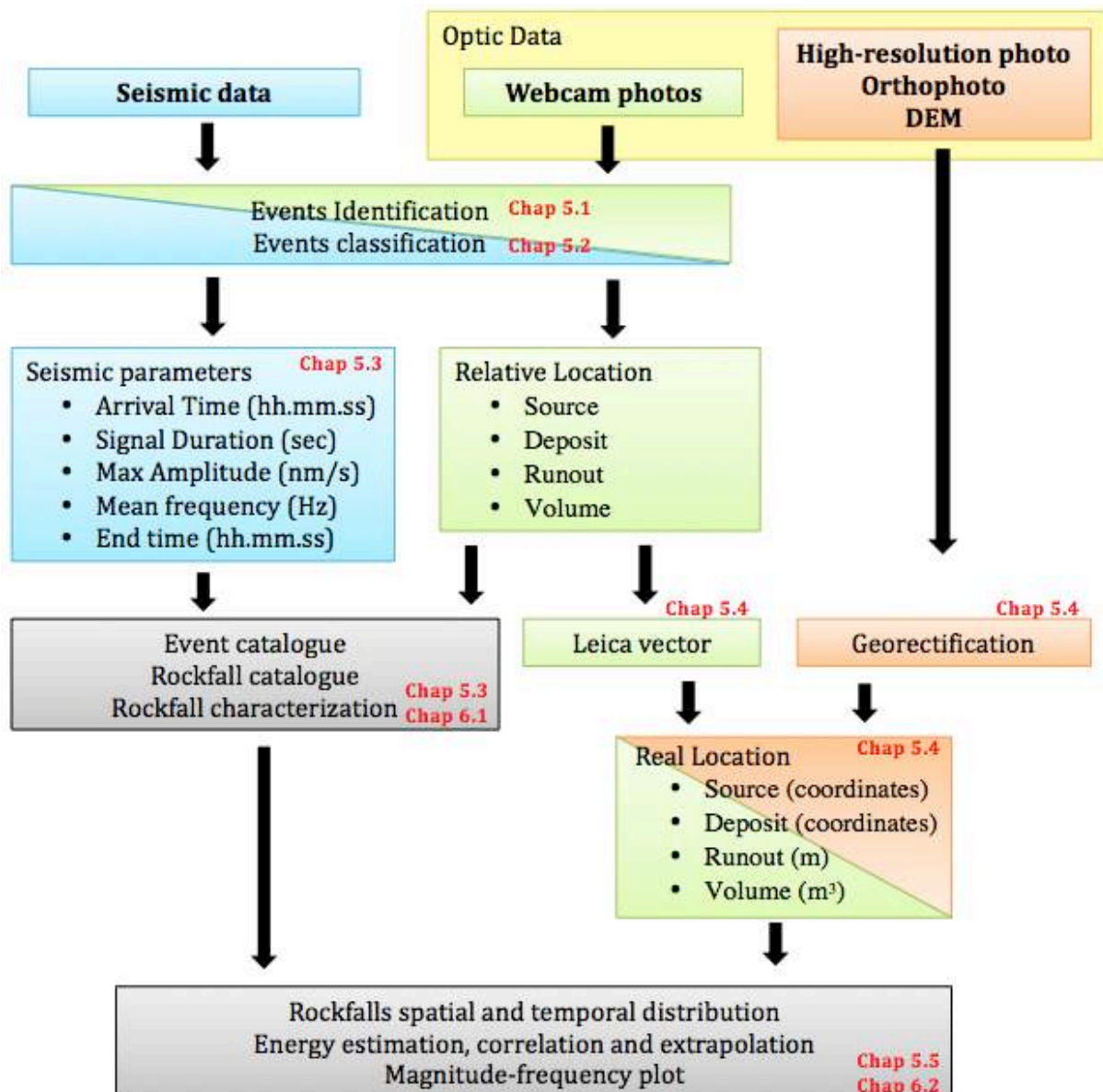


Figure 16: Main steps followed during the thesis

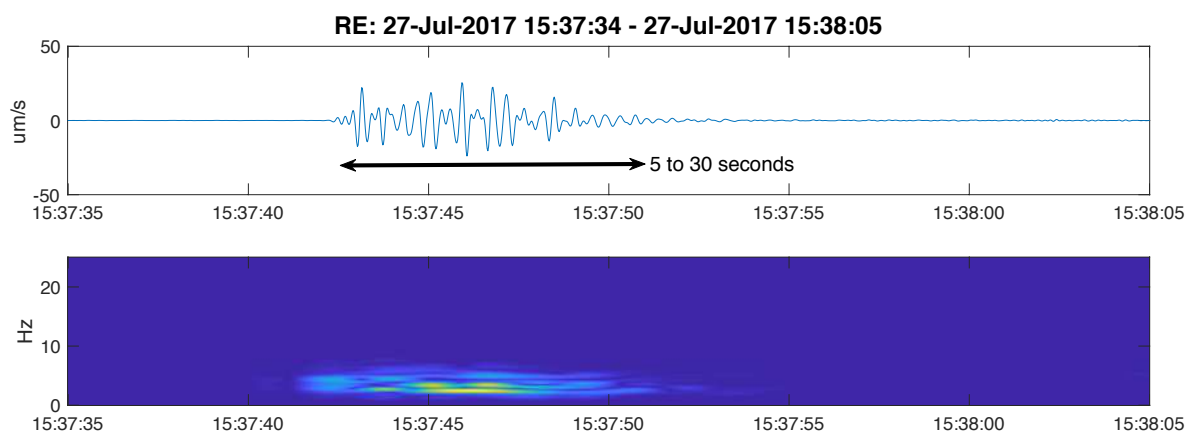
5.1 Events identification

First, we displayed the seismic data with the open source program SWARM (USGS, 2017b). The program allows quick access to the data in helicorder and seismogram views. It also allows easy filtering and enables the display of several stations at the same time. Events have been manually

identified focusing on the ones encountered at 2 or 3 stations. The identification focused on events with typical rockfall signals (see chapter 3.4) but most teleseisms and local earthquakes, as well as several unknown events were also described.

Once an event was identified, it was entered into an event catalogue (Appendix 3) listing the date and type of the event, the preliminary classification and a first approximation of the main seismic parameters, which are the duration, the peak amplitude at each station and the mean frequency. Then depending on the classification, further investigation to confirm the event was undertaken either through the webcam photos or in the earthquake catalogues. Note that not all rockfalls were seen on the webcam but all earthquakes were found in one of the two earthquake catalogues. The USGS catalogue was used for large magnitude ($M_w \geq 4$) distant (>100 km) earthquakes (USGS, 2017a) and the SED catalogue for low magnitude ($M_w \geq 0.5$) local (<100 km) earthquakes (seismo.ethz.ch, 2017). The following paragraphs give example of seismic signals for Rockfalls and earthquakes.

Figure 17 and Figure 18 show the rockfall event of the 27.7.2017 at around 15h37 UTC. It is an ideal case since the event can be well observed at the three stations as well as on the webcam. Figure 17 shows the seismic data at the three stations. The signal shows the typical characteristics for rockfalls its gradual onset, its mean frequency of 6 Hz and its average duration of 15 seconds. It is also typical for this dataset that the peak amplitude is the largest at the cable car, smaller in Catzulecher and the smallest in Driest. Moreover, the signal does not arrive simultaneously at all stations confirming the nearby occurrence of the event. For this event, the signal was first recorded in Catzulecher, then at the cable car and finally in Driest, which was the most frequently observed arrival pattern. After seismic identification and first characterization the webcam photos were examined. In that case the hole left by the fallen block is obvious (Figure 18 right) and even the cloud from the fall was captured (Figure 18 middle). The fallen block was partly identified, just under the detachment zone. The final step was to use Matlab to extract the seismic parameters (start, end, duration, amplitude) to have consistent quantification through the dataset. Note that this example is ideal since it was not always easy or even possible to detect the rockfall on the webcam photos. Nevertheless, no detection on the webcam did not mean no rockfalls. Indeed the resolution and meteorological conditions limited greatly this detection approach, which emphasize the beneficial use of passive seismic to monitor rockfalls.



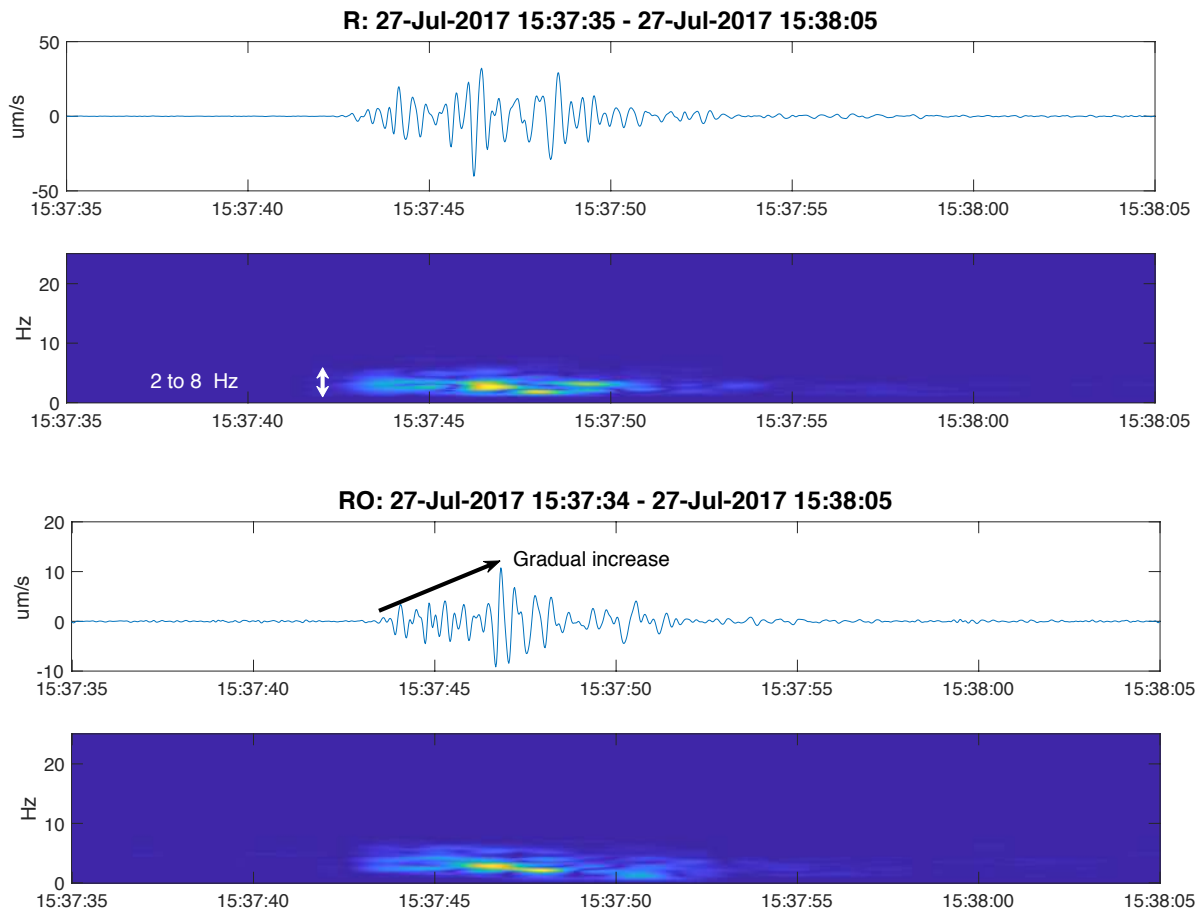


Figure 17: Rockfall event of the 27.7 at 17h37 at the 3 stations in helicorder and seismogram view. It is displayed between 17h37:35 and 17h38:05 UTC (right)

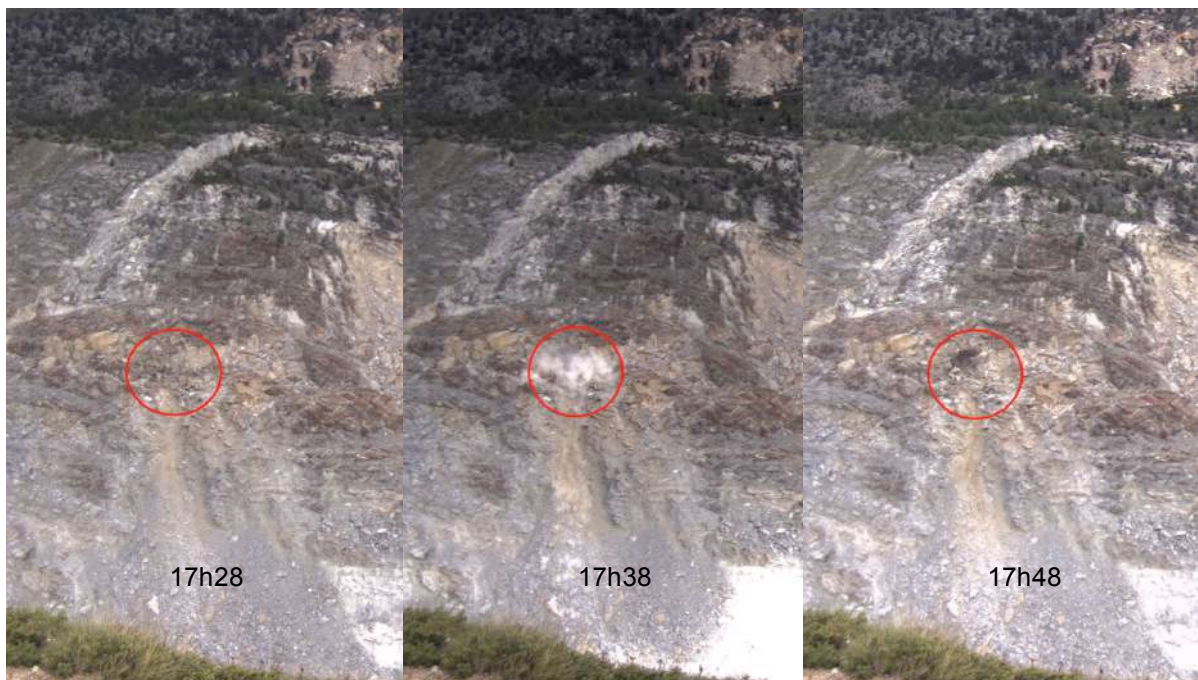


Figure 18: Event of the 27.7.2017 at 17h37 view on the webcam pictures. From left to right the photos show the area before, during and after the event (local time (UTC+2))

Local earthquakes are low magnitude (M_w : 1-3), nearby occurring (Switzerland and nearby region of France and Italy) earthquakes. The raspberry shake seismic network detects some of them. Figure 19 shows a typical local earthquake with sharp onset, relatively low duration and high frequency. The event has been searched and found in the SED earthquake catalogue (seismo.ethz.ch) where a description of the event is found with its location, time, magnitude and depth as well as helicorder data at several seismic stations as shown in Figure 19 (right). Here the timing and shape of the event was very similar to the one showed in the catalogue, confirming that it is indeed the same event.

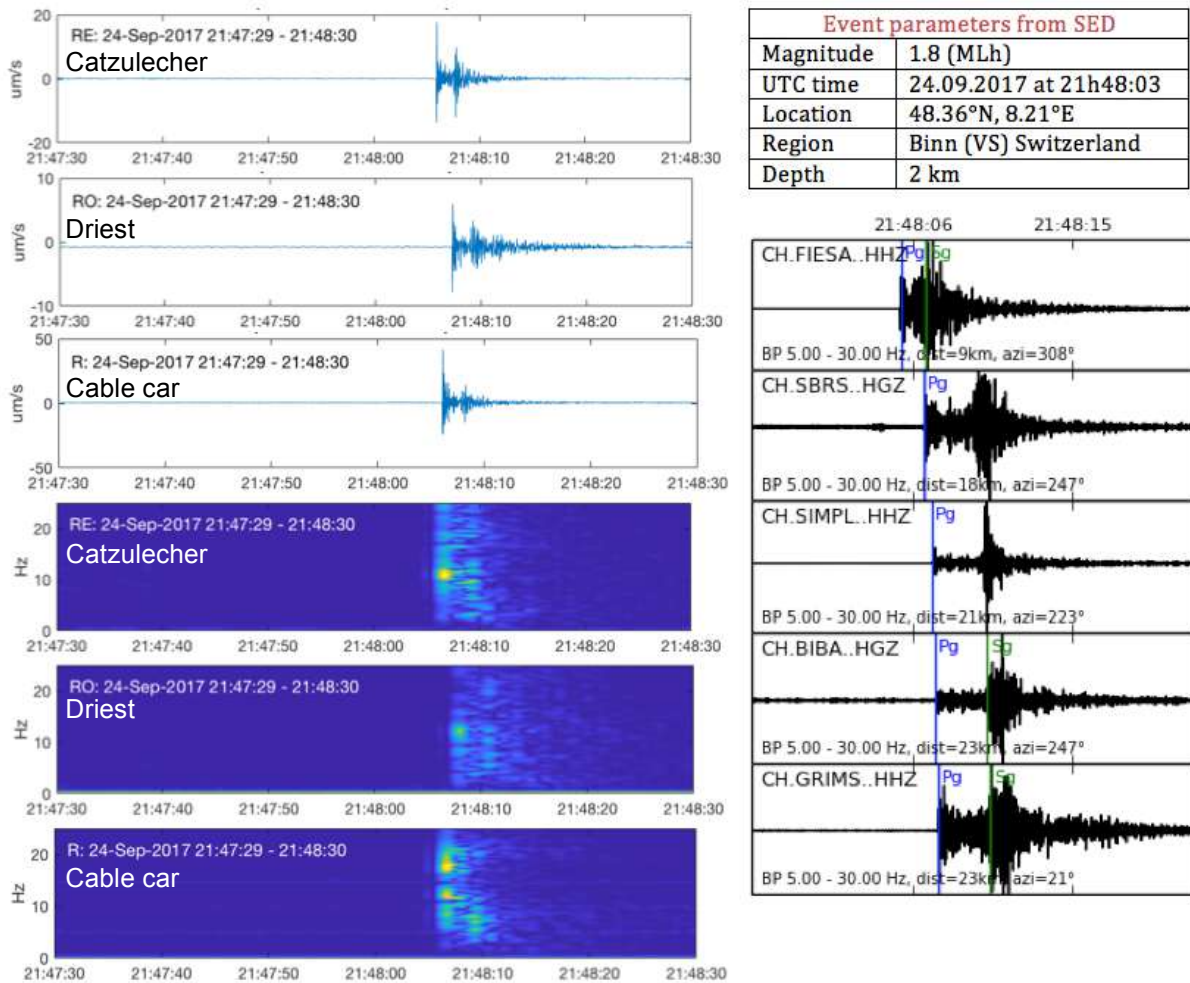


Figure 19: Local earthquake of the 24.9.2018 at 23:48 UTC. The earthquake view in matlab at our three seismic stations (left) and the earthquake details and data found in the SED earthquake catalogue (seismo.ethz.ch) (right) http://www.seismo.ethz.ch/en/earthquakes/switzerland/eventpage.html?originId=%27c21pOmNoLmV0aHouc2Vkl3NjM2Evb3JpZ2luL05MTC4yMDE3MDkyNTEMDg0Ny40MzE2MzcuNjlyODY=%27&date_ch=2017-09-24&time_ch=23:48®ion=Binn%20VS&magnitude=1.8

Beside local earthquake, our raspberry shake network detected many teleseisms, which are earthquakes of magnitude (M_w) larger than 4 occurring more than 100 km away from the monitoring location. Not all teleseisms could be detected due to the distance and magnitude combination. For example a magnitude 4.5 earthquake in Mexico (10'000km) is not detected but the same magnitude event occurring in Greece (1'500km) is. Figure 20 shows a teleseisms recorded by the three seismic stations. In the cable car station (Figure 20 left, 3rd station) the installation was running (noise at 18h29:30) but it was still possible to identify the earthquake even without filtering. Luckily, the event

onset was between the cyclic high amplitude peaks of the running cable car. The signal has the typical low frequency and long duration of teleseisms. Moreover, the event arrived at the three stations simultaneously, indicating a large distance separating the event to the stations. After looking into the USGS earthquake catalogue (USGS, 2017), a magnitude (Mw) 7.1 earthquake in Mexico was listed and occurred 13 minutes before its detection by our seismic network. After rough calculation of the distance (Mexico-Switzerland) and the wave velocity, the timing matches the recorded event in Moosfluh. Again, as shown in Figure 20 (right), the event location, time, magnitude and depth, as well as a shake map and helicorder data were available in the earthquake catalogue (USGS (2017) and ds.iris.edu).

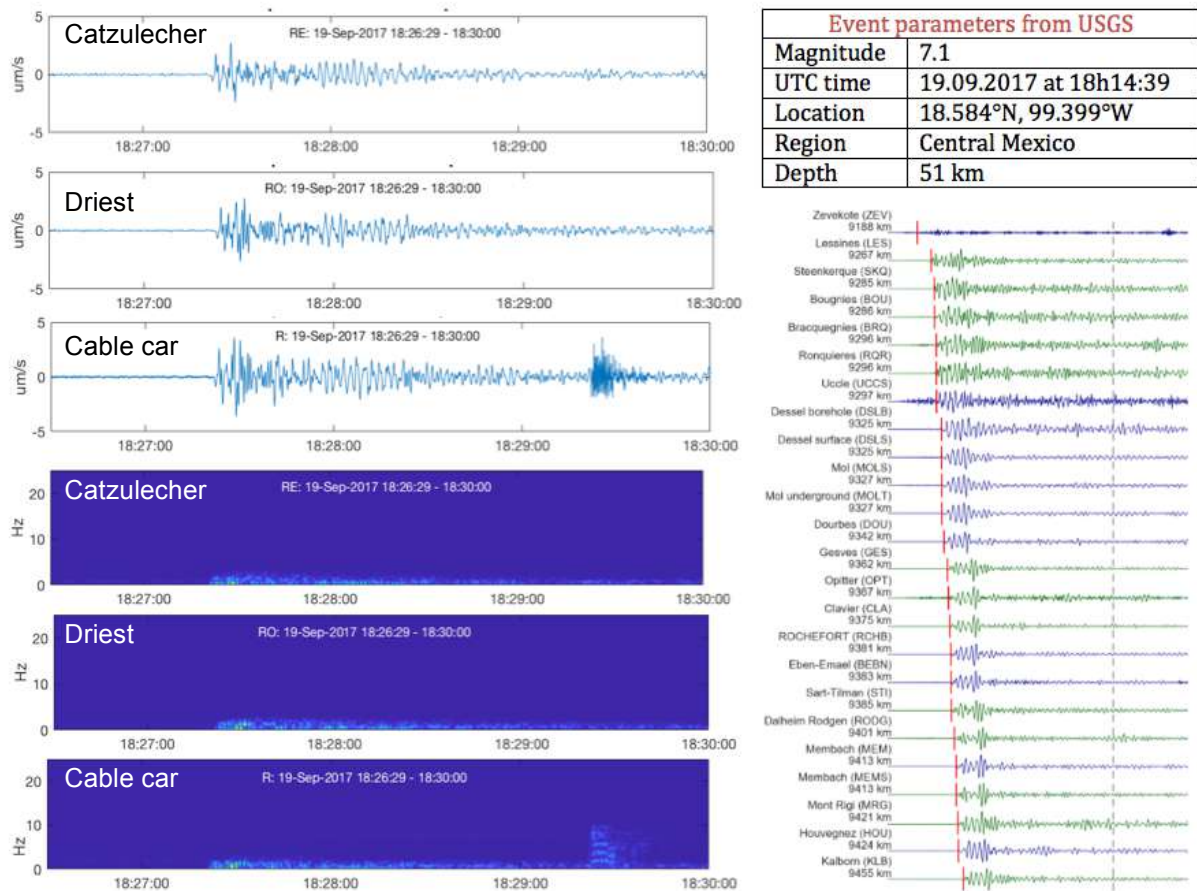


Figure 20: Teleseisms of the 19.9.2018 at 14:39 UTC. The earthquake view in Matlab at our three seismic stations (left) and the earthquake details and data found in the USGS earthquake catalogue (ds.iris.edu) (right) <http://ds.iris.edu/ds/nodes/dmc/specialevents/2017/09/19/central-mexico/>

5.2 Events classification

To confirm the preliminary classification, define more thoroughly typical parameters of each event class and have visual view of the results, spider plots were used. In these graphs, several parameters are plotted in a spider web where each parameter is plotted one radial line. As a result, each event has a specific shape and each shape is typical for one event type (ex: Figure 19). Here, five parameters have been plotted: the average frequency, the duration, and the peak amplitude at the 3 stations (Catzulecher, cable car and Driest). Each variable was normalized separately in order to have

the same scale on each axis (from 0 to 100). The following paragraphs presents the plots obtained for local earthquakes, teleseisms and rockfalls.

Figure 21 shows the results for local earthquakes. They typically have high frequency (the entire range from 2 - 25 Hz), low duration (10-40 sec) and low to medium peak amplitude ($2e-6$ – $8e-6$ m/s) giving characteristic spider plot shaped as a needle pointing toward the frequency. In Figure 21 all events have this characteristic shape, except one that has larger peak amplitude in Driest and Catzulecher. This deviation is explained by the great proximity (only 12 km from Catzulecher and Moosfluh and 14 km from Driest) of the event despite its low magnitude ($M_w=1.8$). The attenuation and greater distance to the event could explain the lower amplitude in Driest.

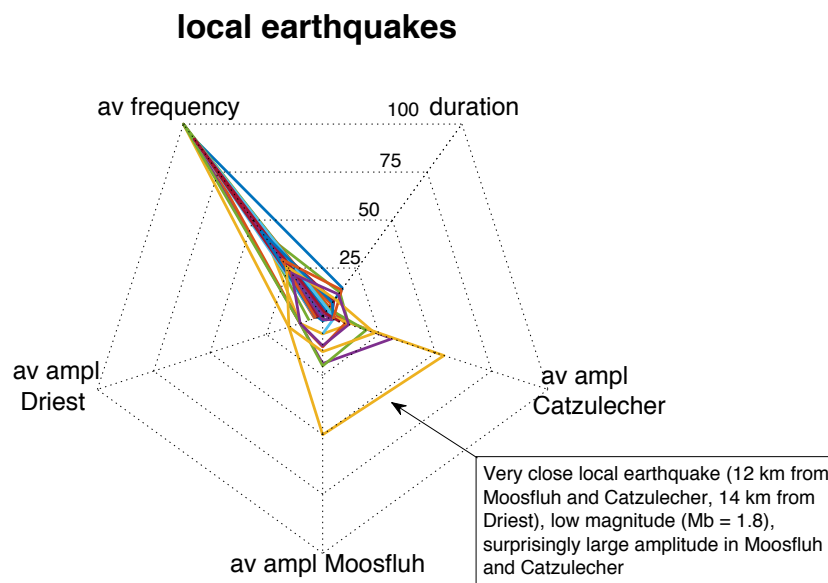


Figure 21: Spider plot for local earthquake

Figure 22 shows the same spider plot for events classified as teleseisms. They typically have low frequency (<2 Hz), long duration (50-250 sec) and low peak amplitude ($8e-7$ – $4e-6$ m/s) giving characteristic spider plot shaped as a needle pointing toward the duration. The magnitude is expected to be the same in all stations due to the large distance between the earthquakes and the monitoring network. Indeed Driest and Catzulecher have very similar peak amplitude. Nevertheless it was seen that the peak amplitude in Moosfluh is higher, due to the amplification of the cable car construction. Here again, one event (purple in Figure 22) does not follow the usual shape and has much larger peak amplitude. It was identified as a magnitude (M_w) 8.2 earthquake occurring in Mexico. The large magnitude (exponential scale) is the most probable cause of the large recorded peak amplitude.

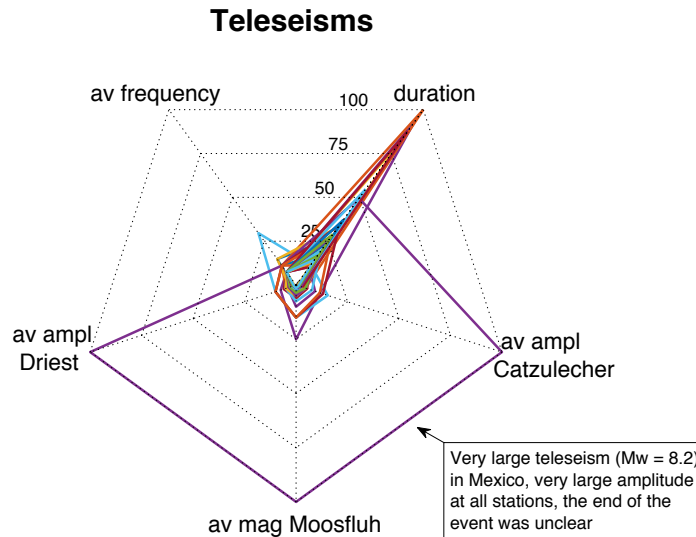


Figure 22: Spider plot for teleseisms

Figure 23 shows the spider plot for events classified as rockfalls. They are characterized by medium frequency (2-8 Hz), low duration (5-30 sec) and medium to large peak amplitude (9e-7 – 5e-6 m/s). The peak amplitude was expected and is varying at each station because rockfalls are local events located inside the seismic network. Driest station located on the other valley flank shows low peak amplitude due to great attenuation of the seismic waves during crossing of the glacier. Catzulecher is on the same side so that the peak amplitude is larger. Moosfluh is at about the same distance as Catzulecher also on the same side of the valley but the cable car infrastructure amplifies the vibration giving larger peak amplitude. All rockfalls plotted here have the same pattern on the spider plot, confirming that the signals classified as rockfalls not seen on the webcam were indeed rockfalls.

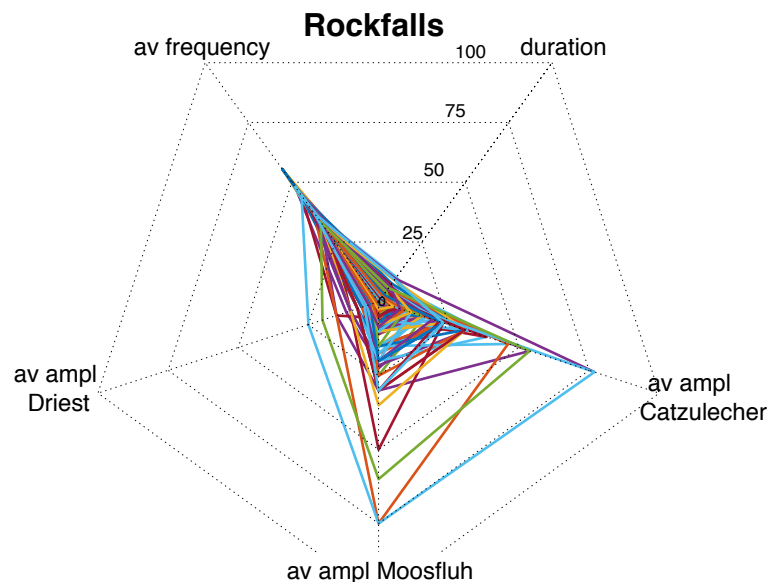


Figure 23: Spider plot for rockfalls

From these 3 spider plots it is obvious that we have 3 event types with distinct typical seismic parameters. From now on, a rockfall catalogue (only rockfalls) was built and all the next steps focus on rockfall characterization in the Moosfluh study area. The earthquakes were not further investigated.

5.3 Seismic data

All identified rockfalls entered in the catalogue will be further characterized by analyzing the seismic signal in a systematic routine. The files are 24 hours miniSEED files, which is a striped down version of the SEED format (standard for seismological time series) containing only waveform data. 24 hours files means unnecessarily long processing time and many unwanted signals. Therefore only the needed data was kept, which is each rockfall event with a minimum of 70 seconds before the start and about the same after the end of the event. To do that, the file is read by the readMSEEDfast Matlab function (Mityska, 2014) and the wanted time is cut from the 24 hours file (Figure 24 up). Then the processing steps are applied to the cut signals. A smoothing envelope is calculated (Figure 24 red line) to outline the peak of the event and remove outliers. The smooth function in Matlab was applied with the local regression (LOESS) smoothing method to give more weight to the nearest neighbors and the moving average was calculated with 1% of the data points. Then the peak amplitude, start time and end time were obtained from the cut and smoothed signal. The starting time of the event is manually picked as accurately and consistently as possible. The lowest point just before the first peak reaching above the noise level was chosen visually as event starting time. 70 seconds of noise before that starting point were then averaged and used as threshold to automatically close the event (Figure 24 down). After trying several average lengths, 70 seconds was giving event closure time when the noise level just reached back to the level it had before the start. Longer and shorter average gave miss-closure of the event in many cases, closing either too early (event still ongoing) for shorter averages or too late (noise level already back for several seconds) for longer averages. The duration was calculated by simple subtraction between the end and start time. The peak amplitude was directly extracted from the smoothed envelope automatically picking the largest amplitude value. This routine was applied to every rockfall event at each station where the event was detected (from manual identification). A pre-filtering was applied between 0.1 and 20 Hz, which is well below and above the typical rockfall central frequency (2 to 8 Hz). Additional filtering was done in exceptional cases when low signal to noise ratio prevented automatic closure without tight filtering.

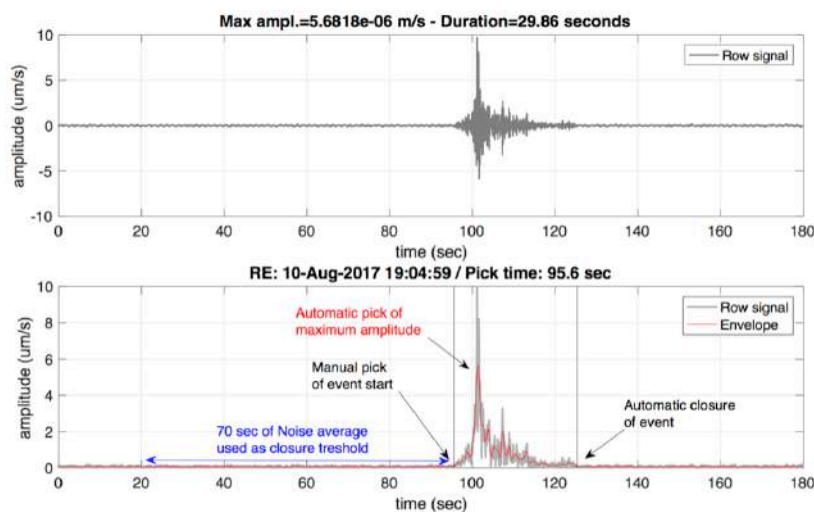


Figure 24: Calculation of the peak amplitude and event duration from the raw signal (event of the 10.8 at 19h06 UTC)

Even with a systematic routine, picking of the event start is sometimes problematic. Because of the characteristic gradual start of rockfall signals and varying signal to noise ratio, detecting the true start is not easy. For example, depending on the noise level the start can be “hidden” by the noise and chosen too late at one station while another station having lower noise does not show this problem. This can lead to relatively large differences in picking time between stations. Another problem was occurring in some cases during the event closure. Due to low noise level before and slightly larger noise after the event, the threshold was either never reached, or reached very late. Figure 25 gives an example of such cases. When it happened, the closing time was corrected manually to have better approximation of the duration.

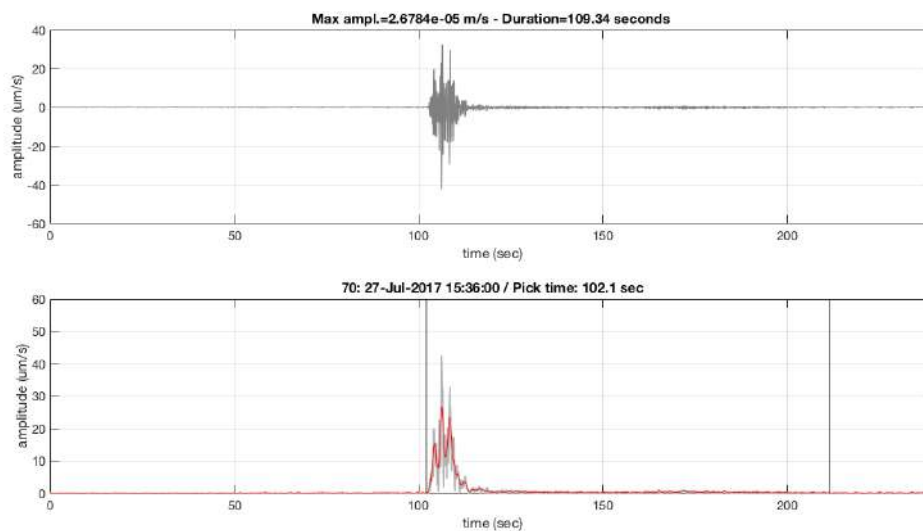


Figure 25: Rockfall having lower noise before than after the event leading to misidentification of the event end

Usual noise level varied between day and night and between the stations. At the cable car station, the noise was the largest, especially during the day due to the operation of the cable car. It typically ranged between $6.4\text{e-}6$ and $6.4\text{e-}5$ m/s during the day whereas it ranged between $2.1\text{e-}7$ and $2.1\text{e-}6$ during the night. In Catzulecher the noise level ranged between $1.1\text{e-}7$ and $1.1\text{e-}6$ m/s during the day whereas it ranged between $1.1\text{e-}7$ and $4.3\text{e-}7$ m/s during the night. In Driest the noise level was similar to Catzulecher ranging between $1.1\text{e-}7$ and $8.5\text{e-}7$ m/s during the day and between $1.1\text{e-}7$ and $2.1\text{e-}7$ m/s during the night. These noise differences between day and night makes it slightly easier and to identify events during the night and the seismic parameters can be quantified more accurately.

5.4 Optical data

Imagery is a way to confirm the seismic signal identified as rockfall in the field. Webcam photos combined with Leica vector measurements and georectification enabled accurate assessment of spatial rockfall properties. The events sources, deposits, runout distances and volumes could be first estimated from the webcam photos and then quantified with the Leica vector and the georectification. In this chapter the steps to obtain these parameters are explained.

5.4.1 Webcam

The webcam was mostly used to confirm the seismic signal corresponding to rockfalls and to obtain spatial information, which was crucial for the next steps. The webcam photos themselves were not sufficient to extract the 3D coordinates of the blocks or to measure lengths because pixels have different sizes in different parts of the photos (over 1000 meters between the slope bottom and top in the camera direction) so that it only gives relative location of the blocks.

5.4.2 Selected events for Leica vector and georectification measurements

20 events were selected for further investigation of their spatial properties. The only criterion was that they had to be identified in the webcam photos. Without that no location indication can be extracted. Then the source and deposit were identified on the webcam photos to be later measured with the Leica vector or the georectification technique. The field campaign for the Leica vector measurement took place on the 12th of October so that all 20 selected events took place before that (until the end of September because the seismic signal for October was not processed yet). Table 1 presents the selected events that were used for all further spatial analyses. They were mostly long duration events with large peak amplitude because small events were usually not detectable on the webcam photos. One event was identified on the webcam by chance but was not seen at any of the three seismic stations. The last one (29.09.2017) was well seen in Moosfluh but missing data at the other two stations prevented its identification there.

date	start time (UTC)	average duration	max amplitude	nb of station	short description
<i>dd.mmm</i>	<i>hh:mm:ss</i>	<i>(sec)</i>	<i>(m/s)</i>	<i>(max 3)</i>	
07.juil	22:41:21	13.35	3.83E-06	3	single block, 2 deposits
27.juil	15:37:43	14.72	1.76E-05	3	small rock avalanche
04.août	02:49:27	19.17	1.62E-06	3	single block, long runout
06.août	18:58:00			0	single block, roll in talus
07.août	18:37:25	9.38	6.42E-06	3	short, deposit just below source
08.août	07:11:18	19.80	6.02E-06	2	2 large blocks, short runout
10.août	12:39:20	39.50	1.16E-05	2	large single block, freefall, long runout
10.août	19:06:35	30.93	5.56E-06	3	large block split, various runouts
11.août	20:37:11	36.06	1.91E-06	3	several small blocks, various runout
14.août	17:58:40	53.95	3.01E-06	3	many blocks, long various runout
21.août	20:03:13	12.06	1.64E-06	3	1 block split in ++ small ones, various runout
22.août	03:57:12	29.70	2.49E-06	3	large single block, free fall
22.août	23:46:48	39.41	1.50E-06	3	large single block, 2 deposits
27.août	18:24:22	12.76	7.51E-06	3	large block, deposit just below source
04.sept	01:35:10	15.69	2.88E-06	3	free fall, short runout
11.sept	22:00:16	23.77	1.05E-05	3	several blocks, short runout
13.sept	17:51:47	24.73	3.44E-06	2	large block, free fall, short runout
19.sept	20:41:35	40.26	1.04E-05	3	2 large blocks, short runout
19.sept	23:37:55	47.23	5.20E-06	3	several blocks, very longrunout
29.sept	05:54:36	11.30	9.48E-6 (Moos)	1	large block, deposit just below source

Table 1: Main parameters of the selected events for measurements with the Leica vector and georectification

5.4.3 *Leica vector*

To obtain geographic location of blocks, the Leica vector was used in the field for the 20 selected events mentioned above. The relative locations of the rockfall sources and deposits were collected and redrawn on one clear webcam photo. In the field, each block source and deposit was located from the photo. The azimuth, inclination angle and distance between the measurement point (Driest) and the target were measured with the Leica vector giving the real 3D coordinates of each block source and deposit. The direct runout distance was approximated by subtraction (source coordinate – deposit coordinate). These parameters are important for the estimation of the energy involved.

5.4.4 *Georectification*

The high resolution of the photograph from Geoprævent allowed recognition of objects as small as 1 by 1 meter (1px \approx 20cm at a distance of 1.2km). Georectification was necessary to measure the wanted parameters on the photograph. After this step it was possible to locate rockfalls in the Swiss coordinate system (CH 1903 LV03) as well as measure distances and lengths on the photograph (runout and volume). The basic georectification tool in QGIS or ArcGIS cannot be used because the photograph is not aerial looking straight downward. It is an oblique photograph, which means that very large distortions develop when using basic georectification tools. Therefore another tool was used: the Matlab routine PRACTISE (Härer et al., 2015). The main goal of this routine is automatic snow classification of webcam photographs. One of the necessary steps in the routine is the link between each photograph pixel to a real world coordinate (the SwissALTI3D DEM here). This is exactly what we need as georectification. In the code, two configurations are available and only the first one (configuration A) was used. Required inputs are a photograph, a DEM, ground control points (GCPs) and camera parameters (can be calibrated with trial and error if not available). The photo used here is the one from Geoprævent because of its very high resolution. It allowed better identification of GCPs, more accurate georectification and easier identification of the rockfalls (details seen even with large zoom in). The DEM must be in ASCII format. The GCPs is a text file containing real world and the corresponding pixel coordinates of each ground control point (10 GCPs here). They were marked in QGIS using the basic georeferencing tool with the swissALTI3D DEM, the SWISSIMAGE25 orthophoto (to better recognize topographic features) and the Geoprævent photo. Only points outside the fast moving part of the DSGSD were chosen as GCPs to avoid large errors. The Camera parameters were entered in the PRACTISE input file for the first fit of the photograph on the DEM. The needed parameters were the focal length, the sensor length, the sensor width and the camera location (XYZ in the correct coordinate system). Figure 26 shows the fit of the GCPs calculated with the PRACTISE routine. The green crosses are the initial guess of the GCPs on the photograph based on the given camera parameters, the little red dots are the GCPs located in the DEM, and the red circles are their corrected location on the photograph. The code is now ready to run.

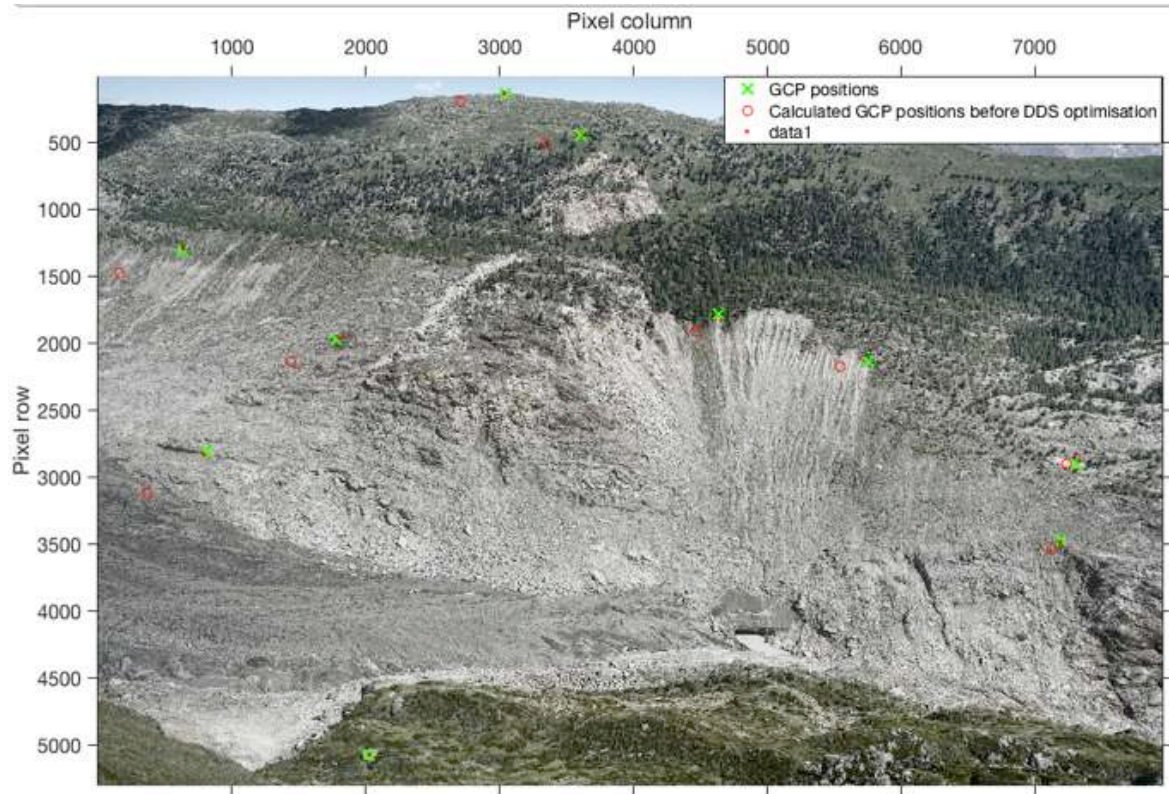


Figure 26: GCPs matching between the high-resolution photograph and the DEM

The output is a georectified photo with snow classification (Appendix 4) where each dot is a DEM coordinate linked to the corresponding photograph pixel. Figure 27 shows the output file in a map view. The grid has a final sampling resolution of 2 meters (limited by the DEM resolution) except for some holes due to occlusion. The most important source of error is the changes in topography between summer 2016 (DEM) and July 2017 (Geprevent photo). The rockfall area moved up to 70 meters at some at the main Scarp leading to large errors. Nevertheless, the blocks themselves didn't undergo differential displacement so that the effect of these changes is not relevant when calculating block volumes. Moreover the fast moving part of the DSGSD had differential displacement of several meters only mostly concentrated at the boundaries, while central part mostly moved as one single body. Since all rockfalls sources and deposits were located under the scarp (Figure 27), the runout uncertainty is as well of several meters (and not tens of meters).

Map view of the georectified photo with PRACTISE

Each dot correspond to one dot in the photos. They are 2 meters appart (dem resolution)

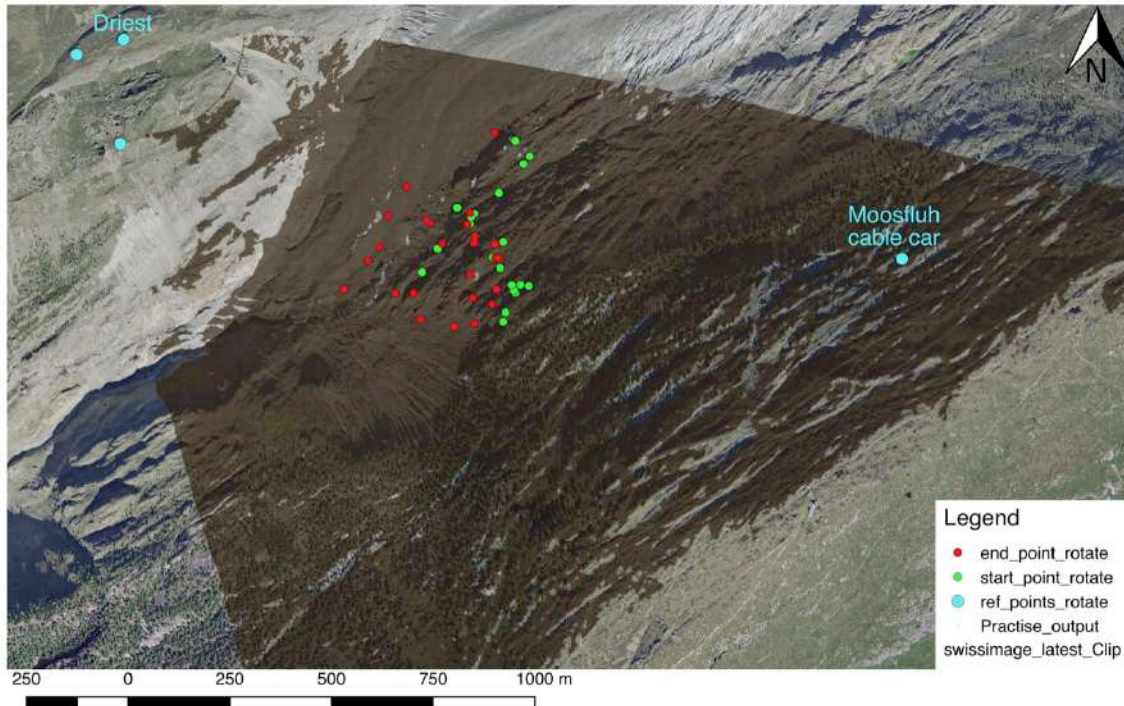


Figure 27: map view of the photo georectification. Each black dot is one DEM coordinated linked to one photo pixel.

5.4.5 Block volume estimation

It is possible to estimate block volumes for the 20 selected events with the help of the webcam photos and the georectified photograph. From the seismic data, the timing of rockfall is known and many events could be identified on the webcam. The block source and deposits was located on the webcam photos and then on the georectified photo. On that photo the 3D coordinates from the source and deposit was extracted. Moreover, thanks to the good resolution of the photograph, it was possible to measure the blocks dimensions. Since the photograph was taken on July 3rd, all fallen blocks since that date are still at their source in the photograph. Dots the closest to the block's corners were identified and the dimension was calculated by subtraction of the coordinates. Only 2 dimensions of the blocks could be quantified and the third was assumed to be in between the 2 measured sides. As an example, one of the identified blocks is shown in Figure 28. This block fell down the 27.7.2017 at 15h37 (UTC). Its source was measured with the Leica vector and on the georectified photo. By measuring the coordinates, the dimensions were calculated and gave a volume of $18 * 14 * 16 \text{ m} = 4'032 \text{ m}^3$, which is the largest block observed. Measured volumes ranged from 216 m^3 to $4'032 \text{ m}^3$ with a mean of $1'456 \text{ m}^3$. Most blocks have rectangular shapes and some are near cubic.

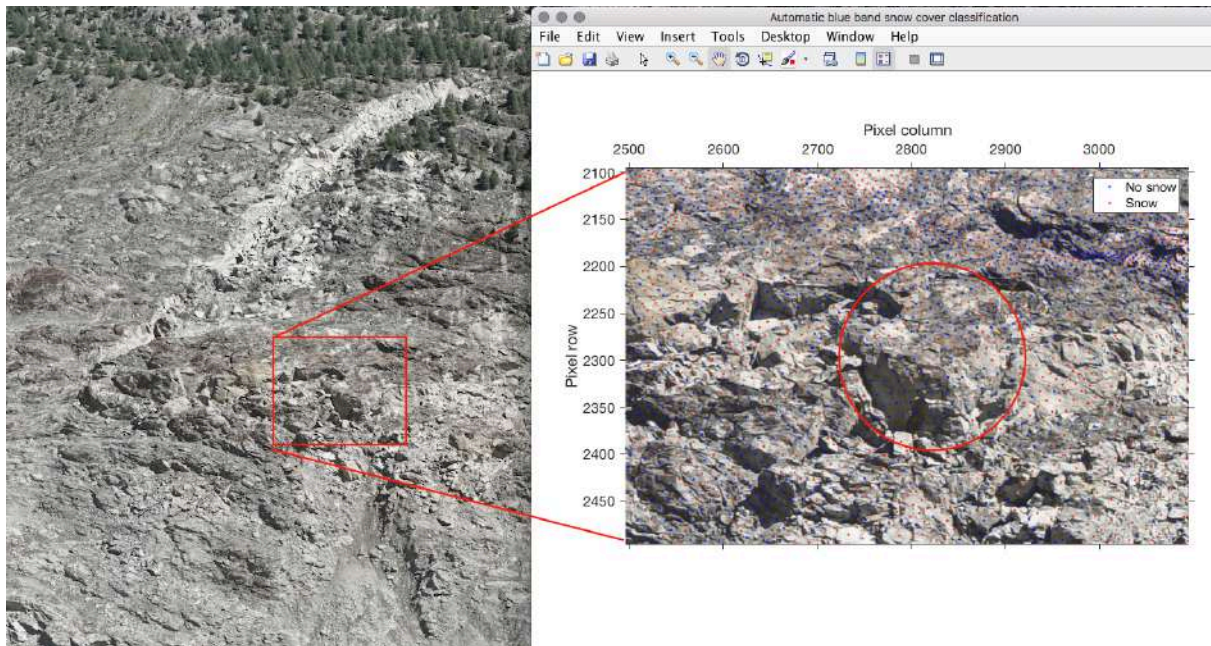


Figure 28: Example of block volume measurement from the georectified photo

5.5 Data combination

All the derived parameters can be now used together, having for goal the creation of a magnitude frequency plot for the rockfall phenomena in Moosfluh.

5.5.1 Energy calculation

We used numerical simulations to estimate the kinetic energy of rockfalls by using as reference the source and deposit of the 20 selected events measured with the Leica vector and the georectified photo. The energy is an important parameter to characterize rockfalls, since it is considered when defining rockfall hazards (hazard maps). It is also needed in the design of mitigation measures during calculation of the needed rock net strength. The program RockyFor3D was selected to simulate the rockfall events. 10 raster input files are required to run the model and are described in Appendix 5. The main ones are a DEM, the block volumes and the event source area. In addition to these: soil, slope and block (shape, density) parameters are needed. All these parameters were estimated from available seismic and optical data and calibrated by forward modeling trying to fit the modeled rockfall deposit with the one measured in the field. In this case, the model was run without any forest or rockfall nets, which are indeed not present in the area of study. 200 simulation per cells were made (about 1000 per block source), a free-fall height of 0.5 meters was needed to give the initial energy for the blocks to fall and the block volume was varied in a range of $\pm 5\%$ of the given values.

The rockfall source areas were defined and characterized (Figure 29). To constrain the model to the blocks observed and not the entire slope, the source area was taken as the location of the block sources from the georectification measurement. The rest of the slope was considered not to be a source of rockfall. The estimated volume for each block from the georectification was used as input for the block dimensions. The DEM used was the SwissALTI3D DEM from 2016 (Swisstopo, 2016)

already used for the georectification. The rock density was estimated to 2700 kg/m^3 from literature values (Kelly et al., (2004) and Grämiger et al., (2017)). The blocks were assumed to have cuboid shapes (non spherical) from photograph observations. The slope was divided into 3 soil types (Figure 29): the first one is the glacier used as stopping area (white), the second one is the bedrock covering the largest part of the study area (orange) and the last one is the talus slope, composed mainly of rockfall deposit (purple). Due to the large fractures and blocks on the ground, the chosen roughness values for the bedrock were 0.7m (rg70), 3m (rg20) and 6m (rg10) and the ones for the talus slope were 0.5m (rg70), 1m (rg20) and 4m (rg10). Input parameters for each zone and each rockfall source are listed in Appendix 6.

Classification input for RockyFor3D

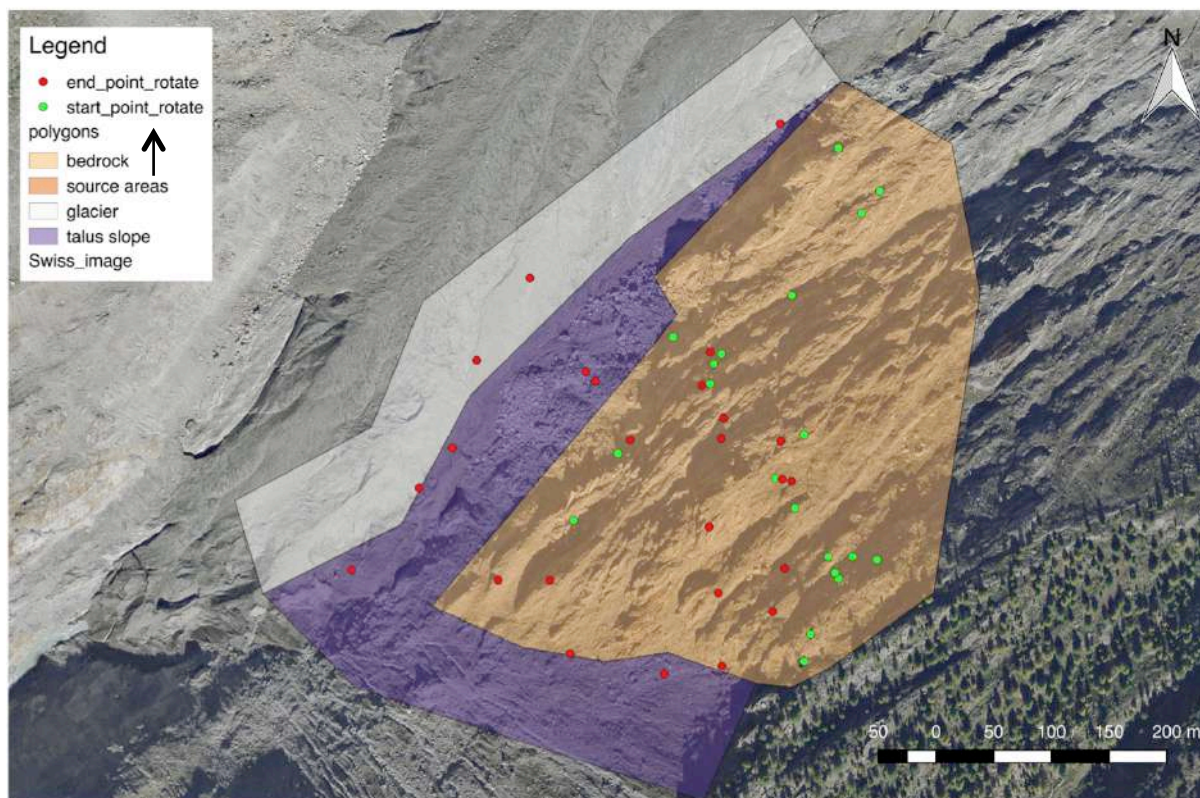


Figure 29: Soil classification for RockyFor3D

The output files of the model are described in Appendix 7. The main output used was the kinematic energy being the target parameter. Moreover, the deposit location of modeled rockfall events was used for comparison with the Leica vector and georectification measurements. The travel time of each event was compared to the duration of the seismic signal. Appendix 8 lists the output values for the 20 modeled rockfall events in comparison with their measured values (trajectory time VS duration, peak amplitude, kinetic energy).

This model gives us an estimation of the kinematic energy for the 20 selected rockfalls but was needed for the entire rockfall catalogue. Therefore the energy was correlated with both the peak amplitude and the event duration to extend the estimation to the entire catalogue. The best results were obtained for the event duration (Figure 30) giving an R square value of 0.75 for a power law fit

against 0.08 (linear fit) for the best fit with the peak amplitude. The peak amplitude is dependent on both the volume and the velocity of the block scaling the chock energy when hitting the slope but the kinetic energy is mostly driven by the velocity ($E_{kin} = 1/2mv^2$). Moreover the topography is highly irregular (large counter scarps, steep slopes and flatter areas), so that the peak amplitude poorly correlates to the kinetic energy. On the other hand, the duration is mostly linked to the distance travelled by the blocks and their velocity along the path. Therefore the duration correlates better with the kinetic energy also mostly driven by the velocity. Figure 30 displays the correlation obtained from the curve-fitting tool in Matlab between the average duration and the energy estimated with RockyFor3D. The best fit was a power law given by the following equation:

$$E = 5670 * d^{1.29}$$

where **E** is the energy in kilo-joules and **d** is the event duration in seconds.

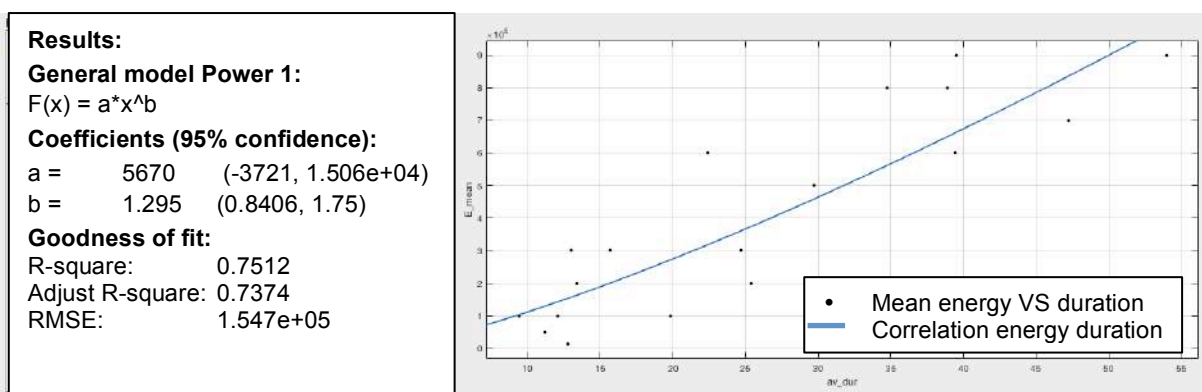


Figure 30: Correlation between the duration and the energy to estimate the energy of the entire rockfall catalogue

5.5.2 Magnitude frequency plot

It has been widely shown that power laws describe well the frequency of rockfalls occurrence with their magnitude (Biagi et al., 2017, Corominas et al., 2017, Williams et al., 2018). Such Magnitude frequency plots are important for hazard assessment and risk mitigation. The plots characteristics are linear slopes in a log-log scale allowing extrapolation of the volume and frequencies to events larger than the ones recorded. In that sense magnitude frequency plots can predict the type, size and return period of rockfalls in a given region. Nevertheless, a threshold has to be set corresponding to the largest possible event, which is mostly defined by the joint sets orientation and spacing. The relation is given by the equation:

$$n(v \geq V) = aV - b$$

where **n** is the frequency of block having volumes larger than **V**, **a** is an annual frequency of occurrence for blocks larger than 1m³, and **b** represent the slope of the line. Both **a** and **b** varies depending on the geological and geotechnical properties (Biagi et al., 2017).

Most rockfall prone areas have safety factor close to 1 and only need small disturbances to trigger rockfalls. The already highly damaged over-steepened rock slope in Moosfluh is no exception. Nevertheless in comparison to other rockfall prone areas, the activity in Moosfluh is extremely large. The main reason is the presence of an accelerated DSGSD amplifying the damages of the rock mass

and acting as increasingly stronger predisposing factor (exponential acceleration since 2005). Through this process, common rockfalls triggers such as heavy rainfall, snowmelt and large earthquakes become extremely efficient. These trigger mechanisms have minimum intensity thresholds usually reached only few times per year (0 - 5) but In Moosfluh the quasi non-stop displacement of the DSGSD lowers that threshold increasing the triggering frequency. The result is a rockfall catalogue of 250 events in 4 months while it can take hundreds of years to have that many events in usual conditions. Corominas et al. (2017) lists 11 magnitude frequency studies of rockfalls having catalogues counting 27 to 3096 events, most of them ranging between 200 and 400 events and in some cases, models simulating rockfalls were developed to have enough events. The 250 events identified in Moosfluh are in that sense largely in the average.

Characteristic magnitude frequency plots display the rockfall volume on the x-axis and the cumulative frequency on the y-axis in log-log scale. Here the cumulative frequency is directly extracted from the rockfall catalogue using a histogram to build categories. For the magnitude, instead of the block volume, the energy is displayed. The choice was made because the energy could be modeled (RockyFor3D) or calculated (correlation energy-duration) for the entire rockfall catalogue. It was not the case for the volume only calculated for 20 events (no good correlation with seismic parameters). Another advantage of the energy over the volume is that it can be directly used to scale mitigation measures such as rockfall nets.

6 RESULTS AND INTERPRETATION

First the rockfall catalogue, classification the spatial and temporal distribution, energy calculation, and magnitude frequency plot are described in a first step and interpreted in a second step in this chapter. Finally uncertainties in the main data, extracted and calculated parameters are estimated and discussed.

6.1 Rockfall Catalogue

The rockfall catalogue is the main direct output and the basis for all further analyses. It resulted in the identification of 250 earthquakes, 32 teleseisms and 18 local earthquakes. Note that not all visible earthquakes were described during this work because the main focus was set on rockfall events. All earthquakes reported here were confirmed in one of the 2 earthquake catalogues used (SED (seismo.ethz.ch) and USGS (earthquake.usgs.gov) catalogues). The catalogues list around 10 to 30 earthquakes per day having magnitude larger than 4.5 in the USGS catalogue and 1 to 10 earthquakes per day ($M_w > -0.6$) in the SED catalogue. Most of these earthquakes were not detected in our seismic network, since they are too weak and/or too far. Out of the 250 rockfalls observed in the seismic signal, only 22% were confirmed on the webcam photos. Confirmed means that either the event has been identified on the webcam within the 10 minutes (elapsed time between 2 photos), or it was no other events occurred during the time between the first and second photos used for identification in case of longer temporal baseline. Additionally 8-16% of events were seen on the webcam but could not be linked doubtlessly to a given rockfall signal because several events occurred

within the time the 2 photos used for identification were taken. Longer baselines are a result of either darkness or bad weather, both phenomena generating several hours (up to days when combined) without any usable photo. It also happened that rockfalls were identified on a webcam photo but were not detected by the seismic network, which is an important limitation to be aware of. For example, during the night between the 5th and 6th of August, 5 events were identified on the webcam overnight but none were identified in the seismic signal. That night was characterized by relatively large noises during parts of the night. It was mostly rainfall in Catzulecher and Driest and at the cable car, the installation was the main source of noise. Indeed sometimes, during the night noises of unknown origin were recorded. They are a set of 2 to 5 noises of given frequency, are constant over time but vary in intensity (Appendix 9). That night, the noises were ranging from usual values ($1e-7$ to $2.2e-7$ m/s) up to $6.4e-6$ m/s in Catzulecher, $3.2e-6$ m/s in Driest (during rainfall) and $2.1e-6$ m/s at the cable car. The hypothesis is that the rain signal superimposed to the rockfall signal preventing identification of several rockfall events. Probably other similar cases took place during the study period but were not detected because not all webcam photos were studied.

Figure 31 focuses on the seismic parameters of the identified rockfalls, namely the event starting time, the duration, the mean frequency and the peak amplitude. These parameters are displayed as boxplots showing the median, the 25th and 75th percentile, as well as outliers. The average event starting time is 12h15, which means that rockfalls are symmetrically distributed during the day around that time. The mean duration is 16 seconds and is very similar at all stations. The duration varies of 3.1 seconds (standard deviation) in average between the three stations. It is a good result and means that the technique used for picking the starting and closing time was adequate. The mean frequency is very constant over the entire rockfall catalogue with a mean of 4.7Hz and a standard deviation of 0.8Hz meaning that it is a very good variable to discriminate rockfalls from other event types on seismograms. The peak amplitude varies between the stations due to differences in the medium crossed by the seismic waves. Driest is below average, the Cable car is above average and Catzulecher corresponds well to it. The minimum peak amplitude is about $1e-7$ m/s in Catzulecher and Driest indicating the sensitivity limit of the raspberry shake seismometers. That value fits the threshold of $1.4e-7$ m/s (between 1 and 20Hz) given in the technical specification of the sensor suggesting favorable noise conditions in Moosfluh despite the installation of the sensors at the surface and not underground as usually suggested as a mean to decrease the noise level. Catzulecher is the best station to identify rockfalls, having low noise and large peak amplitude for rockfalls. The reasons are that it is the closest station, it is located on the same slope as the rockfalls and it lies at a similar altitude (± 50 m) on bedrock. 98% of the events were identified there. The low percentage of event seen at the cable car (61.2%) despite the amplification of the signal is due to operation of the cable car facility from 8h to 16h30 every day (local time; UTC+2). Despite low noise level, low signal amplitude allowed the detection of only 88% of the events in Driest. At that station signal attenuation and scattering while crossing the valley and the glacier is the main reason for lower signal to noise ratio leading to detection of less events. It shows the importance of having low noise and no attenuation to detect a maximum of events.

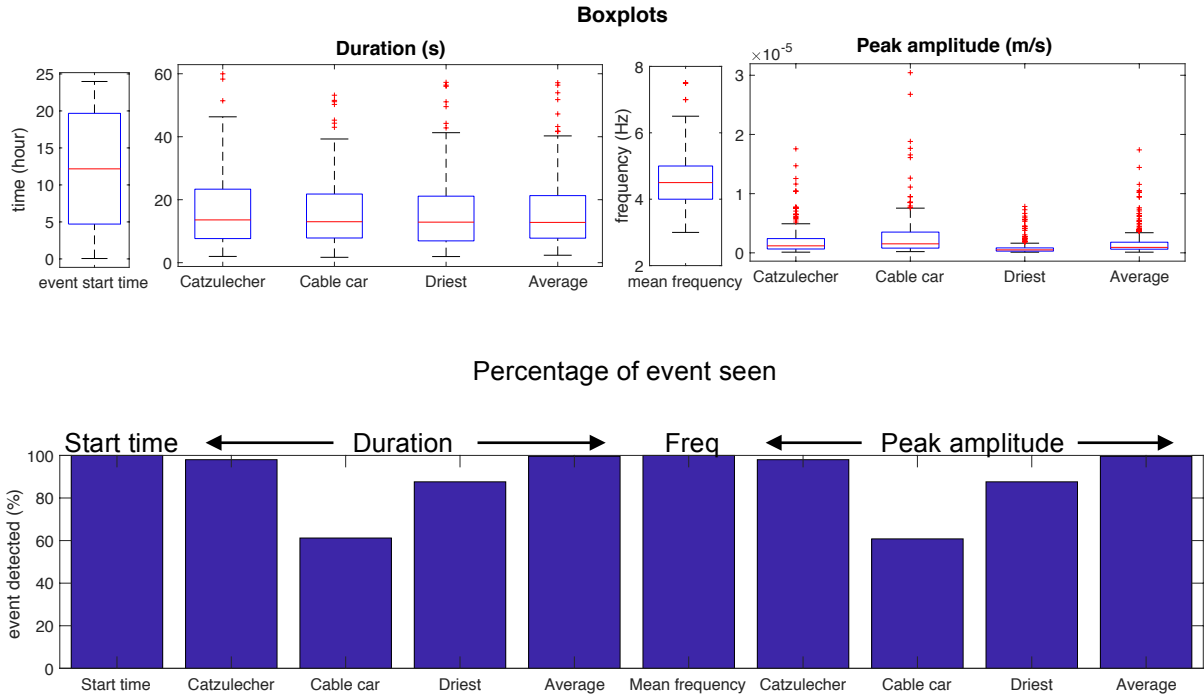


Figure 31: Summary of the main seismic parameters of the rockfall catalogue as boxplot. The red line represents the median and the blue ledges indicates the 25th and 75th percentile. The red + are considered as outliers (top) and a bar plot showing the percentage of rockfall detected for each parameter at each station (bottom)

Figure 32 shows the peak amplitude as a time-series for the 3 stations and note it only displays the largest amplitude event per day. High amplitude events have high amplitude at all stations, and the same is true for low amplitude events. Concerning the time-series, more events have larger amplitude in Mid August, end of September and end of October, periods also corresponding to increase in rockfall activity. In more quiet periods, rockfalls have lower amplitudes.

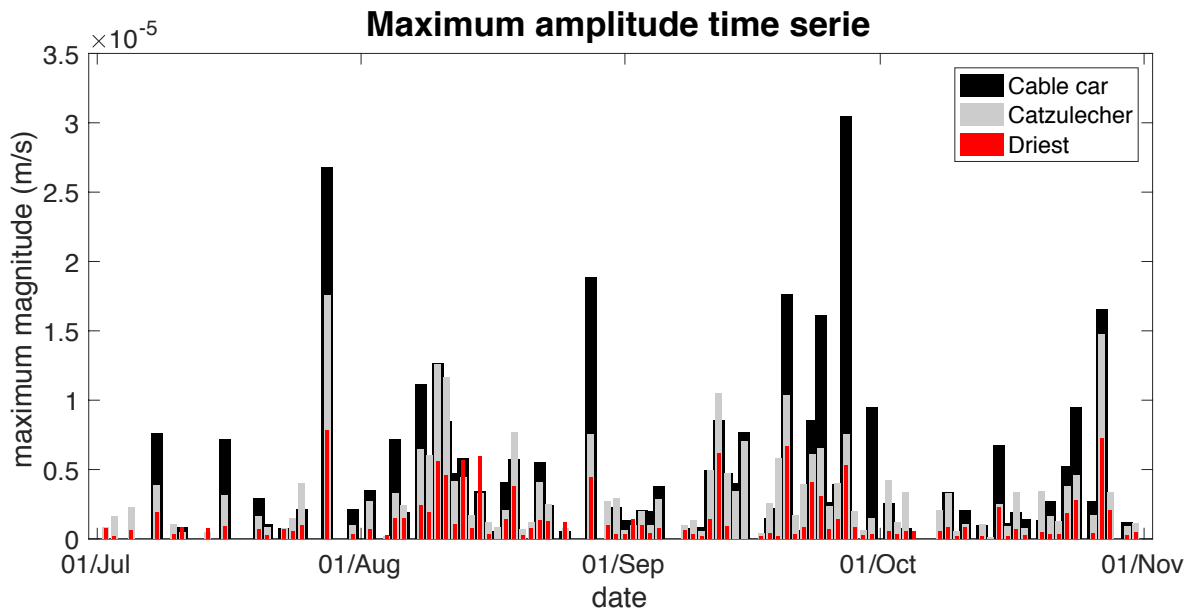


Figure 32: Time-series of amplitude (only the largest amplitude event of each day is shown)

6.2 Rockfall classification

Based on the signal characteristics, rockfall events were sorted into 7 categories: a) short, b) large start, c) gradual start, d) double peak, e) constant amplitude, f) low amplitude and g) single large peak. The categories are presented in Figure 34 with a short description of the characteristic signal for each of them. The choice of categories was based on the spider plots and distinct characteristics of the raw seismic signal. Some of them, for example the double peak and the constant amplitude categories could not be differentiated only by looking at the spider plot. The entire seismic signal was needed to see these specific features because the peak amplitude and duration don't give enough indication to see two peaks during an event or a constant signal for example. More investigations could be undertaken to find new seismic parameters being able to discriminate such signals, for example the amplitude ratio could highlight constant signals (Amp max/Amp mean) (Hibert et al., 2014). Figure 33 shows the number of events in each of the defined categories. Most events are concentrated into 3 of them: short (below ~10sec) gradual start and large start.

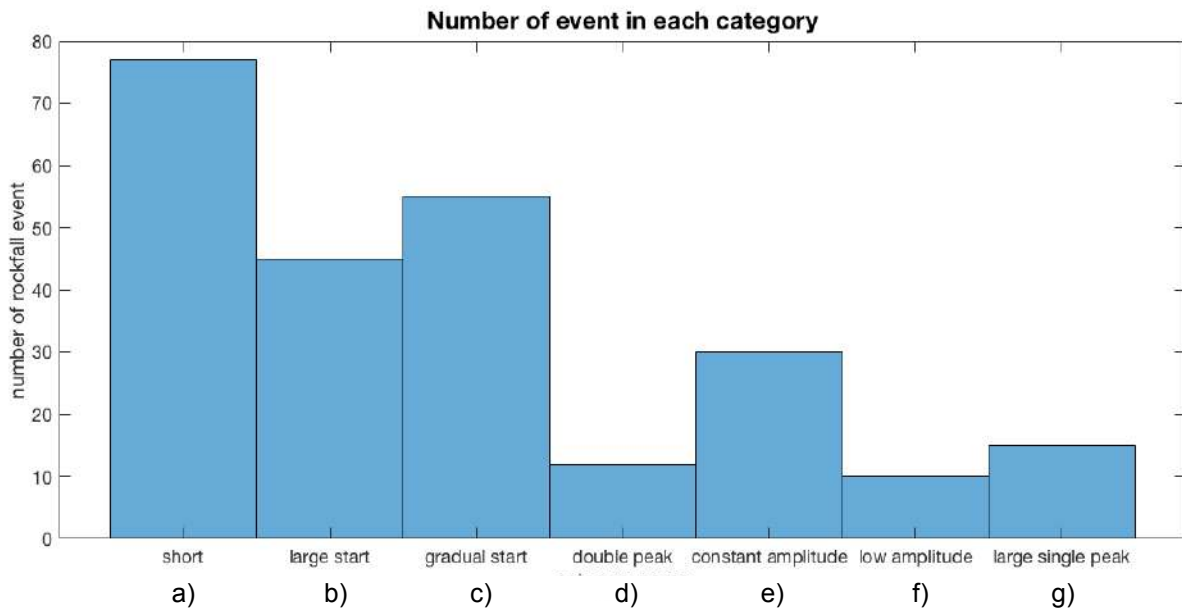
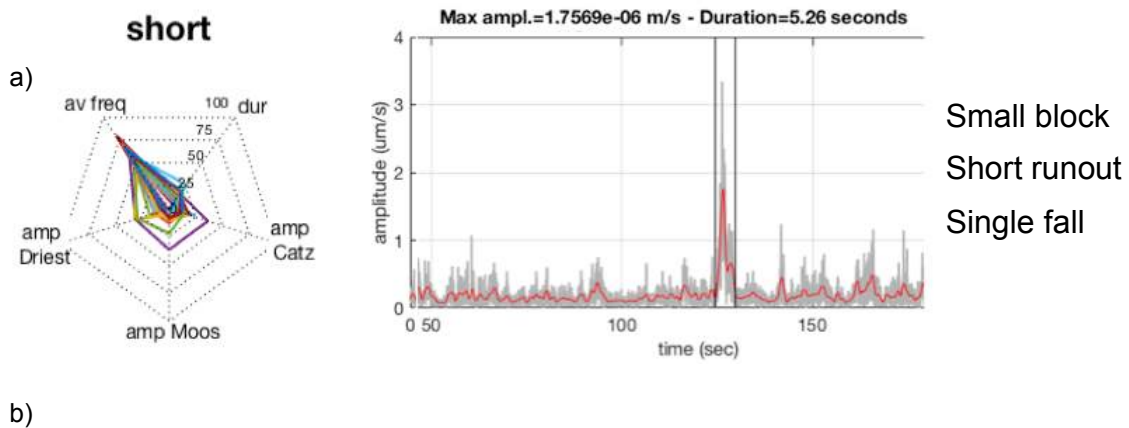
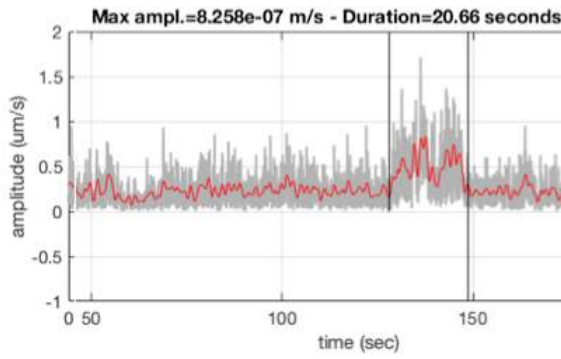
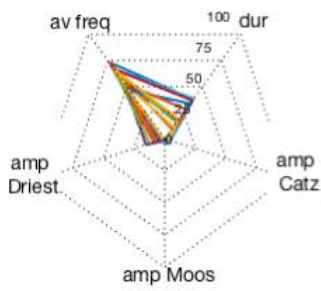


Figure 33: Number of event in each rockfall category

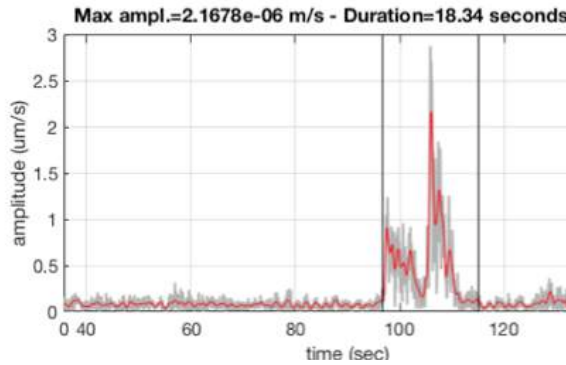
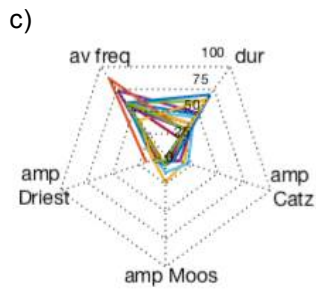


low amplitude



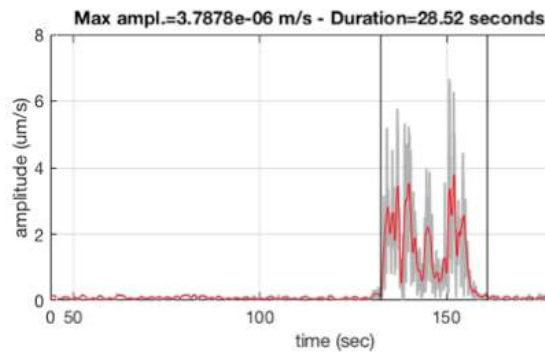
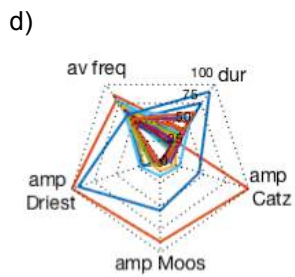
Small block
Not seen on camera

double peak



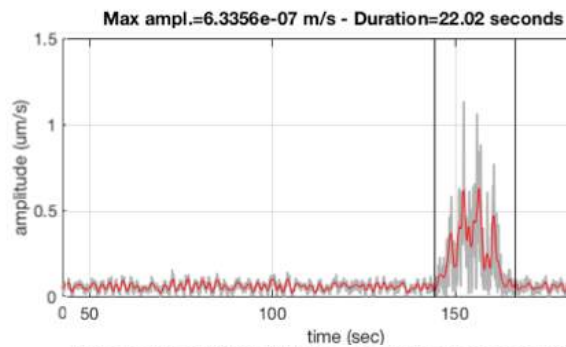
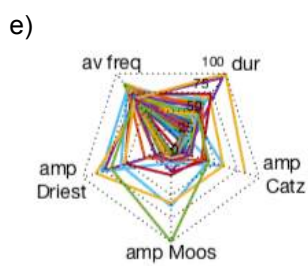
2 single blocks
Double chock

constant amplitude



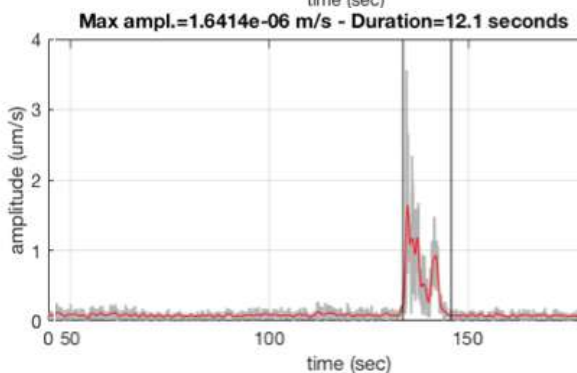
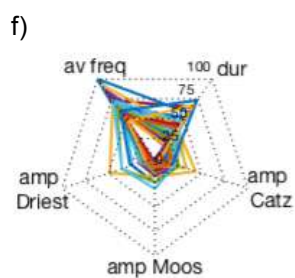
Long runout
Small rock
avalanche (small
or large blocks)

gradual start



Several blocks
Various runouts
Rolling on slope

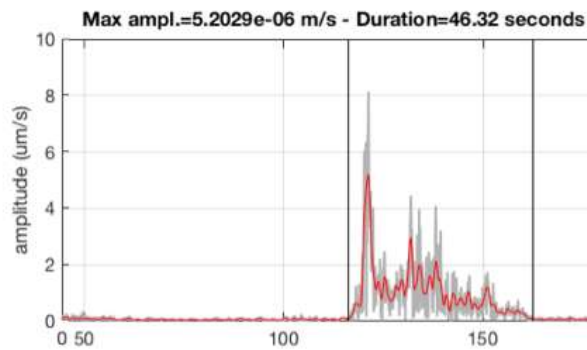
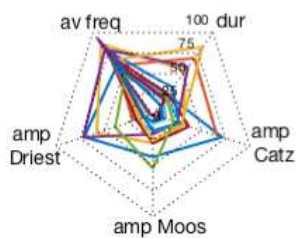
large start



Free fall
Large first chock

large narrow peak

g)



Free fall followed by
Long runout (rolling)

Figure 34: Spider plot and corresponding seismic signal for the 7 rockfall categories

Interpretation

Short events (a) are defined by short duration lasting between 2 and 10 seconds. They are the most frequent events in Moosfluh and are not necessarily the ones with the lowest amplitudes.

Low amplitude events (b) are rarely recorded because they are characterized by low peak amplitude meaning very low signal to noise ratio, which makes them hard to identify. Several additional low amplitude events occurred but couldn't be seen at more than one station (mostly Catzulecher) and thus were not listed in the catalogue. Moreover smaller events also occurred that could be heard during field campaigns but neither seen in the field nor on the seismic signal.

Double peak events (c) have low amplitude and long duration. The 2 peaks correspond to two parts having larger amplitudes due to 2 separate phases (2 drops for example) during the rockfall event. It could also be the generation of two rockfalls very close (in time) to each other, for example the first one generating the second during its fall. It has relatively long duration since it has 2 phases of energy increases (implies longer runout) or is 2 events in one.

Constant amplitude events (d) have relatively long duration and various amplitudes. No clear pattern was to be seen. The reason of constant signals is a continuous rolling and bumping of the falling rock mass on slope of relatively constant steepness and homogenous roughness.

Gradual start events (e) are the most typical rockfalls signals widely described in the literature. The block detaches, rolls and gradually gains kinetic energy and/or drags more material leading to gradually larger signal amplitude. The end is typically gradually decreasing where the opposite happens. Blocks slowly loose energy during chocks while rolling and bumping on flatter slopes and/or are broken into pieces stopping after different distances. They can have any duration and amplitude but all largest amplitude events observed here show this typical gradual start.

Large start events (f) are characterized by low amplitude and medium duration. Here most of the energy is lost after the first impact giving an asymmetrical shape of the signal with large start and gradually lower amplitude as it loses energy in the same way as explained for category e).

Large narrow peak events (g) have relatively low amplitudes except one large peak that is not in the beginning. They have either long or short duration and medium amplitude. The peak represents a

large loss of energy during impact after a relatively large gain of energy that could be due to a kink in the slope leading to free-fall and velocity increase.

6.3 Spatial and temporal distribution

Understanding rockfall distribution is necessary in order to understand the kinematics of the slope instability. Temporal distribution helps identifying the main factors contributing to rockfall causes and triggers. Spatial distribution helps understanding the displacement dynamic of the slope and the region of lowest stability and concentrated activity.

6.3.1 *Spatial distribution*

First of all, from the webcam photos, it was possible to see long-term changes in the fast moving part of the Moosfluh DSGSD. When taking one photo in July and one in October, the boundary and motion of the fast-moving body appear clearly. Figure 35 displays the different landslide features observed with that method. In red, a large flank scarp can be recognized as the eastern boundary. That large cliff become smaller in the middle slope and eventually stops. Nevertheless the evolution of the scarp shows a downward spreading and will eventually reach the slope toe in the future. For now, under the flank scarp (yellow) differential displacement spread across a 70 meters wide area being less intense on the external part of the boundary (northeast). The southwestern flank is showing similar behavior. The lower part is characterized by the same zone or differential displacement without having a clear flank scarp. The upper part is made of talus slope, which barely moves together with the rest of the body. Therefore the limit in that area is poorly defined. The head scarp (orange) is less obvious than the northeastern flank scarp but the displacement is concentrated on a single line currently developing the scarp into a cliff similar to the northeastern flank scarp. Rockfall deposit can be observed on the entire slope but 2 talus slopes (blue polygons and green rectangle) concentrate the largest rockfall deposits. The rest of the body within the scarp is moving down as a whole with slightly larger displacement closer to the scarp and smaller at the slope toe. The pink polygon shows a smaller part outside the main fast moving part also undergoing visible downward displacement during this time period (July-October 2017).

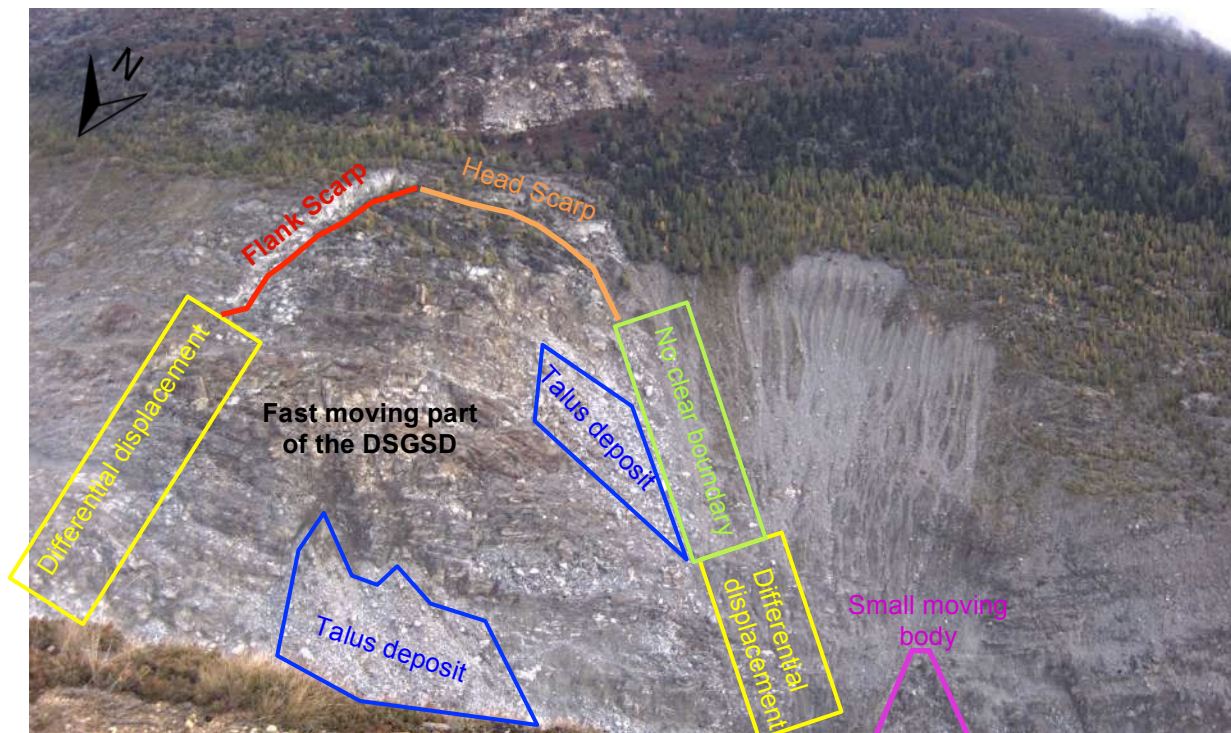


Figure 35: Main features of the DSGSD fast moving part

The spatial distribution at the rockfall scale can now be described. The source and deposit coordinates of the 20 selected rockfalls were measured with the Leica vector and georectification. Additional events, in particular occurring after the field measurements could be located on the georectified photo. Figure 36 shows the georectification of the selected events with the source coordinates in green, the deposit coordinates in red and direct runout in yellow lines. The georectification results were chosen here because the block identification was easier on the high quality photograph (large zoom possible) than in the field, leading to more accurate location of the events. The results with the Leica vector can be found in Appendix 10. Both methods were compared and the difference quantified. 4 outliers corresponding to clearly misidentified block source or deposit in one of the method were removed. The coordinates of block sources differed of 30 meters in average. For the same events, the coordinates of the block deposits differed of 75 meters in average. This larger difference is due to the more difficult identification of the deposit, due to deposit located out of the webcam frame or disintegrated block resulting in deposits at several locations. The runout distance differed of 30 meters between the two methods.

Interpretation

As mentioned in chapter 4.2.2 the orthophoto is from summer 2016. Therefore on Figure 36 many blocks seem to have reached the glacier and rolled on it. It is due to the fact that the glacier has melted between 2016 and 2017 leaving the studied slope mostly free of ice at the time of the field measurements in summer 2017, while the orthophoto still shows ice. All target deposit measured with the Leica vector and georectification were lying outside the glacier, 3 of them at its boarder.

Most rockfalls occurred on the southeastern (right of the blue line) section of the study area (Figure 36). They were concentrated in the upper portion of the slope and had long to medium runout. In that

section, most rockfalls occurred in August and September 2017. In the northwestern (left of the blue line) part of the study area (Figure 36) less rockfalls occurred. They took place on the lower portion of the slope and had medium to short runout. They mostly occurred in July and August 2017. These observations may indicate larger displacement during August and September on the upper section of the fast moving part where most rockfalls occurred. Indeed it is the location the closest to the scarps, and the one showing the largest displacement rate (Manconi et al., 2018a (GPRI on the 28.09.2017)).

Location from the georeferenced photo from Geopreavent

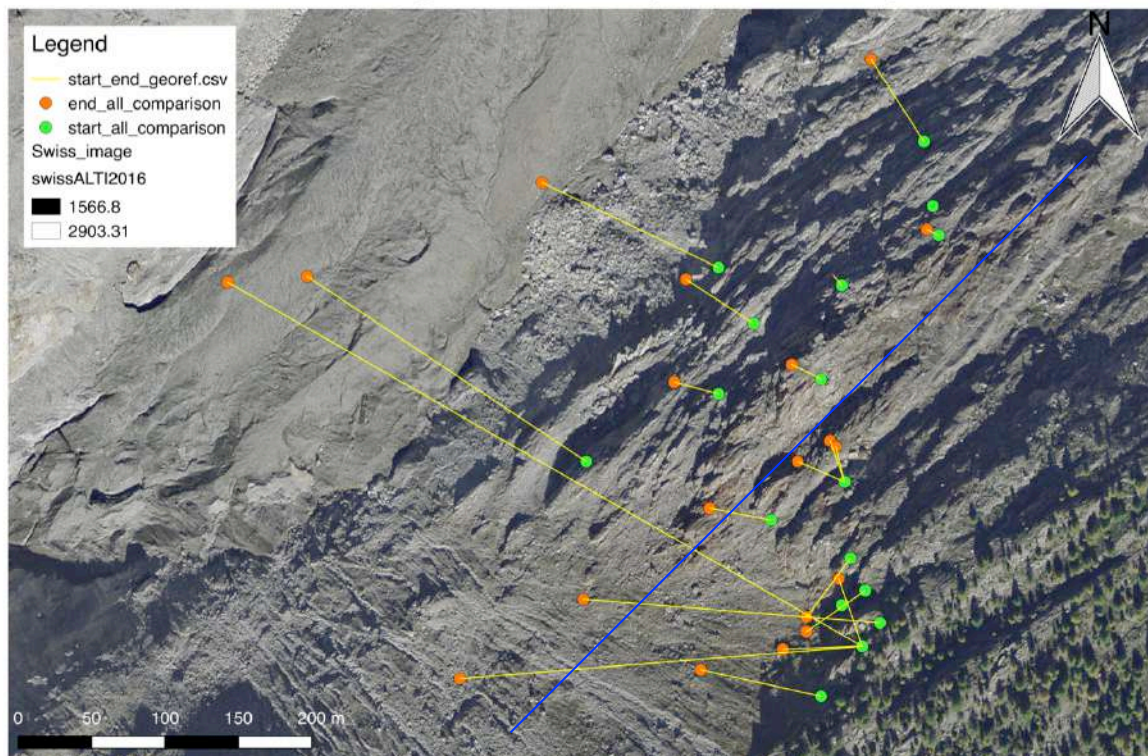


Figure 36: Source and deposit of the 20 selected events measured by the Leica vector

6.3.2 Temporal distribution

Figure 37A) shows a time-series containing the 250 identified rockfall events. The blue line depicts the cumulative number of events between July 1st and October 31st. The black dots are events identified on webcam photos and linked to a specific rockfall signal in the seismic data. This plot reveals a low and constant rockfall activity in July and in the beginning of August. In mid August the number of rockfalls suddenly increased counting 35 rockfalls within 3 days (10th, 11th and 12th of August) representing 14% of all identified rockfalls. Later the rockfall activity stayed constant until the end of the study period (31st October) but larger than the one in July before the increase. Figure 37B) shows the displacement data of reflector 72 (Figure 2) during the same time period (July 1st to October 31st). It is located just above the head scarp of the fast moving part of the DSGSD. Acceleration is observed from the end of August to the beginning of September and is corresponding to the increase in rockfall activity with a shift of 3 weeks. The causes of this time lag between both accelerations will be further investigated. It is an interesting observation, since at first; a behavior opposite to the one observed was expected. Increase in displacement of the DSGSD was expected to lead to an increase in the

number of rockfalls while here the increase in rockfall activity preceded the increase in displacement rate of the DSGSD.

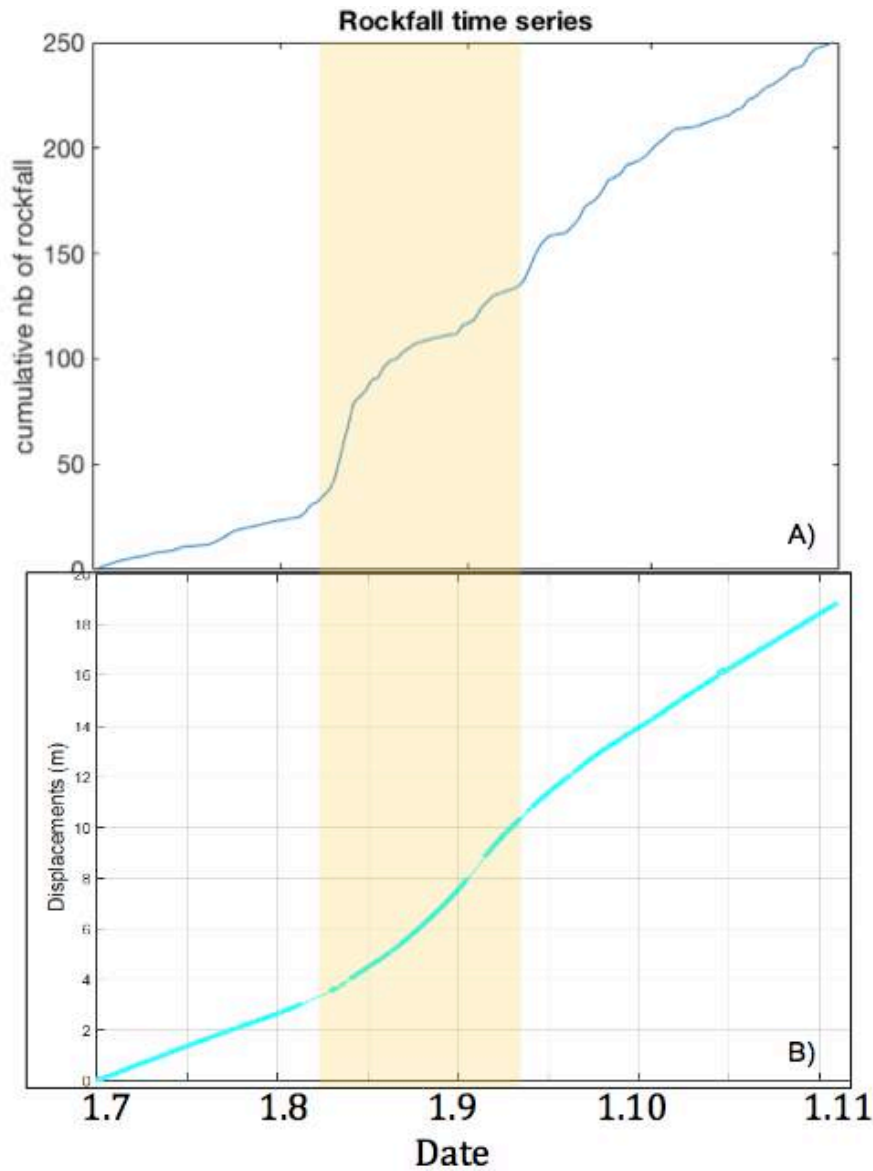


Figure 37: A) Cumulative number of events (blue) and events confirmed on the webcam (black) and B) surface displacement of reflector 72 located just above Moosfluh DSGSD fast moving part

Interpretation

The first hypothesis is related to meteorological trigger. The large rockfall increase in mid-august was compared to temperature and precipitation data (Figure 38). It was found to correspond to heavy rainfall with about 78 mm of rain between the 8th, 9th and 10th of August including 47 mm on the 10th only. The rainfall was confirmed in the seismic signal with several long lasting and shorter heavy rainfall events apparent in Catzulecher and Driest. The rainfall was also confirmed on webcam photos where rain clouds and large water drops were clearly visible. Moreover, on the webcam, precipitations as snowfall were observed during the 11th of August in the morning (from 04h). At 16h (first photo

without clouds) everything had already melted. According to the seismic signal, the most intense rainfall event occurred the 10th of August between 20h30 and 24h00 in Catzulecher (Appendix 11). With a shift of 2 days, the 3 days with the most rockfalls correspond to these 3 days of intense precipitation. In this case rainfall was seen as the trigger for this increase in rockfall activity. In early and mid September as well as in the beginning of November further rockfall activity increase occurred shortly after relatively large rainfall events (Figure 38).

The question now is: Can the same trigger account for the increase in surface displacement 3 weeks later? It is known that heavy rainfall or/and snowmelt events induce changes in pore pressure at depth and can affect DSGSD displacement rates. It is believed that a minimum threshold has to be reached to generate acceleration (Brückli et al., 2013, Wolter and Löw., 2016). The threshold was investigated (Domènech, 2015, Peruccacci et al., 2017) and it was estimated that when daily precipitation exceeded 40 mm, landslides could be triggered and displacement rate increased. Therefore, the shift of 3 weeks observed between the increase in activity and the acceleration in the displacement rate in Moosfluh could be explained by the time it takes for the water to infiltrate the slope and act on the sliding plane of the DSGSD. Nevertheless due the characteristic high permeability of the DSGSD caused by a highly fractured rock mass, the time lag for water infiltration is in the order of hours to days. In conclusion, these 3 days of intense rainfall explains the increase in rockfall activity, but not the increase in the displacement rate 3 weeks later.

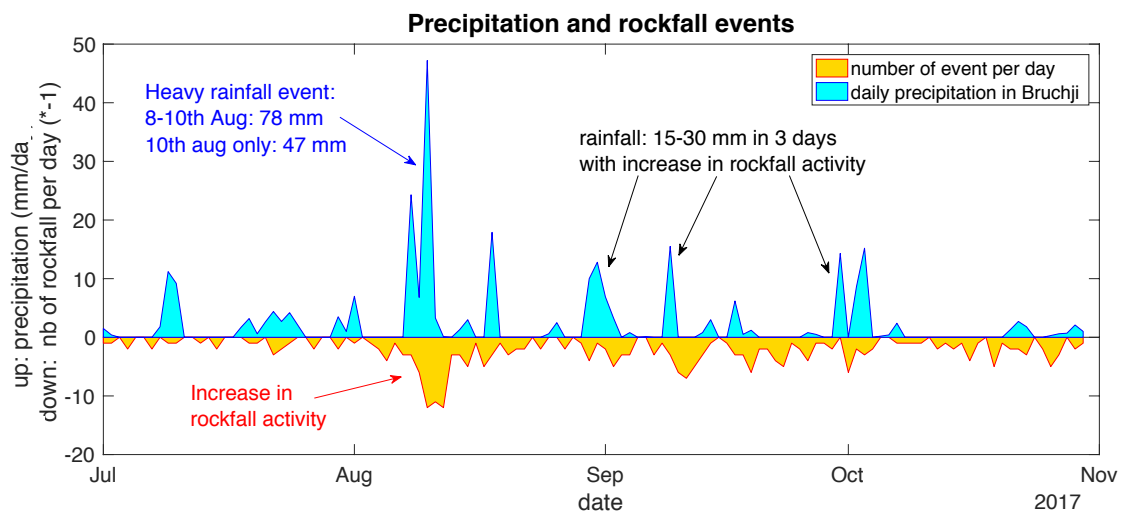


Figure 38: Daily precipitation data and daily rockfall events between July 1st and October 31st 2017.

The second hypothesis is linked to the location of the reflector 72 (Figure 2), which is outside of the area where most rockfall occurred and just outside of the fast moving part of the DSGSD. The hypothesis is that the fast moving part moved in a first step and with a faster rate. That displacement lead to changes in the stress state and in a second step, the displacement propagated upwards to the rest of the DSGSD with smaller displacement.

The third hypothesis is that the increase in displacement rate of the DSGSD is due to seasonal changes in temperature. Mechanically, temperature changes and in particular temperature drops lead to contraction of material (here the bedrock). That contraction causes crack initiation and propagation

and gives the little destabilization needed to trigger rockfalls and increase in displacement rate (Gunzburger et al., 2004, Dietze et al., 2017b). Indeed the temperature is at his maximum in August, its minimal in January creating drops of 20°C between these months. Moreover drops of 10°C within 2 weeks were observed each year as shown in Figure 39. The large increase in displacement rate of 2016 took place during one of these drops (12 September – 10 November) and the one in 2017 as well (1-16 September, Figure 38). Nevertheless, other large temperature drops were recorded in 2015 for example (blue box in Figure 39), which did not lead to dramatic acceleration of the DSGSD although the general trend was an exponential increase in the velocity since 2005 (chapter 3.4).

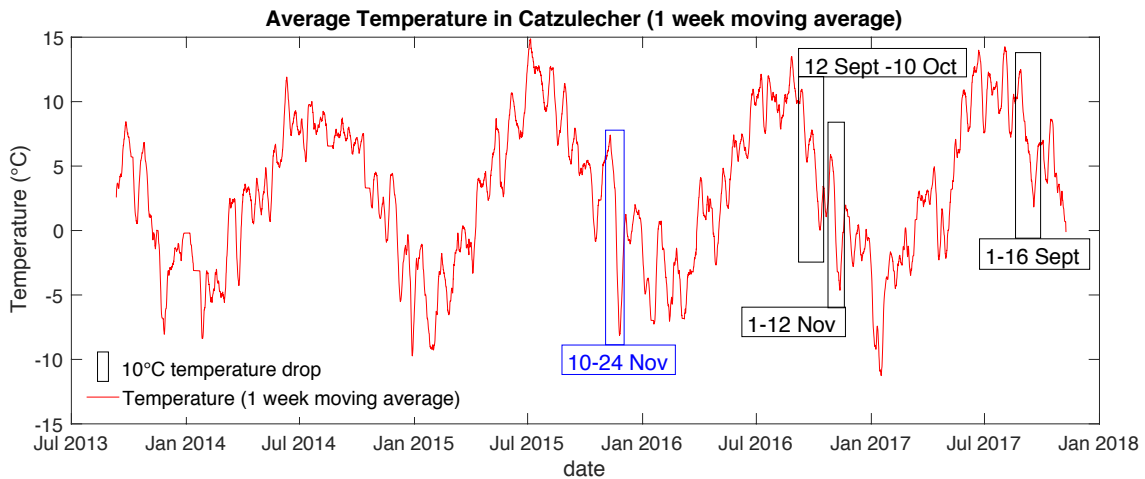


Figure 39: 1 week moving average of the temperature in Catzulecher (July 2013 - November 2017)

Increase in activity with temperature difference was as well observed at a daily scale. The number of rockfalls increased during the evening and night when the temperature dropped. Figure 40 shows temperature data during a typical sunny September day showing a drop of 7°C between 18h and 01h (local time). This is as well the time of the day when most rockfalls were recorded. Indeed 56% of all rockfalls occurred between 18h and 04h against 27% between 08h and 18h (both are 10 hours time periods) (Figure 41).

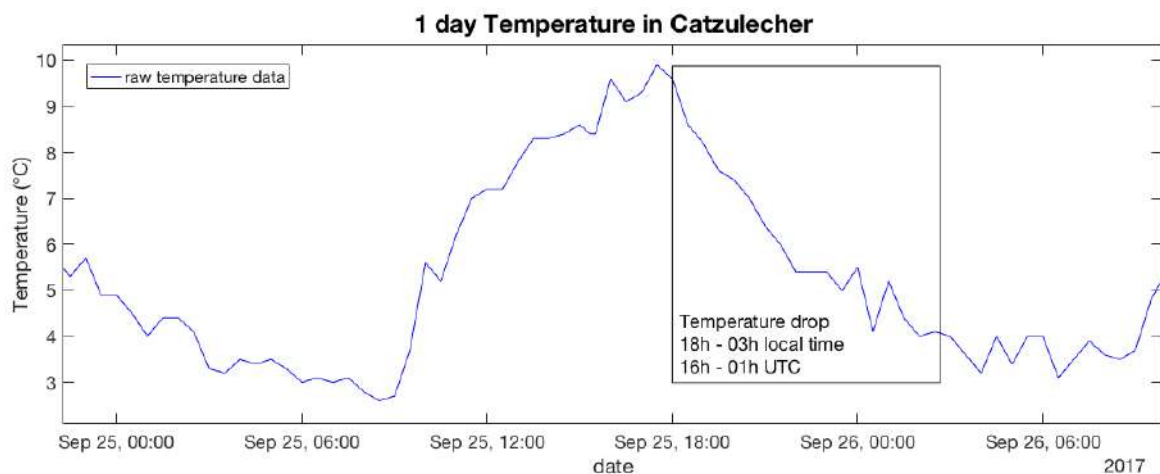


Figure 40: Typical temperature of a September day in Catzulecher (time in UTC + 2 (Local time)). The temperature is measured every 30 minutes.

The daily rockfall distribution was then studied more in details to be sure that this trend was not an artifact. Indeed a bias exists due to large noise level during daytime (chapter 5.3) in particular the noise generated by the operation of the Moosfluh cable car between 8h and 16h30 for small events. Indeed many small events could be seen at night in Catzulecher and Moosfluh but not in Driest. Therefore, the same events occurring during the day could only be seen in Catzulecher, 1 station being too few for event confirmation. Nevertheless 97% of the events were seen in driest and 99% in Catzulecher in contrast with only 61% seen in the cable car station so that the bias negligible. On the other hand, a previous study in Moosfluh (Weber, 2017) using only webcam photos identified the largest occurrence of rockfalls in the morning. This is due to large bias in term of rockfall identification since it is much more difficult to identify rockfalls when comparing photos having large temporal baseline and very different light conditions (morning-evening), which are mostly the rockfall occurring at night. This result shows the importance of continuous recording that are not influenced by light and weather conditions. Another possible bias was investigated, which is that the rockfalls produced by the heavy rainfall event in August were mostly happening in the evening, due to a given intense rainfall in the evening. Nevertheless it was found that these rockfalls occurred the entire day and night and even a slightly larger amount of rockfalls occurred between 14h and 16h so that it could not cause the larger occurrence of rockfalls at night.

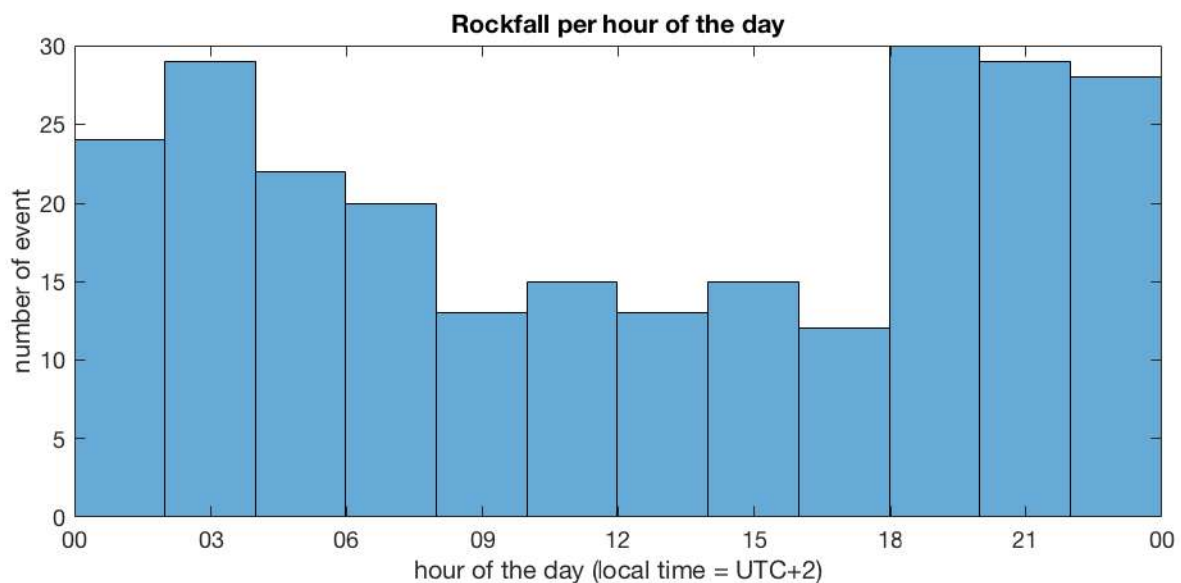


Figure 41: Event distribution across one day (time in UTC, local time = UTC + 2)

After the review of 3 hypotheses, 2 triggers were identified for rockfalls: intense rainfall led to increase in rockfall activity within few days during and after the rainfall event, while daily temperature drops is the driving parameters for the rockfall distribution at a daily scale. The cause of the shift between the increase in rockfall activity and displacement rate remains unclear. It may be triggered by autumnal temperature drops or due to timing difference in the several parts of the DSGSD. Other phenomena may as well be involved.

6.5 Magnitude frequency plot

Figure 43 presents the final magnitude frequency plot calculated with the extrapolated kinetic energy. The power law predicts well the distribution of rockfalls in a given magnitude range. Nevertheless, below 1.7×10^5 KJ (12 in log scale) and above 1.1×10^6 KJ (13.9 in log scale) the curve shows rollovers. On both sides, the frequency of rockfall occurrence is reduced compared to the prediction made by the power law.

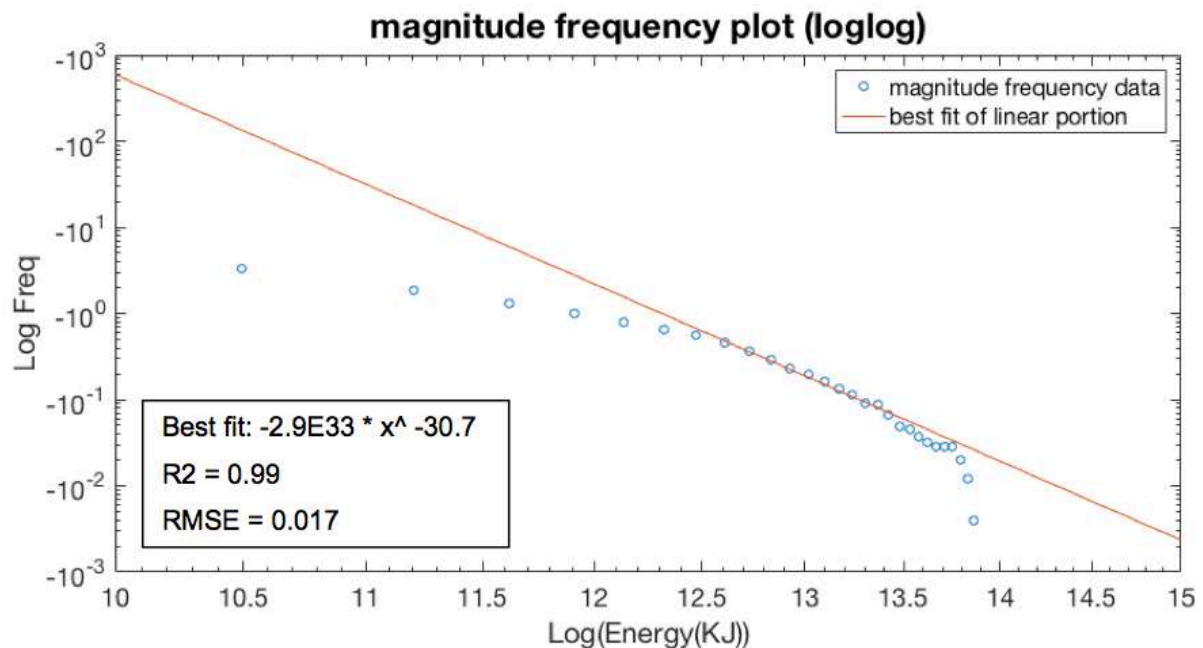


Figure 43: Magnitude frequency plot with the energy estimation and cumulative frequency (natural logarithm of the energy and the frequency)

Interpretation

It is known that under-sampling and geological factors may explain rollover behaviors (Btagi et al., 2017, Corominas et al., 2017). The low magnitude large frequency rollover (left side of Figure 43) is probably due to under-sampling of low magnitude events. The resolution of the seismometers capturing events is limited and only some low magnitude events can be resolved, for example during very quiet nights when the noise level is at its minimum. For large magnitude low frequency events (right side of Figure 43), the deviation may be explained by geological factors such as discontinuity sets, lithology, active tectonic, or glacial history (Corominas et al., 2017). From this magnitude frequency plot, it seems that the highly degraded rock mass of Moosfluh is preventing large highly energetic rock slope failure to occur (larger than 1.1×10^6 KJ). Nevertheless, large slope failures were observed in Moosfluh both in October 2016 and May 2018. In addition, several catastrophic failures were recorded in the same valley further downslope on the both valley sides. It suggests that largest event depend on the time scale investigated and need large displacement rate of the DSGSD to occur.

It brings up the question of the possibility to extrapolate magnitude frequency plots to other places in the world having similar geological setting. In chapter 5.5.2 the hypothesis that frequency has to be

adapted to the trigger and geology was made. In Moosfluh the trigger being a DSGSD undergoing seasonal and yearly variation in the displacement rate, the rockfall frequency has to be adapted to each time period. For example, the sudden acceleration of the DSGSD in Autumn 2016 induced over 600 rockfalls identified from the webcam photos within three months (Weber, 2017) contrasting with our 4 months in 2017 characterized by smaller acceleration inducing (only) 250 Rockfalls, mostly of smaller magnitude (only 75 to 95 events were seen on the webcam). In 2016, larger rock slope failures could be observed, up to several orders of magnitude larger than the ones recorded with the raspberry shakes. It appears that not only the frequency but as well the upper magnitude of the largest occurring event depends on the DSGSD displacement rate. In conclusion due to highly changing conditions in Moosfluh, the magnitude frequency plot displayed in Figure 43 represents the rockfall distribution for periods undergoing displacement in the order of 10 to 30 centimeters per day. For smaller or larger displacement rate, both the frequency scale and the magnitude of the largest possible event (upper cut-off value) have to be adapted. Alternatively monitoring over one (or several) year would give more complete data taking into account seasonal (and yearly) variation giving a frequency magnitude plot representing the long-term activity of the slope.

6.6 Uncertainty estimation

Knowing the accuracy of the different parameters and measuring methods is important when analyzing the results. Table 2 shows an estimation of the uncertainties for the main parameters. For most variables, the uncertainty was measured from the dataset based on statistics and comparison between the 3 seismic stations (duration, amplitude, frequency, picking) or between two different methods used (source, deposit, runout, energy).

Parameters	Uncertainty
Duration	± 2 seconds
Peak amplitude	$\pm 1e-7$
Frequency (of the signal)	± 2 Herz
Picking	± 0.5 seconds
Source location	~ 30 meters
Deposit location	~ 80 meters
Runout	~ 30 meters
Volume	$\pm 5*5*5$ meters
Dem	Resolution 2 meters (outdated)
Georectification	± 30 pixels (Geoprævent image)
Mean kinetic energy	10-15% of block energy ($\sim 200'000$ kJ)
Energy-duration correlation	$R^2=0.74$ /RMSE= $1.5e+5$

Table 2: Uncertainties estimation of the main parameters

The DEM has a 2 meters resolution but the large displacement undergoing in the slope and the glacier melt introduces additional errors. Nevertheless, within the fast moving part, differential movement is estimated to few meters so the runout and volumes are only little affected. The peak amplitude is accurate at a single station but varies a lot between the three stations since it is dependent on the terrain (wave attenuation and amplification). The picking of starting time is challenging but is crucial

only when trying to localize events from the seismic data. The source and deposit locations could be improved with good knowledge of the visual aspect of the slope and some training with identifying features between webcam photos, the slope in the field and the high-resolution photo. The correlation between the energy and duration was good after removal of 4 outlier events.

7 DISCUSSION AND CONCLUSION

In this project, a new type of seismometers, the low cost raspberry shakes, were used to monitor rockfalls at local scale. With the combination of optical data from a webcam and field measurements, the DSGSD of Moosfluh was more precisely characterized. In particular the rockfall distribution in time and space was better understood and a magnitude frequency plot was built providing useful information for a global hazard assessment. To fill a monitoring gap, passive seismic was chosen because it allows continuous monitoring and is independent of weather and light conditions. Nevertheless optical data were necessary to confirm the signal and scale the seismic parameters to the physical parameters of the rockfalls.

The first challenge was to identify rockfalls on the seismic data and discriminate them from other event types and noises. With the help of previous studies and optical data, typical properties for rockfall seismic signal could be established and 7 categories of rockfalls were described. Most rockfalls have gradual increase during their onset phase, a mean frequency between 3 and 8 Hz, and duration from 5 to 30 seconds. For each rockfall, the onset time, frequency, peak amplitude and duration were calculated and entered in a rockfall catalogue. Extra parameters were obtained for 20 events seen in the webcam photos, namely the source and deposit location, the runout distance, and the block volume. From these parameters the mean kinetic Energy was modeled.

All these information were used to assess the spatial and temporal distribution of the rockfalls. The number of rockfalls increased in the middle of August, corresponding to an increase in the surface displacement 3 weeks later. The increase in rockfall activity was linked to 3 days of intense rainfall but due to the high permeability of the heavily fractured rock mass of the DSGSD, the rainfall event cannot have caused the observed increase in displacement rate. The two hypotheses for that increase are seasonal temperature drop and propagation of the DSGSD from the fast moving part to the rest of the body. Nevertheless other phenomena might as well cause such acceleration. At the rockfall scale, the location of rockfall sources is time depend. Most rockfalls occurred in the southeastern part of the slope and were concentrated in August and September while the rest of the rockfalls took place in the northwestern part of the slope mostly in July and August. Moreover the majority of rockfalls occurred during nighttime during daily temperature drop.

The combination of seismic and optic data enabled the calculation of rockfall kinetic energy and creation of a magnitude frequency plot. The rockfall distribution follows a power law for over one order of magnitude and is characterized by cutoff on both sides (low and high magnitude events). The one in the low magnitude area is due to the sensor resolution leading to under-sampling of small rockfalls. In the area of large magnitude, the cutoff was partly explained by geological factors. This product characterizes the rockfall phenomena in Moosfluh covering useful parameters for risks mitigation,

namely the energy of the event with their respective frequency, as well as the area of occurrence. Nevertheless, large temporal variation of the rockfall phenomena result in widely variable plots depending on the monitoring time-scale chosen. Therefore the calculated frequency and largest possible event cutoff only apply to time period showing similar displacement rate and similar slopes. By monitoring over several years, this high variability would be incorporated and give insights into long-term activity of the slope.

In conclusion the monitoring of rockfalls with low-cost seismometers was successful and the raspberry shakes seismometers can be recommended in other rockfall active areas to measure the phenomena at local scale. Despite the resolution limit and the fact that seismic only gives indirect measurement, it provides continuous data and when combined with optical tool the rockfall phenomena can be fully assessed with almost no bias, providing deeper understanding of the mechanisms and can also be used in mitigation strategies.

In the future, automation of the rockfall identification process would allow large expansion of the rockfall catalogue over long time periods. Indeed manual identification of rockfalls is very time consuming. Another improvement could be automatic location of the rockfalls from the seismic data alone. These two steps could be used to build an early warning or fast response system in areas exposed to rockfalls. More time could be also invested in deeper understanding of the magnitude frequency plots to understand how it changes with various time-periods and how to scale and extrapolate them in slopes showing similar characteristics. It would allow much faster hazard assessment since it would mean that only few magnitude frequency plots and some extra data would be needed to assess the hazard in any slope.

8 ACKNOWLEDGEMENTS

I first would like to thank my supervisor Andrea Manconi for his guidance, motivation and ideas and to give me the opportunity to work on this interesting and up-to date project.

Many thanks go to Marc Hügentobler and Nicolas Östreicher for the field experience and fruitful discussions. Thank you to everybody in the C1.1 and E39 offices for great work environment and discussions throughout the project and thank you to all my flat mates for all their support and discussion.

Tank you to Reto Seifert for his help before and during the sensors installation and am grateful to Martin Ziegler for his help and demonstration of the Leica vector range finder.

I am grateful to the company Geoprævent for sharing 2 of their high quality photographs of the Moosfluh landslide. It has been of great help and a pleasant relief to my eyes.

Additional seismic data are available through the Eida (<http://www.oreus-eu.org/data/eida>) and raspberry shake (<http://www.raspberrysake.org>) networks.

9 REFERENCES

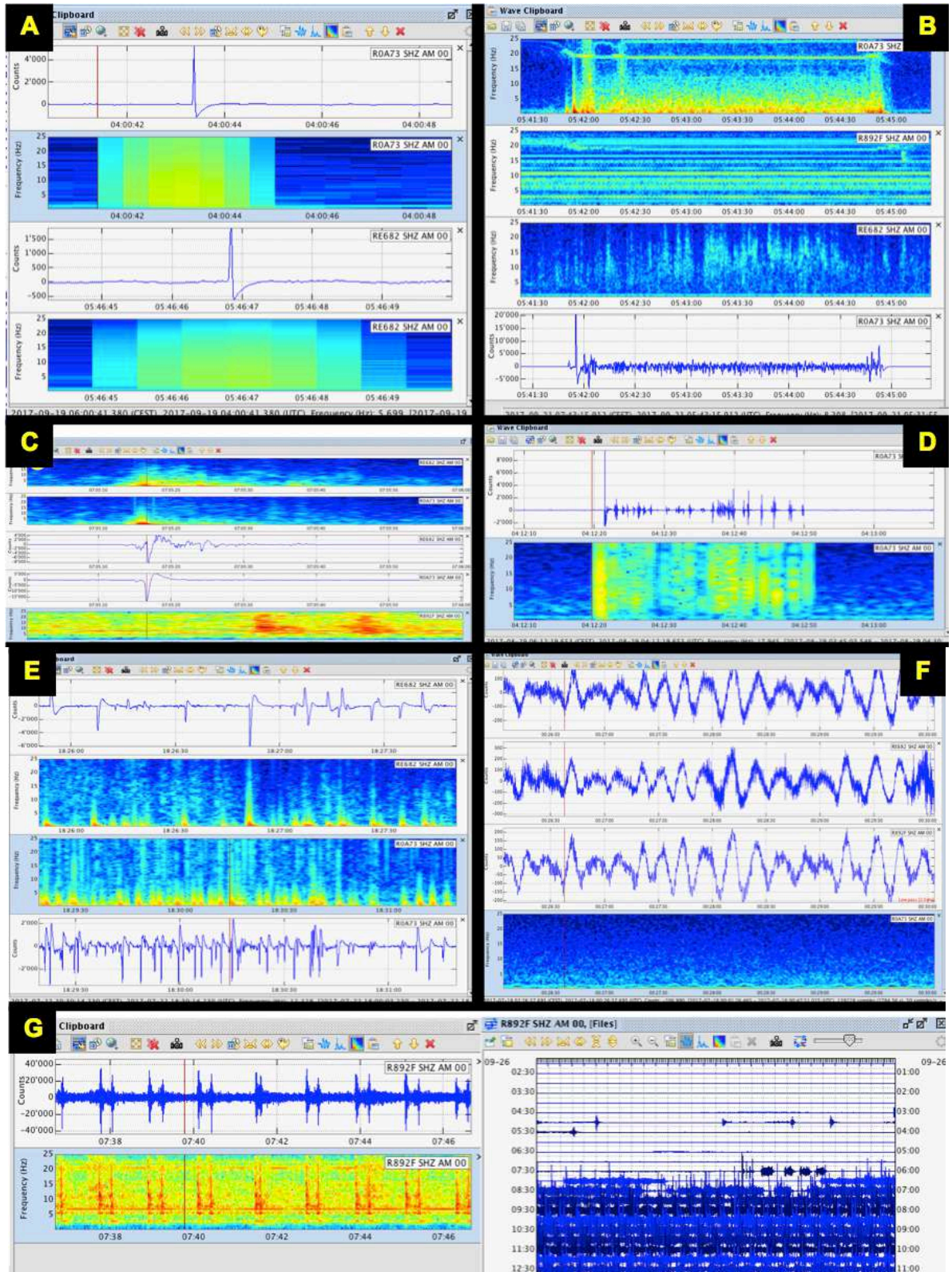
- Agliardi, F., Crosta, G., Zanchi, A. and Ravazzi, C. (2009). Onset and timing of deep-seated gravitational slope deformations in the eastern Alps, Italy. *Geomorphology*, 103(1), pp.113-129.
- Borgatti, L. and Soldati, M. (2013). Hillslope Processes and Climate Change. In: J. Shroder, ed., *Treatise on Geomorphology*. Elsevier science, pp.306-319.
- Brückl, E., Brunner, F., Lang, E., Mertl, S., Müller, M. and Stary, U. (2013). The Gradenbach Observatory—monitoring deep-seated gravitational slope deformation by geodetic, hydrological, and seismological methods. *Landslides*, 10(6), pp.815-829.
- Bürgmann, R., Rosen, P. and Fielding, E. (2000). Synthetic Aperture Radar Interferometry to Measure Earth's Surface Topography and Its Deformation. *Annual Review of Earth and Planetary Sciences*, 28(1), pp.169-209.
- Cervelli, D., Cervelli, P., Parker, T. and Murray, T. (2017). *Swarm*. Alaska Volcano Observatory:USGS.
- Corominas, J., Mavrouli, O. and Ruiz-Carulla, R. (2017). Magnitude and frequency relations: are there geological constraints to the rockfall size?. *Landslides*, 15(5), pp.829-845.
- Cossart, E., Braucher, R., Fort, M., Bourlès, D. and Carcaillet, J. (2008). Slope instability in relation to glacial debuitressing in alpine areas (Upper Durance catchment, southeastern France): Evidence from field data and ¹⁰Be cosmic ray exposure ages. *Geomorphology*, 95(1-2), pp.3-26.
- Crisinel, A. (1978). GEOLOGIE DE LA RESERVE NATURELLE DE LA FORET D'ALETSCHE (VALAIS - SUISSE). *Bulletin de la Murithienne*, 95, pp.45-58.
- Dammeier, F., Moore, J., Hammer, C., Haslinger, F. and Loew, S. (2016). Automatic detection of alpine rockslides in continuous seismic data using hidden Markov models. *Journal of Geophysical Research: Earth Surface*, 121(2), pp.351-371.
- Dammeier, F., Moore, J., Haslinger, F. and Loew, S. (2011). Characterization of alpine rockslides using statistical analysis of seismic signals. *Journal of Geophysical Research*, 116(F4).
- De Biagi, V., Napoli, M., Barbero, M. and Peila, D. (2017). Estimation of the return period of rockfall blocks according to their size. *Natural Hazards and Earth System Sciences*, 17(1), pp.103-113.
- Deparis, J., Jongmans, D., Cotton, F., Baillet, L., Thouvenot, F. and Hantz, D. (2008). Analysis of Rock-Fall and Rock-Fall Avalanche Seismograms in the French Alps. *Bulletin of the Seismological Society of America*, 98(4), pp.1781-1796.
- Dietze, M., Mohadjer, S., Turowski, J., Ehlers, T. and Hovius, N. (2017a). Seismic monitoring of small alpine rockfalls – validity, precision and limitations. *Earth Surface Dynamics*, 5(4), pp.653-668.
- Dietze, M., Turowski, J., Cook, K. and Hovius, N. (2017b). Spatiotemporal patterns, triggers and anatomies of seismically detected rockfalls. *Earth Surface Dynamics*, 5(4), pp.757-779.
- Domènech, G. (2015). *Assessment of the magnitude-frequency relationship of landslides and rockfalls: Application to hazard mapping*. PhD in Geotechnical Engineering and Geo-Sciences. UTP (polytechnic university of catalonia).
- ETH, zürich (2016). *The Cerentino Landslide: Analysis of Existing Data and Proposed Complementary Investigations*.
- Frukacz, M., Presl, R., Wieser, A. and Favot, D. (2017). Pushing the sensitivity limits of RTS-based continuous deformation monitoring of an alpine valley. *Applied Geomatics*, 9(2), pp.81-92.
- GEOPRÆVENT AG. (2018). *Webcams | GEOPRÆVENT AG – Elektronische Überwachung von Naturgefahren*. [online] Available at: <https://www.geopraevent.ch/technologien/webcams/> [Accessed 9 Apr. 2018].
- Geertsema, M. and Chiarle, M. (2013). Mass-Movement Causes: Glacier Thinning. In: J. Shroder, ed., *Treatise on Geomorphology*. Elsevier science, pp.217-222.

- GitHub. (2017). *geoscience-community-codes/GISMO*. [online] Available at: <https://github.com/geoscience-community-codes/GISMO> [Accessed 24 Oct. 2017].
- Grämiger, L., Moore, J., Gischig, V., Ivy-Ochs, S. and Loew, S. (2017). Beyond debuttressing: Mechanics of paraglacial rock slope damage during repeat glacial cycles. *Journal of Geophysical Research: Earth Surface*, 122(4), pp.1004-1036.
- Gunzburger, Y., Merrien-Soukatchoff, V. and Guglielmi, Y. (2005). Influence of daily surface temperature fluctuations on rock slope stability: case study of the Rochers de Valabres slope (France). *International Journal of Rock Mechanics and Mining Sciences*, 42(3), pp.331-349.
- Härer, S., Bernhardt, M. and Schulz, K. (2015). PRACTISE – Photo Rectification And Classification SoftwarE (V.2.0). *Geoscientific Model Development Discussions*, 8(10), pp.8481-8518.
- Helmstetter, A. and Garambois, S. (2010). Seismic monitoring of Séchilienne rockslide (French Alps): Analysis of seismic signals and their correlation with rainfalls. *Journal of Geophysical Research*, 115(F3).
- Hibert, C., Mangeney, A., Grandjean, G., Baillard, C., Rivet, D., Shapiro, N., Satriano, C., Maggi, A., Boissier, P., Ferrazzini, V. and Crawford, W. (2014). Automated identification, location, and volume estimation of rockfalls at Piton de la Fournaise volcano. *Journal of Geophysical Research: Earth Surface*, 119(5), pp.1082-1105.
- IPCC Fifth Assessment Report: CSIROexperts comment. (2013). *ECOS*, pp.p 56-73.
- Kelly, M., Kubik, P., Von Blanckenburg, F. and Schlüchter, C. (2004). Surface exposure dating of the Great Aletsch Glacier Egesen moraine system, western Swiss Alps, using the cosmogenic nuclide¹⁰Be. *Journal of Quaternary Science*, 19(5), pp.431-441.
- Kortström, J., Uski, M. and Tiira, T. (2016). Automatic classification of seismic events within a regional seismograph network. *Computers & Geosciences*, 87, pp.22-30.
- Kos, A., Amann, F., Strozzi, T., Delaloye, R., von Ruetten, J. and Springman, S. (2016). Contemporary glacier retreat triggers a rapid landslide response, Great Aletsch Glacier, Switzerland. *Geophysical Research Letters*, 43(24), pp.12,466-12,474.
- Loew, S., Glueer, F. and Manconi, A. (2017). Unravelling detailed kinematics of DSGSD morphostructures (Moosfluh, Swiss Alps). *Geophysical Research Abstracts*, Vol. 19(EGU2017-3847).
- Manconi, A., Picozzi, M., Coviello, V., De Santis, F. and Elia, L. (2016). Real-time detection, location, and characterization of rockslides using broadband regional seismic networks. *Geophysical Research Letters*, 43(13), pp.6960-6967.
- Manconi, A., Kourkoulis, P., Caduff, R., Strozzi, T. and Loew, S. (2018a). Monitoring Surface Deformation over a Failing Rock Slope with the ESA Sentinels: Insights from Moosfluh Instability, Swiss Alps. *Remote Sensing*, 10(5), p.672.
- Manconi, A., Glüer, F. and Löw, S. (2018b). Displacement time series of active slopes from time-lapse cameras.
- Matoza, R., Green, D., Le Pichon, A., Shearer, P., Fee, D., Mialle, P. and Ceranna, L. (2017). Automated detection and cataloging of global explosive volcanism using the International Monitoring System infrasound network. *Journal of Geophysical Research: Solid Earth*, 122(4), pp.2946-2971.
- MeteoSwiss (2017). *MeteoSwiss IDAWEb*. [online] Gate.meteoswiss.ch. Available at: <https://gate.meteoswiss.ch/idaweb/> [Accessed Dec. 2017].
- Mityska, M. (2014). *ReadMSEEDFast(fileName) - MATLAB Central File Exchange*. [online] Ch.mathworks.com. Available at: <https://ch.mathworks.com/matlabcentral/fileexchange/46532-readmseefast-filename> [Accessed Sep. 2017].

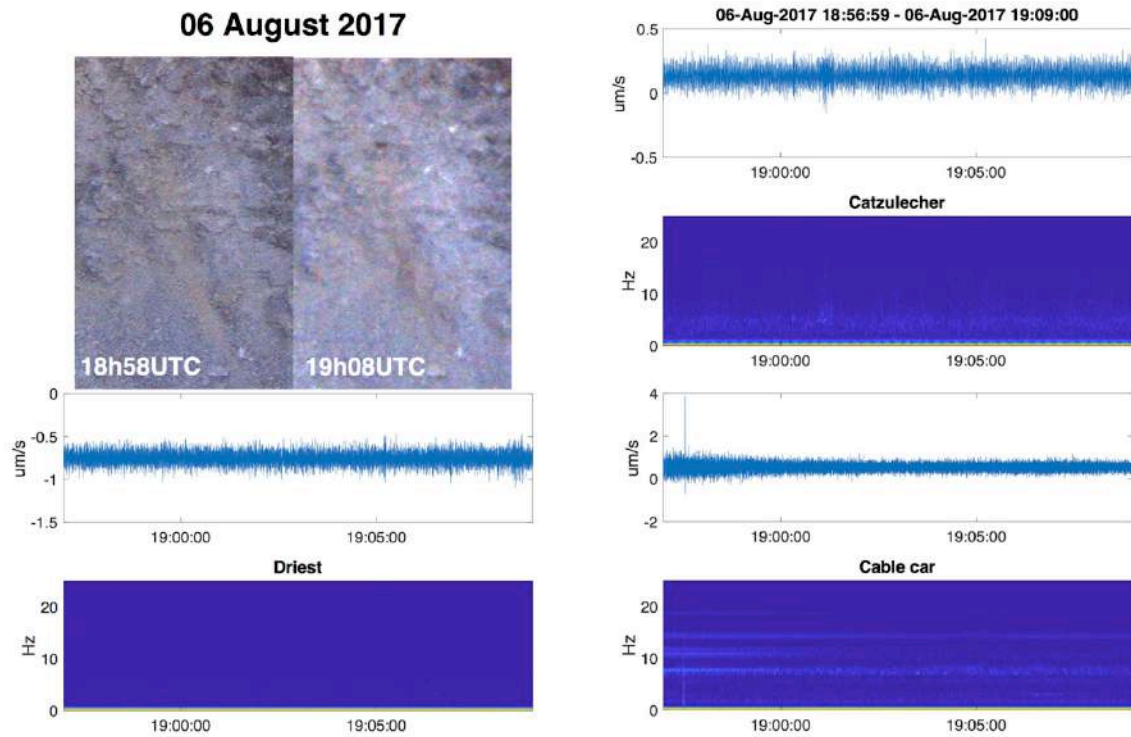
- Orfeus-eu.org. (2017). *ORFEUS - EIDA*. [online] Available at: <http://www.orfeus-eu.org/data/eida/> [Accessed 22 Oct. 2017].
- OSOP, S. (2017). *Raspberry Shake • Watching the earth move*. [online] Raspberry Shake. Available at: <http://www.raspberrysshake.org> [Accessed 23 Oct. 2017].
- Palis, E. Lebourg, T. Tric, E. Malet, J. and Vidal, M. (2016). Long-term monitoring of a large deep-seated landslide (La Clapiere, South-East French Alps): initial study. *Landslides*, 14(1), pp.155-170.
- Peruccacci, S., Brunetti, M., Gariano, S., Melillo, M., Rossi, M. and Guzzetti, F. (2017). Rainfall thresholds for possible landslide occurrence in Italy. *Geomorphology*, 290, pp.39-57.
- Poli, P. (2017). Creep and slip: Seismic precursors to the Nuugaatsiaq landslide (Greenland). *Geophysical Research Letters*, 44(17), pp.8832-8836.
- Pro Natura (2017). *Le Grand Glacier d'Aletsch*. [online] Pronatura-aletsch.ch. Available at: <https://www.pronatura-aletsch.ch/glacier-d-aletsch> [Accessed 22 Oct. 2017].
- Satriano, C., Lomax, A. and Zollo, A. (2008). Real-Time Evolutionary Earthquake Location for Seismic Early Warning. *Bulletin of the Seismological Society of America*, 98(3), pp.1482-1494.
- Schindelwig, I., Akçar, N., Kubik, P. and Schlüchter, C. (2011). Lateglacial and early Holocene dynamics of adjacent valley glaciers in the Western Swiss Alps. *Journal of Quaternary Science*, 27(1), pp.114-124.
- Seismo.ethz.ch, (2017). *SED | Tous les séismes*. [online] Available at: <http://www.seismo.ethz.ch/fr/earthquakes/switzerland/all-earthquakes/> [Accessed Nov. 2017].
- Strozzi, T., Delaloye, R., Kääh, A., Ambrosi, C., Perruchoud, E. and Wegmüller, U. (2010). Combined observations of rock mass movements using satellite SAR interferometry, differential GPS, airborne digital photogrammetry, and airborne photography interpretation. *Journal of Geophysical Research*, 115(F1).
- Swisstopo, (2016). *SWISSIMAGE25*. [online] Available at: https://shop.swisstopo.admin.ch/fr/products/images/ortho_images/SWISSIMAGE [Accessed Nov. 2017].
- Swisstopo, (2017a). *swissALTI3D*. [online] Available at: https://shop.swisstopo.admin.ch/fr/products/height_models/alti3d [Accessed Nov. 2017].
- Swisstopo, (2017b). *Swiss map*. [online] Map.geo.admin.ch. Available at: <https://map.geo.admin.ch> [Accessed 20 Oct. 2017].
- USGS, (2017a). *Earthquake Catalogue*. [online] Available at: <https://earthquake.usgs.gov/earthquakes/search/> [Accessed Nov. 2017].
- USGS, (2017b). *USGS Volcano Science Center Software: SWARM*. [online] Volcanoes.usgs.gov. Available at: <https://volcanoes.usgs.gov/software/swarm/index.php> [Accessed Jul. 2017].
- VAW/ETHZ & EKK/SCNA (2015). *GLAMOS Glacier Monitoring Network*. [online] Glaciology.ethz.ch. Available at: <http://glaciology.ethz.ch/messnetz/glaciers/aletsch.html> [Accessed 18 Oct. 2017].
- Vectronix, A. (2004). *Vectronix USMC VECTOR 21 Manuals*. [online] Manualslib.com. Available at: <https://www.manualslib.com/products/Vectronix-Usmc-Vector-21-3696610.html> [Accessed 24 Oct. 2017].
- Weber, S. (2017). *Untersuchung der Moosfluh Hanginstabilität anhand von Webcambildern*.
- Williams, J., Rosser, N., Hardy, R., Brain, M. and Afana, A. (2018). Optimising 4-D surface change detection: an approach for capturing rockfall magnitude–frequency. *Earth Surface Dynamics*, 6(1), pp.101-119.
- Zimmer, V. and Sitar, N. (2015). Detection and location of rockfalls using seismic and infrasound sensors. *Engineering Geology*, 193, pp.49-60.

10 APPENDIX

Appendix 1: Different noises and unknown signals observed between July and October 2017. A) Single spike occurring at a single station, B) helicopter, C) military plane, D) unknown event at a single station, E) rain, F) unknown low frequency event at the 3 stations, G) Moosfluh cable car running



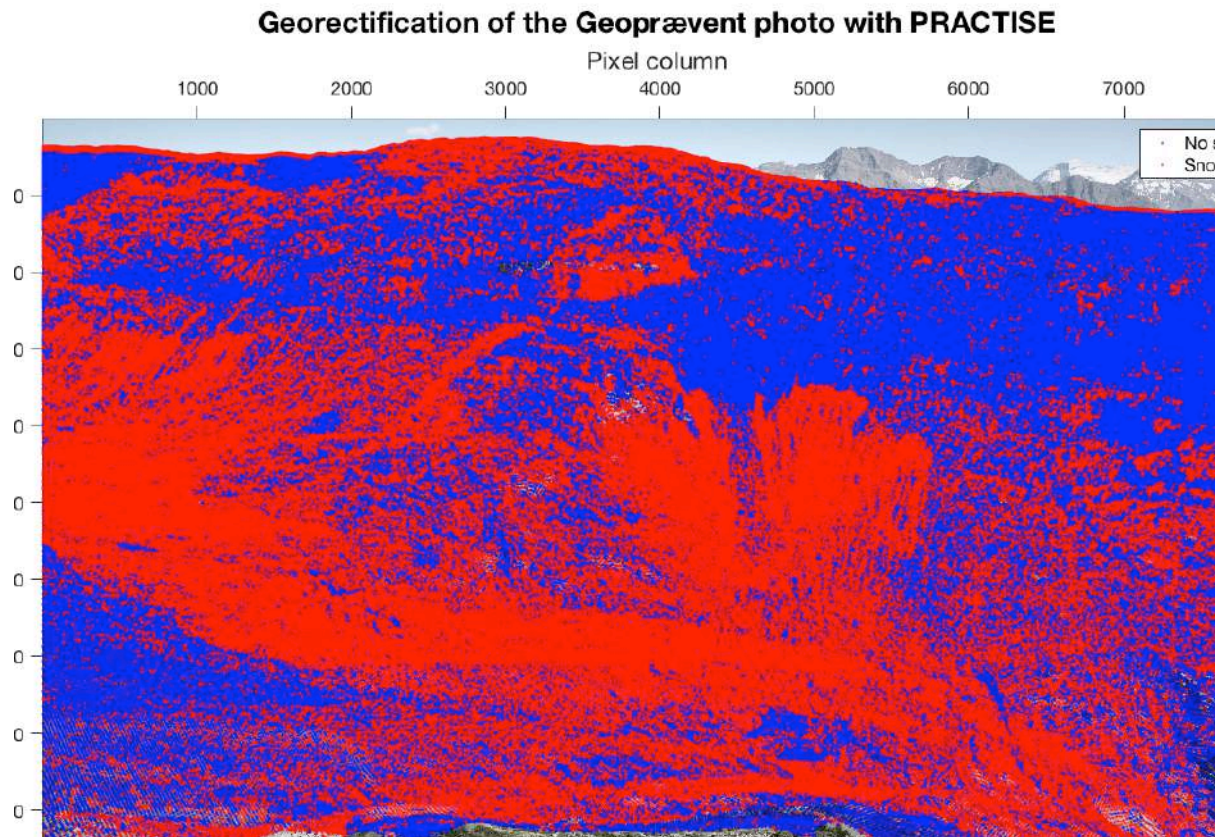
Appendix 2: Rockfall event visible on webcam photo but not on the seismic signal



Appendix 3: Extract from the event catalogue built from seismic data

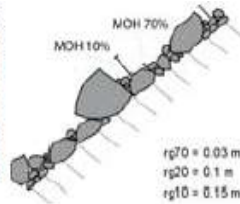
Events catalogue extract												
event number	event type	date	start time	end time	event duration	mean frequency	max magnitude	max magnitude	max magnitude	nb of station	order of arrival at station	
unit					sec	Hz	RE682-catzulecher	R892F-moosfluh	ROA73-driest		1st	2nd/3rd
1	rock fall	20.sept	23h06:43	23h06:52	9	4-10	1500	200	100	3	re+/ro	
2	rock fall	21.sept	05h01:02	05h01:17	15	2-9	1000	400	200	3	re+/ro	
3	rock fall	21.sept	06h34:42	06h35:02	20	3-10	3000	-	600	2	re/ro	
4	rock fall	22.sept	19h22:26	19h23:02	36	3-9	800	1000	400	3	re+/ro	
5	rock fall	22.sept	21h10:08	21h10:40	32	2-9	3000	4000	2000	3	r/re/ro	
6	rock fall	22.sept	21h36:48	21h36:55	7	2-8	400	400	150	2.5	re/ro	
7	rock fall	22.sept	22h19:58	22h20:14	16	3-9	400	1000	400	3	re+/ro	
8	rock fall	23.sept	03h39:17	03h39:23	6	1-6	3000	10000	2000	3	re/ro/r	
9	rock fall	23.sept	04h42:25	04h43:02	37	2-10	4000	3000	1500	3	re+/ro	
10	rock fall	23.sept	05h21:55	05h22:20	25	2-8	300	200	150	3	re+/ro	
11	rock fall	23.sept	09h04:42	09h05:05	23	3-8	1500	-	600	2	re/ro	
12	teleseism	23.sept	13h05:50	13h07	70	0-2	600	6000(1000)	1000	3	re+/ro	
13	rock fall	23.sept	16h59:05	16h59:32	27	3-9	1000	1000	500	3	re+/ro	
14	rock fall	24.sept	15h50:55	15h51:05	10	2-8	1500	1500	400	3	re+/ro	
15	local EQ	24.sept	21h48:06	21h48:17	11	2-25	7000	17000	3000	3	re+/ro	
16	local EQ	25.sept	01h50:01	01h50:04	3	2-25	600	<500	200	2.5	re+/ro	
17	rock fall	25.sept	15h20:53	15h21:18	25	2-9	3000	2000	900	3	re+/ro	
18	rock fall	25.sept	18h11:29	18h11:52	23	3-6	1000	1000(700)	400	3	re+/ro	
19	rock fall	26.sept	03h47:42	03h47:48	6	2-8	800	700	200	3	re+/ro	
20	teleseism	26.sept	04h39:50	04h42	130	0-2	600	1000	700	3	re+/ro	
21	rock fall	26.sept	14h55:05	14h55:31	26	2-8	6000	15000	3000	3	re+/ro	
22	rock fall	26.sept	15h02:55	15h03:03	8	2-8	600	700	200	3	re+/ro	
23	rock fall	26.sept	20h21:43	20h21:47	4	2-7	400	700	60	3	re+/ro	
24	teleseism	26.sept	20h34:40	20h36	80	0-2	600	700	600	3	re+/ro	
25	rock fall	27.sept	08h09:27	08h09:30	3	3-9	1500	-	90	2	re/ro	
26	rock fall	27.sept	23h15:16	23h15:31	15	2-8	1200	3000	400	3	re+/ro	
27	rock fall	28.sept	08h12:20	08h12:28	8	3-7	500	-	200	2	re+ro	
28	data missing	28.sept	14h42:40	08h45:20	env 18h	-	-	-	-	2.5	re/ro	
29	rock fall	29.sept	05h54:36	05h54:44	8	2-8	-	6000	-	1	-	
30	rock fall	29.sept	13h39:52	13h40:08	16	2-8	1000	-	200	2	re/ro	
31	rock fall	01.oct	01h56:58	01h57:05	7	3-7	2000	1000	500	3	re+/ro	
32	rock fall	01.oct	02h58:25	02h58:45	20	3-7	400	400	300	3	-	
33	rock fall	01.oct	03h36:40	03h37:00	20	2-5	300	200	200	3	re+/ro	
34	rock fall	01.oct	03h44:08	03h44:28	20	2-7	400	400	100	3	re+/ro	
35	rock fall	01.oct	10h00:34	10h00:40	6	2-8	2000	-	300	2	re/ro	
36	rock fall	01.oct	23h26:38	23h26:51	13	2-7	1100	1300	300	3	re+/ro	
37	rock fall	02.oct	06h14:37	06h14:47	10	2-6	400	-	150	2	re/ro	
38	rock fall	02.oct	11h49:50	11h50:11	21	2-9	1000	-	300	2	re/ro	
39	rock fall	03.oct	09h54:33	09h54:42	9	3-7	1200	-	200	2	re/ro	
40	rock fall	03.oct	12h06:21	12h06:28	7	2-7	1500	-	400	2	re/ro	
41	local EQ	03.oct	15h16:33	15h16:52	19	2-25	2500	4200	2000	3	re+/ro	
42	rock fall	03.oct	19h11:06	19h11:13	7	2-8	400	400	150	3	re+/ro	

Appendix 4: Georectification of the Geoprævent photo with PRACTISE. The blue and red dots correspond to DEM coordinates (the color is here for snow classification, which shouldn't be taken into account because not calibrated)



Appendix 5: Description of input parameters needed in RockyFor3D

Nb	Raster name	Raster data description	Value here	
1	DEM.asc	Digital elevation model of the area (values 0 - 8850 m)	SwissALTI3D	
2	rockdensity.asc	Density of rock in the source area (2000 – 3300 kg/m ³). The rock density in places other than source areas is set to 0 (no simulation for that cell).	2700	
3	d1.asc	3 files defining the 3 dimensions of the rock block (0-20m). The block size in places other than source areas is set to 0 (no simulation for that cell).	6-20 m	
4	d2.asc		6-20 m	
5	d3.asc		6-20 m	
6	blshape.asc	Defines the block shape (values 0-4) 0 = not defined, 1 = rectangular, 2 = ellipsoidal, 3 = spherical, 4 = disc	1	
7	rg70.asc	Slope roughness (0-100 m), 100m forces the block to stop.	Talus	Rock

8	rg20.asc	<p>mean typical obstacle height normal to the slope surface (m) that block encounters in 70%, 20% and 10% of the cases during a rebound on the slope surface. Should be measured looking down the slope!</p> 	0.5	0.7																											
9	rg10.asc		1	3																											
			4	6																											
			Glacier(all): 100																												
10	soiltype.asc	<table border="1"> <thead> <tr> <th>Soiltype</th> <th>General description of the underground</th> <th>mean R_c value</th> </tr> </thead> <tbody> <tr> <td>0</td> <td>River, or swamp, or material in which a rock could penetrate completely</td> <td>0</td> </tr> <tr> <td>1</td> <td>Fine soil material (depth > ~100 cm)</td> <td>0.23</td> </tr> <tr> <td>2</td> <td>Fine soil material (depth < ~100 cm), or sand/gravel mix in the valley</td> <td>0.26</td> </tr> <tr> <td>3</td> <td>Scree (Ø < ~10 cm), or medium compact soil with small rock fragments, or forest road</td> <td>0.33</td> </tr> <tr> <td>4</td> <td>Talus slope (Ø > ~10 cm), or compact soil with large rock fragments</td> <td>0.36</td> </tr> <tr> <td>5</td> <td>Bedrock with thin weathered material or soil cover</td> <td>0.43</td> </tr> <tr> <td>6</td> <td>Bedrock</td> <td>0.53</td> </tr> <tr> <td>7</td> <td>Asphalt road</td> <td>0.35</td> </tr> </tbody> </table>	Soiltype	General description of the underground	mean R _c value	0	River, or swamp, or material in which a rock could penetrate completely	0	1	Fine soil material (depth > ~100 cm)	0.23	2	Fine soil material (depth < ~100 cm), or sand/gravel mix in the valley	0.26	3	Scree (Ø < ~10 cm), or medium compact soil with small rock fragments, or forest road	0.33	4	Talus slope (Ø > ~10 cm), or compact soil with large rock fragments	0.36	5	Bedrock with thin weathered material or soil cover	0.43	6	Bedrock	0.53	7	Asphalt road	0.35	<p>See</p> <p>Figure 29</p> <p>Bedrock = 6</p> <p>Source area = 6</p> <p>Glacier = 0</p> <p>Talus slope = 4</p>	
Soiltype	General description of the underground	mean R _c value																													
0	River, or swamp, or material in which a rock could penetrate completely	0																													
1	Fine soil material (depth > ~100 cm)	0.23																													
2	Fine soil material (depth < ~100 cm), or sand/gravel mix in the valley	0.26																													
3	Scree (Ø < ~10 cm), or medium compact soil with small rock fragments, or forest road	0.33																													
4	Talus slope (Ø > ~10 cm), or compact soil with large rock fragments	0.36																													
5	Bedrock with thin weathered material or soil cover	0.43																													
6	Bedrock	0.53																													
7	Asphalt road	0.35																													

Appendix 6: input parameters for rocky for 3D

id	▲	density	d1	d2	d3	blshape	rg70	rg20	rg10	soiltype	name
1	1	2700.00	8.00	6.00	7.00	1.00	0.70	3.00	6.00	6.00	s7
17	2	2700.00	24.00	18.00	21.00	1.00	0.70	3.00	6.00	6.00	s30
2	3	2700.00	8.00	18.00	10.00	1.00	0.70	3.00	6.00	6.00	s38
15	4	2700.00	6.00	6.00	6.00	1.00	0.70	3.00	6.00	6.00	s43
19	5	2700.00	16.00	22.00	17.00	1.00	0.70	3.00	6.00	6.00	s46
20	6	2700.00	6.00	12.00	9.00	1.00	0.70	3.00	6.00	6.00	s48
5	7	2700.00	6.00	10.00	8.00	1.00	0.70	3.00	6.00	6.00	s55
12	8	2700.00	12.00	10.00	11.00	1.00	0.70	3.00	6.00	6.00	s70
13	9	2700.00	12.00	12.00	12.00	1.00	0.70	3.00	6.00	6.00	s73
3	10	2700.00	8.00	18.00	10.00	1.00	0.70	3.00	6.00	6.00	s102
8	11	2700.00	12.00	12.00	12.00	1.00	0.70	3.00	6.00	6.00	s125.1
9	12	2700.00	14.00	12.00	13.00	1.00	0.70	3.00	6.00	6.00	s125.2
16	13	2700.00	16.00	6.00	11.00	1.00	0.70	3.00	6.00	6.00	s126
11	14	2700.00	22.00	18.00	20.00	1.00	0.70	3.00	6.00	6.00	s129
6	15	2700.00	12.00	8.00	10.00	1.00	0.70	3.00	6.00	6.00	s160
10	16	2700.00	12.00	10.00	11.00	1.00	0.70	3.00	6.00	6.00	s195
7	17	2700.00	6.00	10.00	8.00	1.00	0.70	3.00	6.00	6.00	s13.9.2
14	18	2700.00	16.00	14.00	15.00	1.00	0.70	3.00	6.00	6.00	s19.9
4	19	2700.00	9.00	9.00	9.00	1.00	0.70	3.00	6.00	6.00	s19.9.3
18	20	2700.00	16.00	10.00	10.00	1.00	0.70	3.00	6.00	6.00	s26.9
0	100	2700.00	0.00	0.00	0.00	0.00	0.70	3.00	6.00	6.00	bedrock
22	200	0.00	0.00	0.00	0.00	0.00	100.00	100.00	100.00	0.00	glacier
21	300	0.00	0.00	0.00	0.00	0.00	0.50	1.00	4.00	4.00	talus

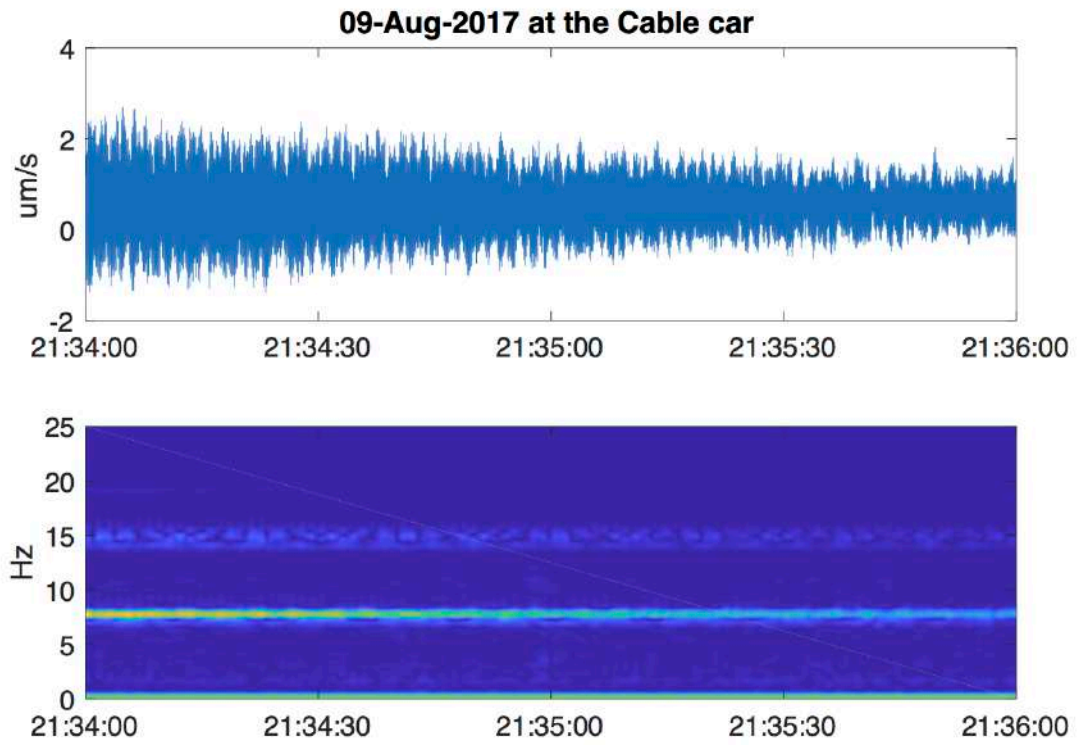
Appendix 7: Output files from RockyFor3D

Output file	Description
E_mean.asc	Mean kinetic energy (translational + rotational; in kJ) per cell
E_95.asc	95% confidence level of all kinetic energy values (in kJ) recorded in each cell
Ph_mean.asc	Mean passage height (in m; measured in normal direction to the slope surface) per cell
Ph_95.asc	95% confidence level of all passage height values (in m; measured in normal direction) recorded in each cell
Nr_passage.asc	Number of blocks passed through each cell
Nr_deposited.asc	Number of blocks stopped in each cell
Rvol_deposit.asc	Maximum block volume (in m) stopped in each cell
EL_angles.asc	Raster with the mean energy line angles per cell (in °). The energy line angle is the slope angle of a virtual direct line between the stopping location and the source location of a fallen block.

Appendix 8: Most important outputs from RockyFor3D

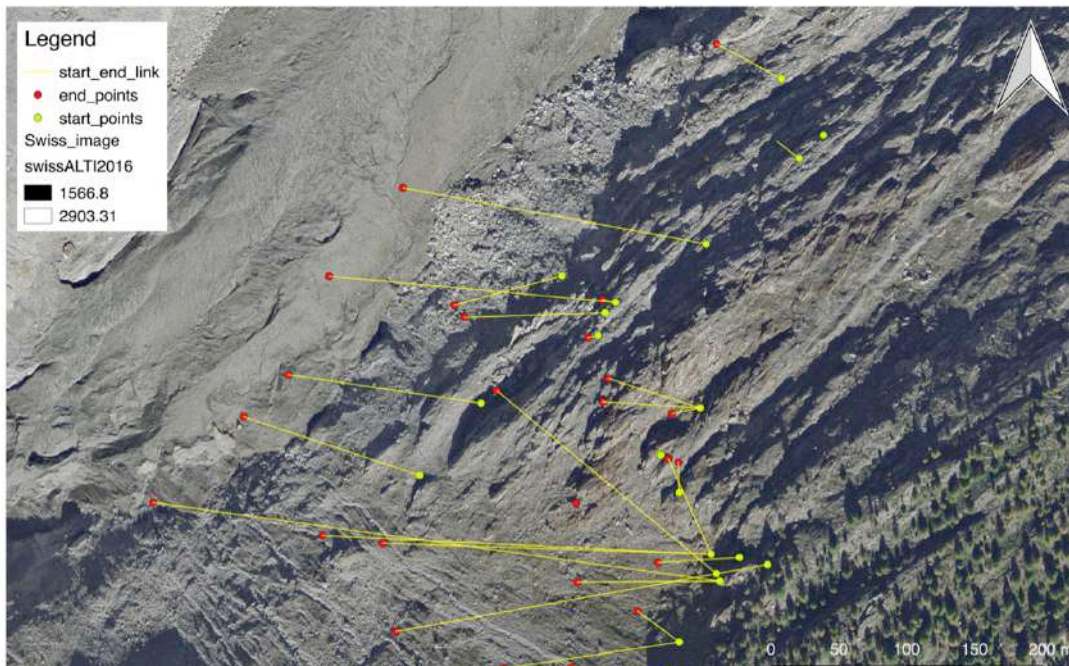
event name	date	start time	nb of station	volume (m3)	mean duration	modeled duration	peak amp Catzulecher	mean kinetic energy
s7	07.juil	22:41:21	3	336	13.35	20.00	3.83E-06	1.70E+05
s30	27.juil	15:37:43	3	4032	22.42	20.00	1.76E-05	6.00E+05
s38	04.août	02:49:27	3	1440	13.00	8.00	1.62E-06	3.00E+05
s38	04.août	02:50:00	3	1440	34.74	25.00	3.31E-06	8.00E+05
s43	06.août	18:58:00	0	216		14.00		6.00E+05
s46	07.août	18:37:25	3	3360	9.38	4.00	6.42E-06	1.40E+05
s48	08.août	07:11:18	2	648	19.80	16.00	6.02E-06	8.00E+04
s65	10.août	12:39:20	2	480	39.50	30.00	1.16E-05	1.00E+06
s70	10.août	19:06:35	3	1320	20.00	10.00	5.56E-06	2.50E+05
s73	11.août	20:37:11	3	1728	38.45	17.00	1.91E-06	9.00E+05
s102	14.août	17:58:40	3	1440	53.95	40.00	3.01E-06	1.50E+06
s102	14.août	17:58:40	3	1440	53.95	20.00	3.01E-06	7.00E+05
s125.1	21.août	20:03:13	3	1728	12.06	7.00	1.64E-06	4.00E+04
s125.2	22.août	03:57:12	3	2184	29.70	14.00	2.49E-06	4.00E+05
s126	22.août	23:46:48	3	1056	39.41	4.00	1.50E-06	3.00E+05
s126	22.août	23:46:48	3	1056	39.41	21.00	1.50E-06	1.20E+06
s129	27.août	18:24:22	3	3360	12.76	4.00	7.51E-06	3.00E+05
s160	04.sept	01:35:10	3	960	15.69	15.00	2.88E-06	2.50E+05
s195	11.sept	22:00:16	3	1320	25.37	15.00	1.05E-05	2.50E+05
s195	11.sept	22:00:16	3	1320	25.37	15.00	1.05E-05	2.50E+05
s195	11.sept	22:00:16	3	1320	25.37	4.00	1.05E-05	7.00E+04
s13.9.2	13.sept	17:51:47	2	480	24.73	26.00	3.44E-06	1.30E+06
s13.9.2	13.sept	17:51:47	2	480	24.73	9.00	3.44E-06	5.00E+04
s13.9.2	13.sept	17:51:47	2	480	24.73	30.00	3.44E-06	1.50E+06
s19.9	19.sept	20:41:35	3	3360	38.89	8.00	1.04E-05	1.20E+06
s19.9.3	19.sept	23:37:55	3	729	47.23	23.00	5.20E-06	9.00E+05
s29.9	29.sept	05:54:36	1	1600	11.20	6.00	9.48E-06	5.00E+04

Appendix 9: Night noise at the cable car station

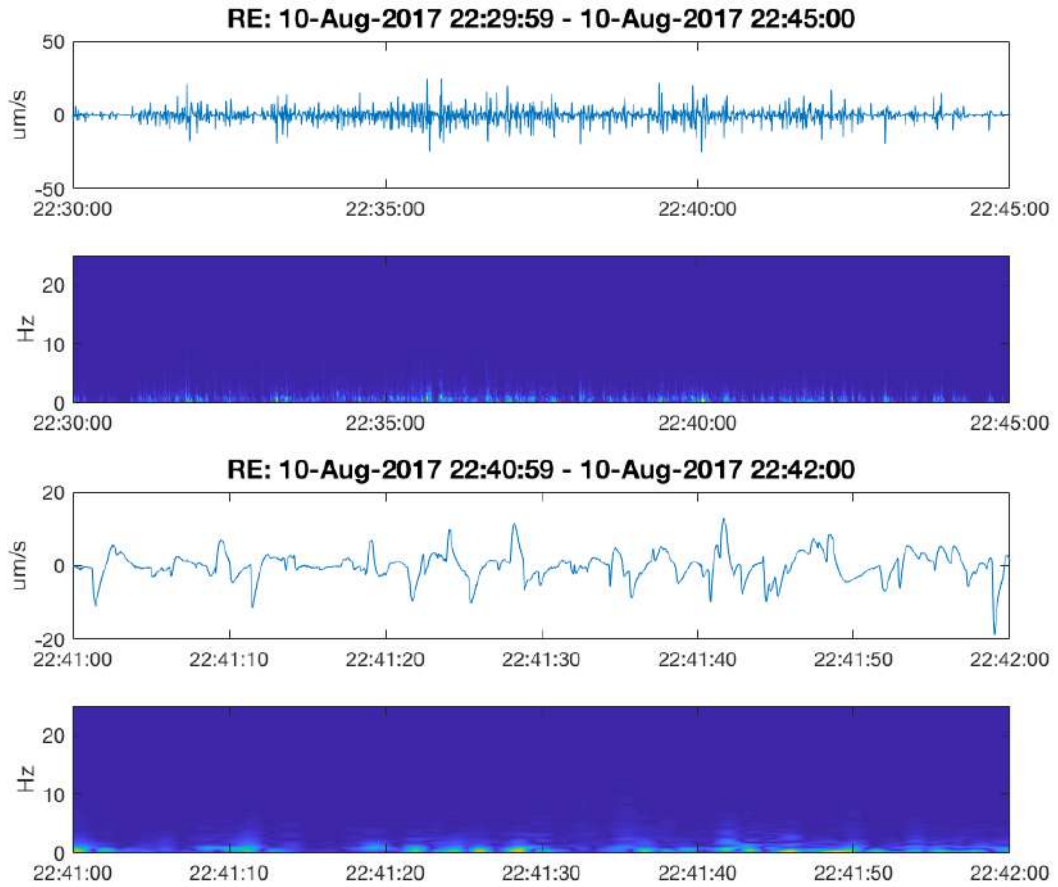


Appendix 10: Source and deposit coordinates of the 20 selected events measured with the Leica vector

Start and end location of events measured with the Leica vector



Appendix 11: Heavy rain in Catzulecher on the 10th of August between 22h30 and 22h45 (up) and a zoom between 22h41 and 22h42 (down). Heavy rain was observed in Catzulecher and Driest the 8.08.2017 from 11h30 to 12h30, the 10.08.2017 from 20h30 to 24h00 (weakly visible in Moosfluh cable car) and longer lasting less strong rainfall was observed the 9.08.2017 from 12h00 to 21h00 in Catzulecher and Driest as well.





Eidgenössische Technische Hochschule Zürich
Swiss Federal Institute of Technology Zurich

Declaration of originality

The signed declaration of originality is a component of every semester paper, Bachelor's thesis, Master's thesis and any other degree paper undertaken during the course of studies, including the respective electronic versions.

Lecturers may also require a declaration of originality for other written papers compiled for their courses.

I hereby confirm that I am the sole author of the written work here enclosed and that I have compiled it in my own words. Parts excepted are corrections of form and content by the supervisor.

Title of work (in block letters):

Mosfluh, towards a rock slope failure ?

Authored by (in block letters):

For papers written by groups the names of all authors are required.

Name(s):

Galletti

First name(s):

Maud

With my signature I confirm that

- I have committed none of the forms of plagiarism described in the 'Citation etiquette' information sheet.
- I have documented all methods, data and processes truthfully.
- I have not manipulated any data.
- I have mentioned all persons who were significant facilitators of the work.

I am aware that the work may be screened electronically for plagiarism.

Place, date

Zürich, 31st July 2018

Signature(s)

Maud Galletti

For papers written by groups the names of all authors are required. Their signatures collectively guarantee the entire content of the written paper.